ESE 131
Ocean Dynamics

Jörn Callies

March 29, 2024

Chapter 1

What does the ocean look like?

Having discussed the basics of rotating and stratified fluid dynamics in ESE 130, we now take a step back and ask what the real ocean looks like. The aim of the course is to develop a dynamical understanding of the various aspects of the ocean circulation, but this would be exceedingly difficult without being familiar with the phenomenology revealed by observations. One might be tempted to claim that it should be possible to derive these theories directly from first principles: the Boussinesq equations accurately describe every aspect of the ocean circulation, so one should be able to deduce from them how the circulation works. The theories we will describe do have this flavor of a deductive connection to the parent Boussinesq equations. But the approximations that are made along the way, arguably the DNA of these theories, are always motivated by phenomenology. For example, choosing the small-Rossby number limit in our discussion of wind-driven gyres requires knowledge not only of the size of ocean basins and the rotation rate of the planet (external parameters), but also the magnitude of the resulting flow. Our theory would have looked very different for an ocean with a much stronger circulation. So observations are an essential prerequisite to our understanding of the ocean.

Observing the ocean is challenging. The ocean is opaque to electromagnetic radiation, so remote sensing is of limited use to observe the ocean interior, and electromagnetic signals cannot be used to communicate with submerged instruments. (Acoustics are an alternative, see below.) Instruments must withstand the crushing pressure in the ocean's interior. Given hydrostatic balance, the pressure increases with depth by $-\partial p_0/\partial z = \rho_0 g = 10^4$ Pa m^{-1}, so every 10 m of water add the same pressure as the entire atmosphere (typical surface pressure: 10^5 Pa). In the sunlit surface layer, where life is abundant, biofouling is a serious impediment to making sustained measurements. At the surface, instruments must further withstand the mechanical stresses of surface gravity waves, and everywhere in the ocean, salty water threatens to corrode and short-circuit electronics. These challenges mean that observations of the ocean are generally sparse. The observations we do have are the result of the tireless work of observationalists, who often dedicate their careers to developing and deploying a single type of instrument.

1.1 Boundary conditions and forcing

We begin our discussion of the ocean's phenomenology by considering its physical context. The ocean has two fundamentally distinct boundaries: a largely solid sea floor and a moving sea surface.

Bathymetry The world ocean consists of three ocean basins—the Atlantic, Pacific, and Indian Oceans—and the circumpolar Southern Ocean. The mean depth of the ocean is about 3800 m. In trenches, the ocean depth can exceed 10 000 m, but these cover only a small fraction of the surface area. The bathymetry is quite complex: There are mid-ocean ridges where tectonic plates drift apart and new seafloor is formed. There are trenches, where plates converge and one slab subducts beneath another slab. There are relatively smooth abyssal plains, separated from shallow continental shelves by steep continental slopes and rises. There are about 10 000 seamounts punctuating these abyssal plains. While some of the theories we will discuss assume the ocean to have vertical sidewalls, it is important to remember the adage: "the ocean has no sides, only a bottom."

The geoid If the ocean were at rest, of uniform density, and subjected to a uniform surface pressure, its surface would follow the geoid. The geoid is an equipotential surface that would be an ellipsoid of revolution (or spheroid) if there were no gravity anomalies. Inhomogeneities in the solid earth cause geoid deviations from a reference ellipsoid by about ±100 m. These deviations from the reference ellipsoid are much larger than the deviations from the geoid due to ocean dynamics. Precise knowledge of the geoid is thus needed to make measurements of the sea surface height useful to oceanographers.

Atmospheric forcing The ocean is forced primarily at its surface. Mechanical wind forcing generates both surface gravity waves and ocean currents. Shortwave radiation is absorbed in the upper few tens of meters, providing a heat source there. Heat is lost through longwave radiation, evaporative cooling, and molecular heat transfer to the atmosphere. Evaporation and precipitation add or subtract freshwater from the ocean, changing the surface salinity. The attendant mass changes are often negligible. The forcing varies on a wide range of time scales, often dominated by diurnal, synoptic, and seasonal variations. The atmospheric circulation shapes this forcing, but the ocean in turn forces the atmosphere, and the two fluids must be considered together. Such coupled dynamics are beyond the purview of this course—we will assume throughout that the forcing is external and prescribed.

Geothermal heat flux The interior of the earth generates a heat flux of about 50 TW to the surface. On average, the ocean receives about 0.1 W m^{-2}. This heat flux is concentrated along mid-ocean ridges, where the crust is young and thin. Compared to the surface heat fluxes, which are typically of order 10 or 100 W m^{-2}, this is a small flux. It nevertheless has some impact on the heat budget of the abyssal ocean.

Tidal forcing The ocean is subject to a time-varying gravitational field, caused predominantly by the sun and the moon. The resulting tidal forces generate tidal currents and perturbations to the sea level that are experienced on beaches and in ports. Tidal motion has long been thought of as simply superimposed on the steady or slowly evolving circulation of the ocean, and we will treat it as such in much of the course. Tidal forcing does appear to have a direct impact on the circulation of the abyssal ocean, however, which we will explore towards the end of the course.

1.2 Observing the ocean's state variables

The physical state of the ocean is almost completely described by the velocity field $\boldsymbol{u}$, the temperature field T, the salinity field S, the pressure field p, and the surface elevation h. These quantities are thus the primary target for observations. Pressure plays a special role: away from the surface, the pressure field is well-approximated by $p = -\rho_0 g z$, the background hydrostatic pressure, so pressure can be used as a proxy for depth. This is convenient because determining an instrument depth is otherwise difficult, although one forfeits measuring the dynamically important deviations from the background pressure field. What follows is an incomplete list of instruments and techniques that are commonly used to measure the ocean's physical state.

Current meters Ocean currents are typically measured using Vector Averaging Current Meters (VACMs) that consist of a rotor and a vane, Vector Measuring Current Meters (VMCMs) that consist of two orthogonally mounted rotors, and Acoustic Current Meters (ACMs) that take advantage of the Doppler shifting of sound waves by ocean currents. ACMs can be divided into two categories: ones that measure a travel times between transducers and ones that measure the Doppler shift in the frequency of reflected sound waves. The latter is the principle of widely used Acoustic Doppler Current Profilers (ADCPs). These emit four sound beams that get reflected by particles that are suspended in the water. The Doppler shift measured by each beam allows the determination of the velocity component in the direction of the respective beam. The three velocity components can be obtained from three beams—the fourth is used for redundancy and to estimate the error. These instruments can measure a profile of the velocity because they successively receive the backscatter from particles at increasing ranges. Current meters are often mounted on mooring lines and can be deployed for about a year. Spectral analysis of these moored measurements typically reveals broadband subinertial variability, spectral peaks at the local inertial and tidal frequencies, and again broadband variability at superinertial frequencies, typically attributed to an internal-wave continuum. ADCPs are also routinely mounted to the hulls of research vessels, giving current profiles along the ships' paths.

Drifters Surface currents are observed with instruments that drift with the water. The design varies in sophistication from pieces of parsnip (Richardson and Stommel, 1948) to a common one consisting of a GPS-tracked surface float tethered to a perforated drogue that anchors it to the currents at 15 m depth, minimizing the effects of wind dragging on the surface expression. The international Global Drifter Program maintains a global array that currently consists of about 1600 drifters. These drifters have a simple design and are easy to deploy. They yield a Lagrangian, i.e., flow-following, description of the ocean currents—in contrast to the Eulerian measurements obtained from moorings. Drifter trajectories are often highly convoluted, shaped by the chaotic dynamics of mesoscale eddies.

Floats Subsurface current can similarly be measured with instruments moving with the flow. The position of these floats must be determined acoustically, requiring the deployment of multiple sound sources that can be used for triangulation. The designations for drifters and floats are unfortunate but conventional. Drifters float, floats sink.

Niskin bottles Traditionally, water properties were sampled by bringing them back to the surface. The modern incarnation of this principle is the Niskin bottle, tens of which are typically mounted on a frame to form a rosette. These bottles are open on the top and bottom, such that water can freely flow through them. When lowered to the target depth, a triggering mechanism causes caps to seal off the top and bottom, trapping the water inside. Back on the deck of the ship, properties of these waters can be measured. These days, this is only used to measure accurate salinity standards to calibrate CTDs (see below) and to obtain chemical and biological samples.

Conductivity–temperature–depth packets CTDs are the workhorse of measuring the temperature and salinity structure of the ocean. They consist of a packet of a conductivity probe that is used to determine the salinity, taking advantage of its the known impact on the conductivity of seawater, a sensitive thermistor, and a pressure sensor. The pressure sensor is used to determine depth by using hydrostatic balance. CTDs are mounted to the same frames as Niskin bottles, yet they sample much more frequently and give finely resolved (about 1 m) temperature and salinity profiles. They contain considerable variability down to the sampling scale (called finestructure), revealing that the ocean is turbulent down to these small scales.

Argo floats CTDs are also mounted to Argo floats, autonomous floats that can change their buoyancy and thus profile the upper 2000 m of the ocean. The Argo program maintains an array of currently about 4000 such floats, each of which relays a temperature and salinity profile via satellite every ten days. Since the mid-2000s, this program has generated the vast majority of temperature measurements that are used to assess the rate of ocean warming in response to greenhouse gas forcing (e.g. Roemmich et al., 2015). More recently, floats that in most places can sample all the way to the seafloor have been designed (e.g. Johnson et al., 2020). In parallel, conventional Argo floats have increasingly been outfitted with beogeochemical sensors (e.g. Gray et al., 2018).

Gliders Like Argo floats, gliders actively control their buoyancy to rise or sink in the water column. Unlike Argo floats, which passively drift with the currents, gliders have wings that allow them to move forward when ascending or descending. Gliders can thus be piloted to follow a prescribed path, which can be adjusted through satellite communication when the glider surfaces. The buoyancy propulsion is very efficient and allows missions lasting several months. Sensors mounted on gliders include CTDs, biogeochemical sensors, turbulence probes, and hydrophones.

Satellite altimetry While the ocean is opaque to electromagnetic radiation, the atmosphere is largely transparent, which allows for remote sensing of the sea surface from space. Satellite altimetry used radar pulses that reflect off the ocean surface to measure the distance between the spacecraft and that surface. Precise knowledge of the spacecraft's position and of the geoid then allows the determination of the dynamically relevant deviation of the sea surface from the geopotential surface described by the geoid. These measurements are used to accurately map out the tides, to measure sea level rise, to globally map mesoscale eddies and their evolution, and to monitor El Niño.

Satellite gravimetry To infer the time-mean surface circulation from altimetric measurements, precise knowledge of the geoid is needed. The most accurate mapping of Earth's gravity anomalies currently available is obtained with satellite gravimetry (GRACE and GRACE-FO missions). Two satellites flying in tandem precisely measure the distance between one another, which changes in response to gravity anomalies experienced by the two spacecraft. These measurements are also used to track how much water has been added to the ocean from melting glaciers, which helps distinguish between sea level rise from mass addition and thermal expansion.

Acoustics The speed of sound in seawater depends on temperature, a property that can be exploited to infer the temperature from the time it takes a sound pulse to travel from a source to a receiver. This can be done at a 10 cm scale, allowing reciprocal transmission to measure both temperature and currents, and at a global scale. The sound speed structure of the ocean is such that there is a mid-depth waveguide, which allows sound waves to travel very long distances. One can exploit this to measure basin-scale ocean warming, although the transmission of sound pulses from active sources fell out of favor after a public outcry over perceived impacts on marine mammals. While acoustics have long been used extensively by navies, its full potential has yet to be realized for basic science.

Inverse methods Ocean observations often become much more useful if they can be combined with *a priori* knowledge. For example, satellite altimetry measures the sea surface elevation, but currents can be inferred using geostrophic balance. The idea to combine measurements with equations describing known physical constraints can be generalized substantially and gives rise to very powerful inverse methods. Such methods allow one to combine different kinds of data (e.g. temperature, salinity, pressure, and silicate concentrations along a hydrographic section) with physical constraints (e.g. thermal-wind balance, mass and tracer conservation) to arrive at improved estimates of a field of interest (e.g. the flow and tracer transport across the section). Taken to the extreme, a full ocean model can be fit to the available data, a practice known as “state estimation” (e.g., Wunsch and Heimbach, 2007). See Wunsch (2006) for a detailed account.

Chapter 2

Gyre and thermocline theory

In ESE 130, we discussed the most basic properties of ocean gyres. We considered a constant-density ocean subjected to a wind stress at its surface and to a simple form of bottom stress at a flat seafloor. Assuming planetary-geostrophic scaling, we derived Stommel's equation for the streamfunction of the depth-integrated flow:

$$\beta \frac{\partial \Psi}{\partial x} = \frac{1}{\rho} \boldsymbol{z} \cdot (\nabla \times \boldsymbol{\tau}) - r \left(\frac{\partial^2 \Psi}{\partial x^2} + \frac{\partial^2 \Psi}{\partial y^2} \right). \tag{2.1}$$

If the bottom friction is weak, the last term is negligible and the equation reduces to Sverdrup's balance. We saw that the friction term does become important in a boundary layer at the western edge of the basin, where a western boundary current emerges. We derived an approximate solution to this equation for a simple ocean basin subjected to a simple wind profile (Fig. 2.1).

Stommel's gyre theory has two major shortcomings: it neglects the effects of topography and of density variations. Under some conditions, the effects of topography can be understood with relative ease, which we discuss next. Once density variations are considered, however, the problem becomes much more complicated. The task to calculate the gyre circulation then becomes intimately tied to the task to determine the stratification of the upper ocean. The resulting theories go by the name of "thermocline theories." They are more easily formulated for discrete layers, so we will consider general layer equations in an interlude.

2.1 Effects of topography and baroclinicity

Our goal here is to develop a theory for the vertically integrated flow that generalizes Stommel's equation to take into the account the effects of topography and density variations. We begin with the Boussinesq equations in planetary-geostrophic scaling. In analogy to our derivation for the shallow-water system, these equations arise by making the scaling assumptions

$$\varepsilon \ll 1 \quad \text{and} \quad \varepsilon \varrho \sim 1, \tag{2.2}$$

where $\varepsilon = U/fL$ is the Rossby number, and $\varrho = L^2/\lambda^2$ with $\lambda = NH/f$ is the Burger number. The inviscid planetary-geostrophic equations are

$$-fv = -\frac{1}{\rho_0}\frac{\partial p}{\partial x}, \qquad fu = -\frac{1}{\rho_0}\frac{\partial p}{\partial y}, \qquad b = \frac{1}{\rho_0}\frac{\partial p}{\partial z}, \tag{2.3}$$

$$\frac{\partial u}{\partial x} + \frac{\partial v}{\partial y} + \frac{\partial w}{\partial z} = 0, \qquad \frac{\partial b}{\partial t} + \boldsymbol{u}\cdot\nabla b = 0, \tag{2.4}$$

where b describes the full buoyancy field, i.e., we did not separate out a background stratification like we did in the quasi-geostrophic system. The planetary-geostrophic system consists of geostrophic balance with the full latitude-dependent Coriolis parameter, hydrostatic balance, the continuity equation, and a fully nonlinear buoyancy equation. This set of equations conserves the planetary-geostrophic potential vorticity $q = f\,\partial b/\partial z$, as can be verified by combining the vorticity equation $\beta v = f\,\partial w/\partial z$ with a vertical derivative of the buoyancy equation, taking advantage of thermal-wind balance.

To be able to incorporate wind forcing and bottom drag, we augment the horizontal momentum equations with turbulent momentum transfer terms:

$$-fv = -\frac{1}{\rho_0}\frac{\partial p}{\partial x} + \frac{\partial}{\partial z}\left(\nu\frac{\partial u}{\partial z}\right), \tag{2.5}$$

$$fu = -\frac{1}{\rho_0}\frac{\partial p}{\partial y} + \frac{\partial}{\partial z}\left(\nu\frac{\partial v}{\partial z}\right). \tag{2.6}$$

We integrate these equations from the seafloor at $z = H$, which can now be a function of x and y, to the sea surface. The sea surface is located at $z = h$, but the deviations from $z = 0$ are small compared to the depth of the fluid, such that we can integrate to $z = 0$ instead. We obtain

$$-fV = -\frac{1}{\rho_0}\int_{-H}^{0}\frac{\partial p}{\partial x}\,\mathrm{d}z + \frac{\tau^x}{\rho_0} - rU, \tag{2.7}$$

$$fU = -\frac{1}{\rho_0}\int_{-H}^{0}\frac{\partial p}{\partial y}\,\mathrm{d}z + \frac{\tau^y}{\rho_0} - rV, \tag{2.8}$$

where U and V are the vertically integrated flow, and we used the same bottom stress condition as in Stommel's theory. The reason we do not simply recover Stommel's theory is that we cannot exchange the order of integration and differentiation in the pressure terms because the depth H varies, as does the pressure at the seafloor. Using the Leibniz rule, we obtain

$$\frac{1}{\rho_0}\int_{-H}^{0}\frac{\partial p}{\partial x}\,\mathrm{d}z = \frac{1}{\rho_0}\frac{\partial}{\partial x}\int_{-H}^{0} p\,\mathrm{d}z - \frac{p_\mathrm{B}}{\rho_0}\frac{\partial H}{\partial x}, \tag{2.9}$$

where $p_\mathrm{B} = p(x, y, -H)$ is the bottom pressure. Using integration by parts, we can further develop this term into

$$\frac{1}{\rho_0}\int_{-H}^{0}\frac{\partial p}{\partial x}\,\mathrm{d}z=\frac{1}{\rho_0}\frac{\partial}{\partial x}\left(Hp_\mathrm{B}-\int_{-H}^{0}z\frac{\partial p}{\partial z}\,\mathrm{d}z\right)-\frac{p_\mathrm{B}}{\rho_0}\frac{\partial H}{\partial x}=\frac{H}{\rho_0}\frac{\partial p_\mathrm{B}}{\partial x}-\frac{\partial}{\partial x}\int_{-H}^{0}z\,b\,\mathrm{d}z, \tag{2.10}$$

where we used hydrostatic balance in the last step. Introducing the short-hand notation

$$\gamma=-\int_{-H}^{0}z\,b\,\mathrm{d}z \tag{2.11}$$

and writing the vertically integrate flow using the streamfunction Ψ, the momentum equations thus become

$$-\frac{f}{H}\frac{\partial\Psi}{\partial x}=-\frac{1}{\rho_0}\frac{\partial p_\mathrm{B}}{\partial x}-\frac{1}{H}\frac{\partial\gamma}{\partial x}+\frac{\tau^x}{\rho_0 H}+\frac{r}{H}\frac{\partial\Psi}{\partial y}, \tag{2.12}$$

$$-\frac{f}{H}\frac{\partial\Psi}{\partial y}=-\frac{1}{\rho_0}\frac{\partial p_\mathrm{B}}{\partial y}-\frac{1}{H}\frac{\partial\gamma}{\partial y}+\frac{\tau^y}{\rho_0 H}-\frac{r}{H}\frac{\partial\Psi}{\partial x}. \tag{2.13}$$

Cross-differentiating these equations then eliminates the bottom pressure terms and yields

$$-\mathrm{J}\left(\frac{f}{H},\Psi\right)=-\mathrm{J}\left(\frac{1}{H},\gamma\right)+\frac{1}{\rho_0}\boldsymbol{z}\cdot\left(\nabla\times\frac{\boldsymbol{\tau}}{H}\right)-\frac{\partial}{\partial x}\left(\frac{r}{H}\frac{\partial\Psi}{\partial x}\right)-\frac{\partial}{\partial y}\left(\frac{r}{H}\frac{\partial\Psi}{\partial y}\right). \tag{2.14}$$

This is the generalization of Stommel's equation to the case with topography and baroclinicity.

The term on the left of (2.14) simplifies to $\beta V/H$ if H is constant. Instead of describing the transport across the gradient in planetary vorticity f, this term now describes the transport across gradients in f/H. Lines of constant f/H therefore play the same role as lines of constant f in Stommel's flat-bottom theory: wind stress curl induces transport across these lines. This is intuitive because the topography allows fluid columns to stretch or squash; f/H is the potential vorticity of the fluid layer. Transport along these lines does not require forcing, just like zonal transport does not require forcing in the case with a flat bottom.

The first term on the right of (2.14) describes the joint effect of baroclinicity and relief (JEBAR), and it constitutes a major complication. This term depends on the buoyancy field b, so it couples the dynamics of the vertically integrated transport to the three-dimensional structure of the buoyancy field, which in turn depends on the three-dimensional structure of the flow field. In general, one has to calculate three-dimensional solutions to the planetary-geostrophic equations, a formidable task given the nonlinearity in the buoyancy equation. This task falls under the purview of thermocline theory and is a major nuisance if one is interested in the vertically integrated flow only.

The JEBAR term disappears under certain conditions. First, if the bottom is flat, the first argument in the Jacobian is a constant, and the term is identically zero. Second, if buoyancy is a function of z only, γ can be understood as a function of H. In that case, the Jacobian also vanishes, because both arguments are functions of H:

$$\mathrm{J}\left(\frac{1}{H},\gamma(H)\right)=-\frac{\gamma'(H)}{H^2}\left(\frac{\partial H}{\partial x}\frac{\partial H}{\partial y}-\frac{\partial H}{\partial y}\frac{\partial H}{\partial x}\right)=0, \tag{2.15}$$

where γ' denotes the derivative of γ with respect to H. If one of these conditions is satisfied, the vertically integrated circulation does decouple from the buoyancy field and can be determined by solving the two-dimensional problem resulting from (2.14). It should be pointed out, however, that dropping the JEBAR term is not always warranted: doing so tends to overemphasize the effect of topography in a stratified ocean.

The second term on the right of (2.14) is the forcing term. It is now proportional to the curl not of the wind stress $\boldsymbol{\tau}$ but of $\boldsymbol{\tau}/H$. This implies, for example, that a uniform wind stress can generate a depth-integrated transport.

The final two terms on the right of (2.14) are due to bottom friction. The particular form of these terms is the result of our somewhat peculiar choice to make the bottom stress proportional to the depth-integrated flow. While these terms capture the basic physics of bottom friction, properties of the solutions to (2.14) that depend sensitively on the form of friction should be taken with a grain of salt.

If the JEBAR term can be neglected, topography exerts an important control on the gyre circulation. Consider an example in which the seafloor rises to the surface at the zonal edges of an otherwise flat ocean basin (Fig. 2.2). The f/H contours, while zonal in the flat part of the basin, take a sharp southward turn near the boundaries. This has a drastic impact on the western boundary current that would occupy this location in an ocean with a flat bottom (Fig. 2.1). Instead of a frictionally controlled boundary current, we now have a topographically steered current: the transport, while strong, largely follows f/H contours. It is only at the southern boundary of the basin, where there is still a vertical sidewall, that friction becomes dominant and a frictionally controlled current persists.

This example bears some resemblance to the real western boundary currents. The margins of ocean basins consist of continental slopes and rises, not unlike in our example. The real Gulf Stream and Kuroshio, for example, largely follow contours of f/H while flowing along the continental margins. They do separate from the continental margins, however, and extend into the basins' interiors. This is understood to be due to inertial effects, which we neglected by considering the inertia-less planetary-geostrophic system.

We can build further intuition for the depth-integrated wind-driven circulation of a depth-variable ocean by drawing an analogy to the advection and diffusion of a passive tracer. Dropping the JEBAR term and changing the sign turns (2.14) into

$$\mathrm{J}\left(\frac{f}{H},\Psi\right)=-\frac{1}{\rho_0}\boldsymbol{z}\cdot\left(\nabla\times\frac{\boldsymbol{\tau}}{H}\right)+\frac{\partial}{\partial x}\left(\frac{r}{H}\frac{\partial\Psi}{\partial x}\right)+\frac{\partial}{\partial y}\left(\frac{r}{H}\frac{\partial\Psi}{\partial y}\right). \tag{2.16}$$

This equation has the same form as the equation satisfied by a tracer field c that is advected by a two-dimensional flow described by the streamfunction ψ, that has a

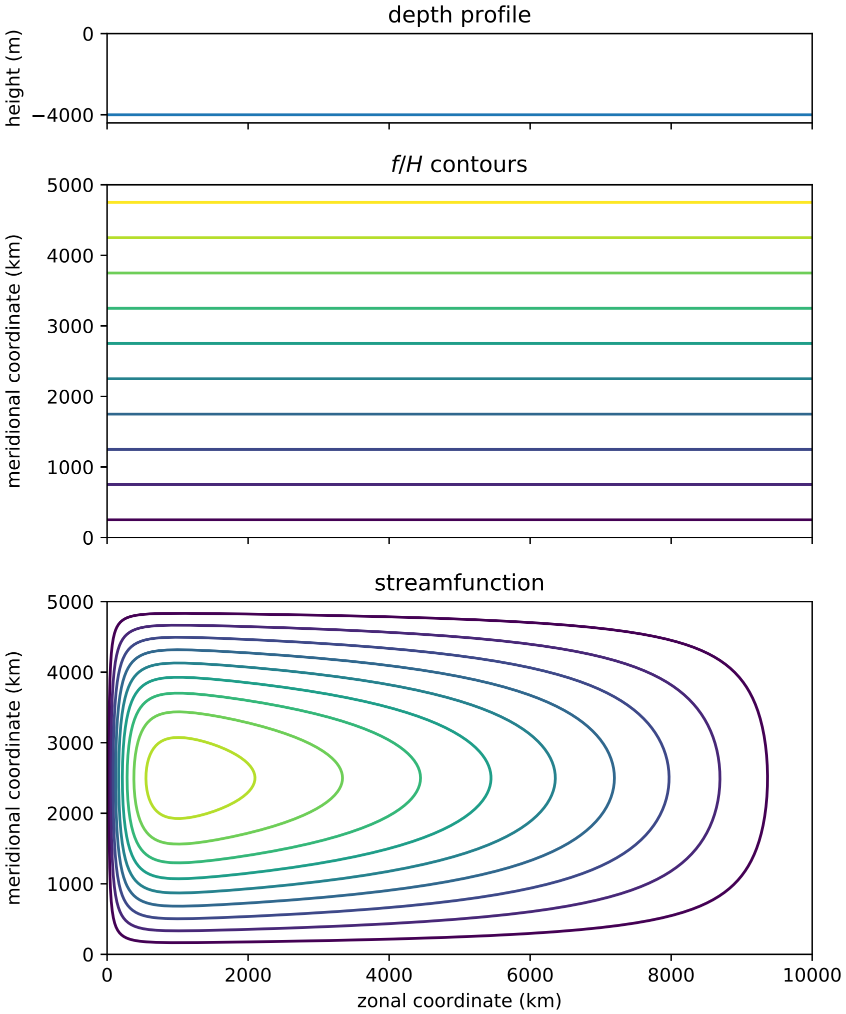

Figure 2.1: Gyre transport for a flat bottom. The solution is calculated for a wind stress $\tau^x = -\tau_0 \cos \pi y/L_y$ and a β-plane. The following parameters are used: $\tau_0 = 0.1\ \mathrm{N\,m^{-2}}$, $f_0 = 10^{-4}\ \mathrm{s^{-1}}$, $\beta = 2 \times 10^{-11}\ \mathrm{s^{-1}\ m^{-1}}$, $r = 5 \times 10^{-6}\ \mathrm{s^{-1}}$, $L_x = 10\,000$ km, $L_y = 5000$ km.

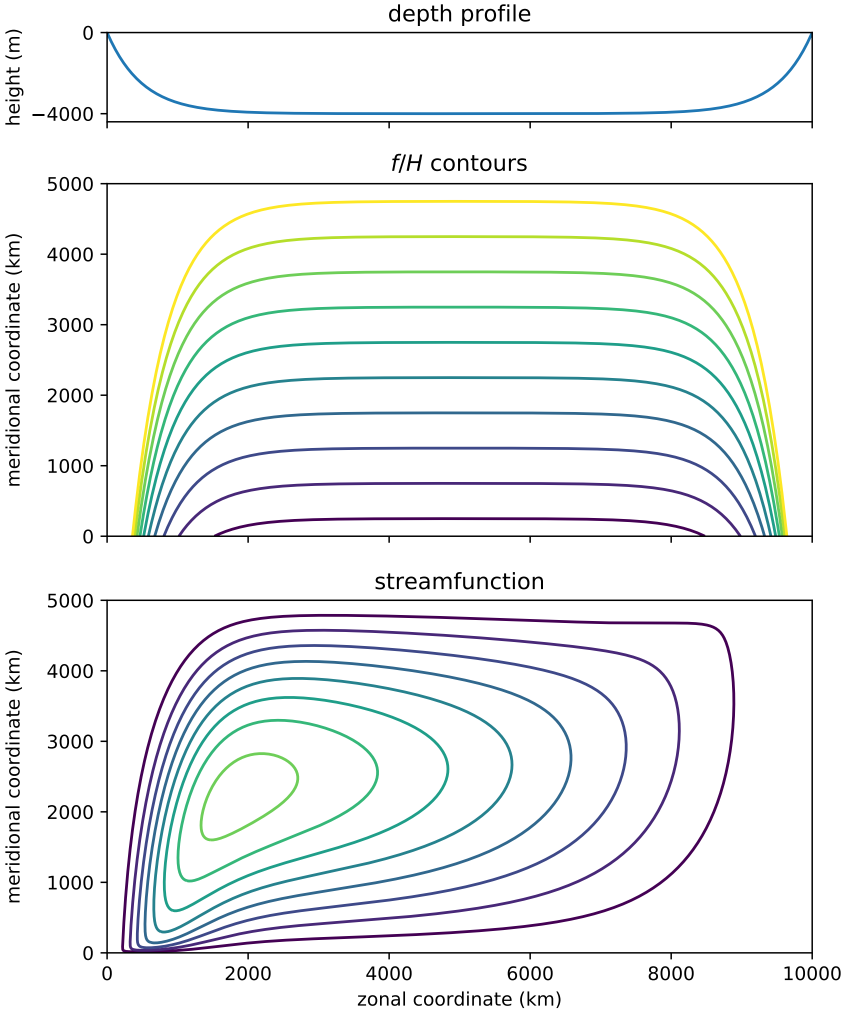

Figure 2.2: Gyre transport for a basin with a bottom that is sloping up at the zonal boundaries. The solution is calculated for depth $H = H_0(1 - e^{-x/d} - e^{(x+L_x)/d} + 2e^{-L_x/d})$ and a wind stress $\tau^x = -\tau_0 \cos \pi y / L_y$ and a β-plane. The following parameters are used: $H_0 = 4000$ m, $d = 500$ km, $\tau_0 = 0.1$ N m^{-2}, $f_0 = 10^{-4}$ s^{-1}, $\beta = 2 \times 10^{-11}$ s^{-1} m^{-1}, $r = 5 \times 10^{-6}$ s^{-1}, $L_x = 10\,000$ km, $L_y = 5000$ km.

source Q_c, that is diffused with a diffusivity κ, and that has reached steady state. The tracer equation is

$$\frac{\partial c}{\partial t} + \mathrm{J}(\psi, c) = Q_c + \frac{\partial}{\partial x}\left(\kappa \frac{\partial c}{\partial x}\right) + \frac{\partial}{\partial y}\left(\kappa \frac{\partial c}{\partial y}\right), \tag{2.17}$$

which in steady state turns into (2.16) if we make the identification

$$c \longleftrightarrow \Psi, \qquad \psi \longleftrightarrow \frac{f}{H}, \qquad Q_c \longleftrightarrow -\frac{1}{\rho_0}\boldsymbol{z} \cdot \left(\nabla \times \frac{\boldsymbol{\tau}}{H}\right), \qquad \kappa \longleftrightarrow \frac{r}{H}. \tag{2.18}$$

We can therefore think of the streamfunction of the vertically integrated flow Ψ as being a tracer that has a source proportional to the curl of $\boldsymbol{\tau}/H$, that is advected by a flow that is described by the streamfunction f/H, and that is diffused with a diffusivity r/H. The boundary conditions are $\Psi = 0$, enforcing a constant tracer concentration at the boundaries of the domain.

Let us consider the flat-bottom case as an example. The usual subtropical negative wind stress curl corresponds to a positive source in the tracer analogy. This tracer is advected westward because the zonal and meridional components of the advecting flow are

$$-\frac{\partial}{\partial y}\left(\frac{f}{H}\right) = -\frac{\beta}{H} \quad \text{and} \quad \frac{\partial}{\partial x}\left(\frac{f}{H}\right) = 0. \tag{2.19}$$

As hypothetical fluid parcels in this analogy are advected westward, they pick up more and more tracer concentration, which leads to a linear westward concentration increase starting from $\Psi = 0$ on the eastern boundary. Near the western boundary, the tracer must diffusively adjust back to $\Psi = 0$, which leads to a strong tracer gradient. The result is the familiar streamfunction field of Stommel's gyre solution (Fig. 2.1).

Now consider the case with continental margins (Fig. 2.2). The tracer is now advected along lines of constant f/H, which emanate from the southern boundary in the eastern half of the domain. The tracer concentration increases along these f/H contours as more and more concentration is received from the forcing along the hypothetical parcels' trajectories. On the western continental margin, the f/H contours turn south, so the tracer concentration field is swept south as well. Diffusion is only needed where f/H contours run into the southern boundary in the western part of the domain. Here, a diffusive layer adjusts the concentration to $\Psi = 0$. This boundary layer is thinner than that on the western boundary in the flat-bottom case because the hypothetical flow advecting the tracer is faster: in the boundary layer, diffusive transports must balance the advective transport, so stronger advection requires sharper tracer gradients.

Another useful way to think about the wind-driven circulation is with the use of Green's functions. We can think of the wind stress forcing as consisting of a superposition of point sources, and the circulation as the superposition of the responses to these point sources. In the tracer analogy, the Green's function corresponds to the tracer field induced by a (negative) point source of the tracer. The hypothetical flow along f/H contours advects this tracer downstream, inducing a plume that is slowly spreading out due to the effect of diffusion (Fig. 2.3). This advection is westward if the bottom is flat,

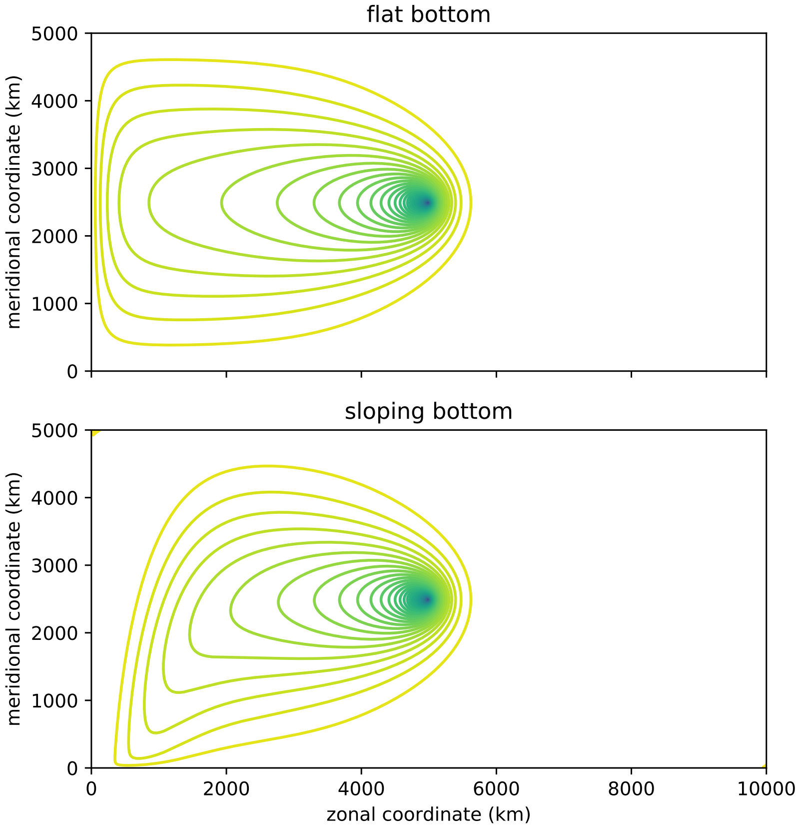

Figure 2.3: Circulation in response to a point source of wind stress curl, a.k.a. β-plumes. The topography in the lower panel is the same as in Fig. 2.2.

but it can be distorted by topography. The tracer analogy has led oceanographers to refer to these Green's functions as β-plumes.

The impact of bottom topography can also be understood through the lens of momentum transfer between the ocean and the solid earth through "bottom form drag." We return to the vertically integrated momentum equations (2.7) and (2.8). Applying the Leibniz rule as in (2.9) yields

$$-fV = -\frac{1}{\rho_0}\frac{\partial}{\partial x}\int_{-H}^{0} p\,\mathrm{d}z + \frac{p_\mathrm{B}}{\rho_0}\frac{\partial H}{\partial x} + \frac{\tau^x}{\rho_0} - rU, \tag{2.20}$$

$$fU = -\frac{1}{\rho_0}\frac{\partial}{\partial y}\int_{-H}^{0} p\,\mathrm{d}z + \frac{p_\mathrm{B}}{\rho_0}\frac{\partial H}{\partial y} + \frac{\tau^y}{\rho_0} - rV. \tag{2.21}$$

Instead of proceeding as before, we now pause and consider the physical meaning of terms involving the bottom pressure. They tell us that there can be sources or sinks of vertically integrated momentum if there are correlations between the bottom pressure and the bottom slope. As an example, consider a ridge running in the meridional direction. If there is a zonal eastward flow, one would expect the bottom pressure to be elevated on the western flank of the ridge and reduced on the eastern flank. Since $\partial H/\partial x < 0$ on the western flank and $\partial H/\partial x > 0$ on the eastern flank, this configuration leads to a loss of eastward momentum—or rather a transfer of eastward momentum from the ocean to the solid earth below. This phenomenon, which does not require any friction, is called "bottom form drag."

Cross-differentiating (2.20) and (2.21) gives a vorticity equation for the vertically integrated flow:

$$\beta V = \frac{1}{\rho_0}\left(\frac{\partial p_\mathrm{B}}{\partial x}\frac{\partial H}{\partial y} - \frac{\partial p_\mathrm{B}}{\partial y}\frac{\partial H}{\partial x}\right) + \frac{1}{\rho_0}\boldsymbol{z}\cdot(\nabla\times\boldsymbol{\tau}) - r\left(\frac{\partial V}{\partial x} - \frac{\partial U}{\partial y}\right). \tag{2.22}$$

This is the same as Stommel's equations except for the appearance of the term involving the bottom pressure. This is the torque applied to the fluid by the bottom form drag and is called the "bottom pressure torque." To solve this equation, we require knowledge of the bottom pressure field, which in general couples this equation to the three-dimensional buoyancy field, so this major complication did not magically disappear.

2.2 Layer equations

Both theories on the vertical structure of the gyre circulation that we will discuss below idealize the ocean's stratification into a small number of homogeneous layers, i.e., layers in which the density is uniform. This simplification has proved crucial to make the mathematics tractable. The dynamics revealed by these theories can be generalized to a continuous system, but the core physics of the thermocline circulation is most transparently revealed in these systems with a small number of layers.

We consider a general system of stacked layers with buoyancies $b_1, \dots, b_n$. Breaking with oceanographic tradition, we assign numbers to the layers starting from the bottom, such that an increasing index corresponds to an increased vertical coordinate z. We make the hydrostatic approximation, such that in a given layer, we can write the pressure field as ($i = 1, \dots, n$)

$$p(x, y, z, t) = p_i(x, y, t) + \rho_0 b_i z. \tag{2.23}$$

The uniform buoyancy within the layers implies that horizontal pressure gradients are vertically constant across the layers. Consequently, the horizontal velocities remain constant across layers if they are so initially. We therefore have a set of two-dimensional momentum equations:

$$\frac{\partial u_i}{\partial t} + u_i \frac{\partial u_i}{\partial x} + v_i \frac{\partial u_i}{\partial y} - f v_i = -\frac{1}{\rho_0} \frac{\partial p_i}{\partial x}, \tag{2.24}$$

$$\frac{\partial v_i}{\partial t} + u_i \frac{\partial v_i}{\partial x} + v_i \frac{\partial v_i}{\partial y} + f u_i = -\frac{1}{\rho_0} \frac{\partial p_i}{\partial y}. \tag{2.25}$$

Denoting the layer heights by h_i, we obtain from mass conservation:

$$\frac{\partial h_i}{\partial t} + \frac{\partial}{\partial x}(u_i h_i) + \frac{\partial}{\partial y}(v_i h_i) = 0. \tag{2.26}$$

The layers are coupled through the pressure terms: the pressure at the interface between layers must match. We will return to this matching condition.

The layer equations above layer-wise conserve potential vorticity. In both theories discussed below, potential vorticity takes center stage. We therefore derive a general conservation statement for layer potential vorticity and subsequently specialize to the quasi-geostrophic and planetary-geostrophic systems.

Upon cross-differentiating the momentum equations (2.24) and (2.25), we find the vorticity equation

$$\begin{aligned}\frac{\partial \zeta_i}{\partial t} &+ u_i \frac{\partial \zeta_i}{\partial x} + v_i \frac{\partial \zeta_i}{\partial y} \\ &+ \frac{\partial u_i}{\partial x}\frac{\partial v_i}{\partial x} + \frac{\partial v_i}{\partial x}\frac{\partial v_i}{\partial y} - \frac{\partial u_i}{\partial y}\frac{\partial u_i}{\partial x} - \frac{\partial v_i}{\partial y}\frac{\partial u_i}{\partial y} + \beta v_i + f\left(\frac{\partial u_i}{\partial x} + \frac{\partial v_i}{\partial y}\right) = 0.\end{aligned} \tag{2.27}$$

This can be written as

$$\left(\frac{\partial}{\partial t} + u_i \frac{\partial}{\partial x} + v_i \frac{\partial}{\partial y}\right)(f + \zeta_i) + (f + \zeta_i)\left(\frac{\partial u_i}{\partial x} + \frac{\partial v_i}{\partial y}\right) = 0. \tag{2.28}$$

From mass conservation, we have

$$\frac{\partial h_i}{\partial t} + u_i \frac{\partial h_i}{\partial x} + v_i \frac{\partial h_i}{\partial y} + h_i \left(\frac{\partial u_i}{\partial x} + \frac{\partial v_i}{\partial y}\right) = 0. \tag{2.29}$$

We can combine these two equations by dividing the vorticity equation by h_i, yielding

$$\frac{1}{h_i}\left(\frac{\partial}{\partial t}+u_i\frac{\partial}{\partial x}+v_i\frac{\partial}{\partial y}\right)(f+\zeta_i)+\frac{f+\zeta_i}{h_i}\left(\frac{\partial u_i}{\partial x}+\frac{\partial v_i}{\partial y}\right)=0, \tag{2.30}$$

and multiplying the mass conservation equation by $-(f+\zeta_i)/h_i^2$, yielding

$$(f+\zeta_i)\left(\frac{\partial}{\partial t}+u_i\frac{\partial}{\partial x}+v_i\frac{\partial}{\partial y}\right)\left(\frac{1}{h_i}\right)-\frac{f+\zeta_i}{h_i}\left(\frac{\partial u_i}{\partial x}+\frac{\partial v_i}{\partial y}\right)=0. \tag{2.31}$$

We obtain the conservation of layer potential vorticity by adding the latter two equations:

$$\frac{\partial q_i}{\partial t}+u_i\frac{\partial q_i}{\partial x}+v_i\frac{\partial q_i}{\partial y}=0 \quad \text{with} \quad q_i=\frac{f+\zeta_i}{h_i}. \tag{2.32}$$

In the absence of forcing, each layer conserves q_i by trading off between planetary vorticity, relative vorticity, and stretching. In the following, we approximate this conservation law following first planetary-geostrophic scaling, then quasi-geostrophic scaling. Our derivation is somewhat informal, but the result is the same as a more formal derivation following the same asymptotic analysis template used previously for the one-layer shallow-water system.

In planetary-geostrophic scaling, the smallness of the Rossby number implies that the relative vorticity is negligible compared to the planetary vorticity: $|\zeta_i| \ll |f|$. The scaling for the length scales translates into variations of layer thickness being of the same order as the layer thicknesses themselves. In fact, layer thicknesses can vanish in parts of the domain, as we will encounter in the theory of the ventilated thermocline. The potential vorticity in the planetary-geostrophic scaling therefore becomes

$$q_i=\frac{f}{h_i}. \tag{2.33}$$

This form is equivalent to the conservation of f/H we encountered in the theory for the vertically integrated gyre flow if baroclinicity, forcing, and friction are negligible.

In the quasi-geostrophic scaling, the Rossby number is also small, such that $|\zeta_i| \ll |f|$. We further assume that variations of the planetary vorticity are of the same order as the Rossby number, i.e., if $f=f_0+\beta y$, $|\beta y| \ll |f_0|$. The restriction to flow at scales of the same order as the deformation radius translates into layer thickness variations being much smaller than mean layer thicknesses. If we write $h_i=H_i+h_i'$, then $|h_i'| \ll H_i$. In quasi-geostrophic scaling, layer thicknesses can be perturbed only slightly. This is an important restriction because it means that the stratification is largely determined once the mean layer thicknesses H_i are prescribed. The stratification, like in the continuous case in the form of N^2, is externally prescribed and not determined as part of the solution. A quasi-geostrophic theory can therefore not explain the stratification of the thermocline itself. It is nevertheless a powerful tool to examine the circulation's horizontal and vertical structure, as well as perturbations to that stratification, once its background structure is presumed.

Given these assumptions, we can approximate the potential vorticity with

$$q_i = \frac{f_0 + \beta y + \zeta_i}{H_i + h_i'} \approx \frac{f_0 + \beta y + \zeta_i}{H_i}\left(1 - \frac{h_i'}{H_i}\right) \approx \frac{1}{H_i}\left(f_0 + \beta y + \zeta_i - \frac{f_0 h_i'}{H_i}\right). \tag{2.34}$$

Since H_i and f_0 are constants, this implies that the layer quasi-geostrophic potential vorticity $\beta y + \zeta_i - f_0 h_i'/H_i$ is conserved. We complement this conservation law with an inversion statement that relates this quasi-geostrophic potential vorticity to the geostrophic streamfunction $\psi_i = p_i/\rho_0 f_0$. First, we assume that the horizontal flow is geostrophically balanced (to leading order), such that

$$\zeta_i = \frac{\partial v_i}{\partial x} - \frac{\partial u_i}{\partial y} = \frac{\partial^2 \psi_i}{\partial x^2} + \frac{\partial^2 \psi_i}{\partial y^2}. \tag{2.35}$$

Second, we need to relate the layer thickness variations h_i' to the geostrophic streamfunction. We do this by matching the pressure across the layer interfaces. If we denote the position of the interface between layer i and layer $i+1$ as z_i, we obtain the matching condition

$$p_i + \rho_0 b_i z_i = p_{i+1} + \rho_0 b_{i+1} z_i \quad \text{or} \quad z_i = -\frac{1}{\rho_0}\frac{p_{i+1} - p_i}{b_{i+1} - b_i} = -f_0 \frac{\psi_{i+1} - \psi_i}{b_{i+1} - b_i}. \tag{2.36}$$

The denominator $b_{i+1} - b_i = g(\rho_i - \rho_{i+1})/\rho_0$ is called the "reduced gravity" of the associated layer interface. It is important to remember that these numbers are externally prescribed. They are part of prescribing the background stratification. The first layer, which touches the seafloor at $z = -H$, then has a thickness

$$h_1 = z_1 + H = -f_0 \frac{\psi_2 - \psi_1}{b_2 - b_1} + H; \tag{2.37}$$

interior layers have a thickness

$$h_i = z_i - z_{i-1} = -f_0 \left(\frac{\psi_{i+1} - \psi_i}{b_{i+1} - b_i} - \frac{\psi_i - \psi_{i-1}}{b_i - b_{i-1}}\right); \tag{2.38}$$

and the surface layer, which we will assume is bounded by a rigid sea surface at $z = 0$, has a thickness

$$h_n = -z_{n-1} = f_0 \frac{\psi_n - \psi_{n-1}}{b_n - b_{n-1}}. \tag{2.39}$$

Dropping all additive constants and a common constant factor $1/H_i$, both of which are inconsequential for the conservation laws, we find that the following layer quasi-geostrophic potential vorticities are conserved ($\tilde{q}_i = H_i q_i - f_0$):

$$\tilde{q}_1 = \beta y + \frac{\partial^2 \psi_1}{\partial x^2} + \frac{\partial^2 \psi_1}{\partial y^2} + \frac{f_0^2}{H_1}\frac{\psi_2 - \psi_1}{b_2 - b_1} - \frac{f_0 H}{H_1}, \tag{2.40}$$

$$\tilde{q}_i = \beta y + \frac{\partial^2 \psi_i}{\partial x^2} + \frac{\partial^2 \psi_i}{\partial y^2} + \frac{f_0^2}{H_i}\left(\frac{\psi_{i+1} - \psi_i}{b_{i+1} - b_i} - \frac{\psi_i - \psi_{i-1}}{b_i - b_{i-1}}\right), \tag{2.41}$$

$$\tilde{q}_n = \beta y + \frac{\partial^2 \psi_n}{\partial x^2} + \frac{\partial^2 \psi_n}{\partial y^2} - \frac{f_0^2}{H_n}\frac{\psi_n - \psi_{n-1}}{b_n - b_{n-1}}. \tag{2.42}$$

Like in the shallow-water system and the continuous system considered previously, the quasi-geostrophic potential vorticity consists of a planetary-vorticity term, a relative-vorticity term, and a stretching term. The bottom layer includes a stretching term due to topography, which would drop out for a flat bottom. The stretching term has some resemblance to that in the continuous system: it can be thought of as a finite-difference approximation to that continuous term. It should be noted, however, that a fluid that consists of a stack of homogeneous layers is at least in principle physically realizable.

The equations (2.40) to (2.42) form the inversion statement of the layered quasi-geostrophic system. The conservation statement can be written succinctly as

$$\frac{\partial \tilde{q}_i}{\partial t} + \mathrm{J}(\psi_i, \tilde{q}_i) = 0. \tag{2.43}$$

Layer quasi-potential vorticity is conserved under advection by the geostrophic flow in each layer. We will drop the tildes in what follows because it will be clear from context that we are working with quasi-geostrophic potential vorticities.

2.3 The vertical structure of gyres and potential-vorticity homogenization

We are now ready to begin our discussion of the vertical structure of wind-forced gyres. We start with a quasi-geostrophic theory, which cannot explain why the thermocline stratification is there to begin with, but it can tell us how a given stratification affects the gyre circulation and is modified by that circulation. This theory was developed by Rhines and Young (1982a) and Rhines and Young (1982b).

We consider an ocean that consists of two layers, the simplest representation of a stratification. The total depth of the ocean is H, and each layer has a mean thickness $H/2$. The ocean is forced by a wind stress that generates an Ekman pumping velocity

$$w_{\mathrm{Ek}} = w_0 \sin \frac{\pi y}{L}. \tag{2.44}$$

Our ocean extends from $y = -L$ to $y = L$, so it contains both Ekman pumping in the subtropics ($y < 0$) and Ekman suction in the subpolar region ($y > 0$). The zonal extent of the ocean basin is from $x = 0$ to $x = L$.

We assume the bottom is flat and frictionless, which prevents us from closing the circulation at the western boundary. In what follows, we focus on the interior of the gyre, but western boundary currents closing the circulation are implied.

Ekman pumping adds mass to the top layer, Ekman suction removes mass from it. This manifests as a source term in the potential-vorticity budget of the upper layer:

$$\frac{\partial q_2}{\partial t} + \mathrm{J}(\psi_2, q_2) = \frac{f_0 w_{\mathrm{Ek}}}{H/2}. \tag{2.45}$$

The lower layer is shielded from the atmospheric forcing by the upper layer, so potential vorticity is conserved there:

$$\frac{\partial q_1}{\partial t} + \mathrm{J}(\psi_1, q_1) = 0. \tag{2.46}$$

Despite not being forced directly by the atmosphere, we will see below that the lower layer is still set into motion. The potential vorticities of the two layers are

$$q_1 = \beta y + \frac{\partial^2 \psi_1}{\partial x^2} + \frac{\partial^2 \psi_1}{\partial y^2} + \frac{2}{\lambda^2}(\psi_2 - \psi_1), \tag{2.47}$$

$$q_2 = \beta y + \frac{\partial^2 \psi_2}{\partial x^2} + \frac{\partial^2 \psi_2}{\partial y^2} - \frac{2}{\lambda^2}(\psi_2 - \psi_1), \tag{2.48}$$

where $\lambda^2 = g'H/f_0^2$ is the square of the deformation radius of the two-layer system, and $g' = b_2 - b_1$ is its reduced gravity. For the ocean, this deformation radius is of order 100 km, much smaller than the scale of the gyres we aim to describe. At scales much larger than the deformation radius, the relative vorticity is negligible compared to the stretching term, such that we can approximate the potential vorticities by

$$q_1 = \beta y + \frac{2}{\lambda^2}(\psi_2 - \psi_1), \tag{2.49}$$

$$q_2 = \beta y - \frac{2}{\lambda^2}(\psi_2 - \psi_1). \tag{2.50}$$

It should be noted that we are violating quasi-geostrophic scaling here: in the derivation of the quasi-geostrophic system, we assumed that the scale of motion is comparable to the deformation radius. We proceed without heeding this warming, and we will find that the resulting solutions do explain some of the qualitative features of the real circulation. This violation, however, is at the core of why this quasi-geostrophic theory cannot predict the mean layer thicknesses $H/2$. We need to go to planetary-geostrophic scaling, as we will in the theory of the ventilated thermocline.

We now look for a steady circulation that satisfies these equations. Adding the two potential-vorticity conservation statements yields

$$\frac{f_0 w_{\mathrm{Ek}}}{H/2} = \mathrm{J}(\psi_1, q_1) + \mathrm{J}(\psi_2, q_2) \tag{2.51}$$

$$= \mathrm{J}(\psi_1 + \psi_2, \beta y) + \frac{2}{\lambda^2}\mathrm{J}(\psi_1, \psi_2 - \psi_1) - \frac{2}{\lambda^2}\mathrm{J}(\psi_2, \psi_2 - \psi_1) \tag{2.52}$$

$$= 2\,\mathrm{J}(\psi_{\mathrm{B}}, \beta y), \tag{2.53}$$

where we used the properties of the Jacobian operator that $J(A,A) = 0$ and $\mathrm{J}(A,B) = -\mathrm{J}(B,A)$. The barotropic streamfunction $\psi_{\mathrm{B}} = (\psi_1 + \psi_2)/2$, the streamfunction of the vertically averaged interior flow, can now be obtained directly from the forcing (Fig. 2.4):

$$\beta \frac{\partial \psi_{\mathrm{B}}}{\partial x} = \frac{f_0 w_{\mathrm{Ek}}}{H}, \quad \text{so} \quad \psi_{\mathrm{B}} = -\frac{f_0 w_0}{\beta H}(L - x)\sin\frac{\pi y}{L}, \tag{2.54}$$

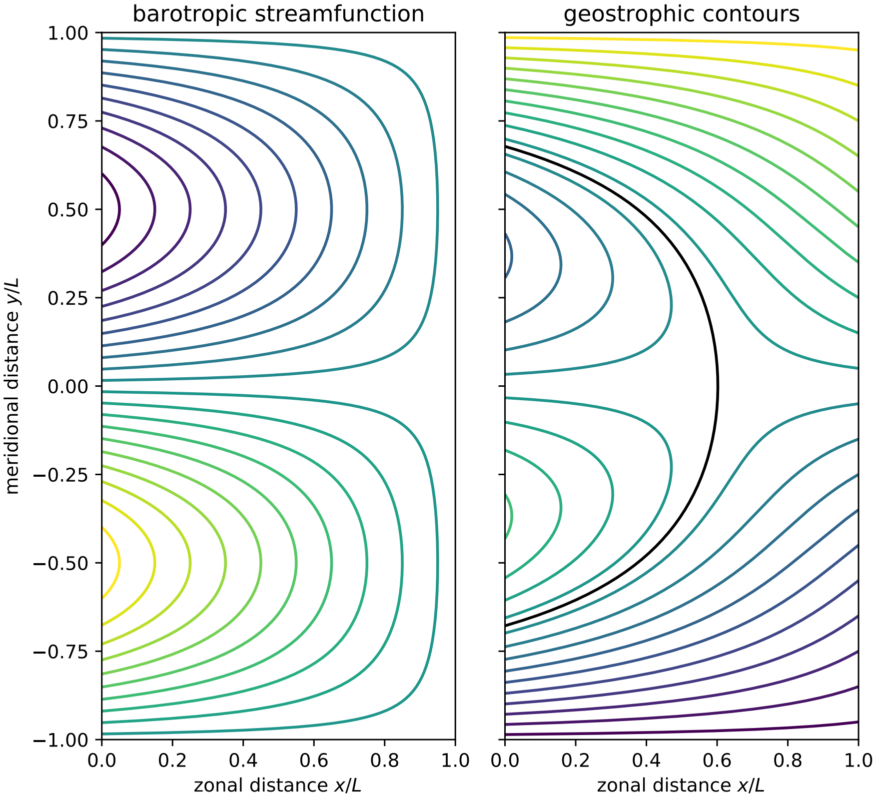

Figure 2.4: Barotropic streamfunction ψ_B (left) and geostrophic contours $\hat{q}_1$ in the lower layer (right). The black line on the right separates the shadow region, where there is no flow in the lower layer, from the pool region, where flow is induced. The solution is plotted for $f_0 w_0/(\lambda^2\beta^2 H) = 0.2$.

where we enforced that $\psi_\mathrm{B} = 0$ at the eastern boundary ($x = L$). This is Sverdrup's balance for the vertically integrated streamfunction $H\psi_\mathrm{B}$. Note that under quasi-geostrophic scaling, the interior transport is much larger than the Ekman transport because variations in the Coriolis parameter are assumed small. This eliminates the distinction between the vertically integrated interior transport and the total vertically integrated transport.

We now know the vertically averaged circulation, but we set out to determine the vertical structure of the circulation. So what is the circulation in the lower layer? From the potential-vorticity conservation in the lower layer, we find

$$0 = \mathrm{J}(\psi_1, q_1) = \mathrm{J}\left(\psi_1, \beta y + \frac{2}{\lambda^2}(\psi_2 - \psi_1)\right) = \mathrm{J}\left(\psi_1, \beta y + \frac{2}{\lambda^2}(\psi_1 + \psi_2)\right) = \mathrm{J}(\psi_1, \hat{q}_1) \tag{2.55}$$

if we define

$$\hat{q}_1 = \beta y + \frac{4}{\lambda^2}\psi_\mathrm{B}. \tag{2.56}$$

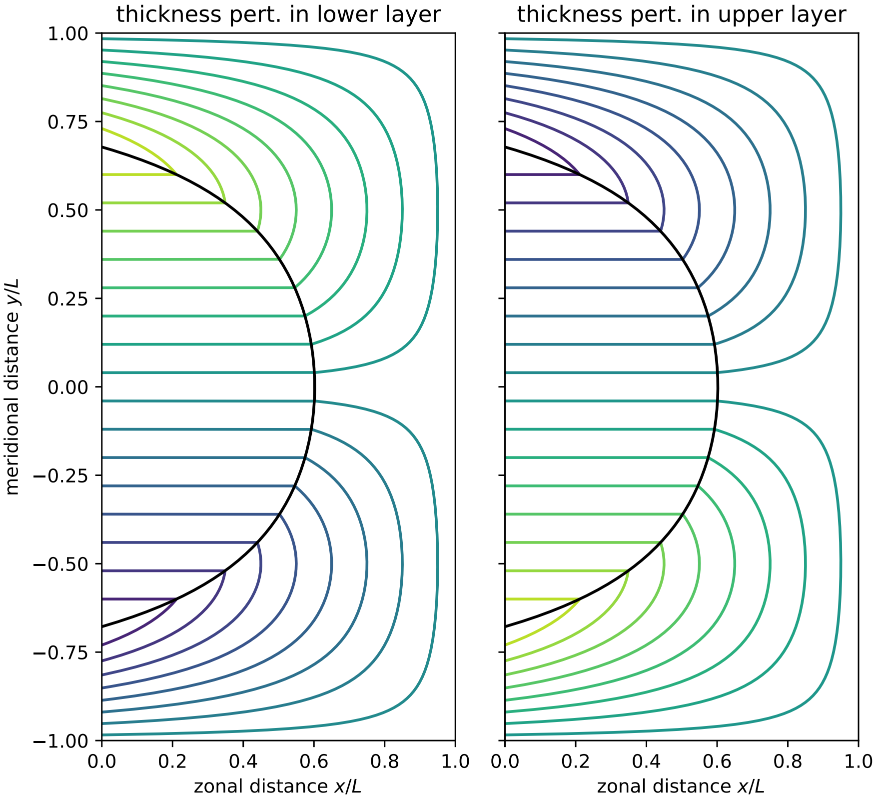

Figure 2.5: Layer thickness perturbations for the two layers. Yellowish colors are positive perturbations, purple colors are negative perturbations. The solution is plotted for $f_0 w_0/(\lambda^2 \beta^2 H) = 0.2$.

This means that the flow in the lower layer must be along lines of constant $\hat{q}_1$. The field $\hat{q}_1$, which is a known function of the forcing, thus defines geostrophic contours for the lower-layer flow. Two types of geostrophic contours emerge: those that connect the western and eastern boundaries of the basin and those that only touch the western boundary (Fig. 2.4).

In the part of the basin covered by geostrophic contours that touch the eastern boundary, we can immediately determine the flow. On the eastern boundary, we must satisfy the boundary condition $\psi_1 = 0$. Since (2.55) tells us that ψ_1 must be constant along geostrophic contours, $\psi_1 = 0$ must hold throughout this region. There is no flow in this region, which is why it is called the “shadow region.” The entire transport must be carried by the upper layer, so $\psi_2 = 2\psi_\mathrm{B}$ in this region.

While the lower layer does not move in the shadow region, its thickness does change (Fig. 2.5). The perturbations to the lower-layer thickness are proportional to $\psi_1 - \psi_2 = -\psi_2$, and those to the upper-layer thickness are proportional to ψ_2. The upper layer therefore thickens in the subtropics and thins in the subpolar region as we move westward, which is consistent with observations. The lower layer does the opposite.

The region covered by geostrophic contours that only touch the western boundary behaves very differently. While omitted from our explicit calculations, there are western boundary currents that close the circulation there. Accounting for these western boundary currents means that the geostrophic contours close on themselves in this region. We will refer to this region as the "pool region," and we require an additional piece of information to determine the flow there.

As the required additional principle, we posit that the lower-layer potential vorticity is homogenized in the pool region. This principle cannot be justified rigorously, but we provide a heuristic theoretical argument, evidence from numerical simulations, and some support from observations. All back the conclusion that homogenized potential vorticity in the pool region is a reasonable assumption.

The pool region is a region of recirculation: geostrophic contours are closed, and the gyre-scale circulation is directed along those contours. As there are no sources of potential vorticity in the lower layer, the only process affecting potential vorticity is then its transport by transient motion, such as Rossby waves and mesoscale eddies. Since potential vorticity is materially conserved, the stirring of a potential-vorticity field by transients tends generate potential-vorticty fluxes down any mean gradients. This stirring thus acts like diffusion and tends to eliminate such mean gradients. In the absence of any forcing that would maintain such gradients, it thus seems plausible to posit that transients erode gradients until the potential-vorticity field is homogenized, even if this homogenization is slow. Numerical simulations of the two-layer system, which retain the relative vorticity term and are forced as described above, do develop transients that homogenize the potential vorticity in the lower layer within the pool region. Plots showing homogenized potential-vorticity fields can be found, for example, in Rhines and Young (1982b) and Marshall et al. (1988). Finally, observations support the notion that there are regions in the western part of the ocean basins in which potential vorticity is homogenized, although the evidence is not entirely conclusive (Talley, 1988).

We complete the solution with the assumption that the lower-layer potential vorticity is homogenized in the pool region (Fig. 2.7). To match the value at the edge of the pool region, we set

$$q_1 = 0. \tag{2.57}$$

This allows us to determine the full flow:

$$q_1 = \beta y + \frac{2}{\lambda^2}(\psi_2 - \psi_1) = 0, \qquad \psi_\mathrm{B} = \frac{1}{2}(\psi_1 + \psi_2), \tag{2.58}$$

so

$$\psi_1 = \psi_\mathrm{B} + \frac{\lambda^2 \beta y}{4}, \qquad \psi_2 = \psi_\mathrm{B} - \frac{\lambda^2 \beta y}{4}. \tag{2.59}$$

In the pool region, the vertically integrated transport is split between the two layers (Fig. 2.6). Even though the wind forcing does not directly act on the lower layer, flow is induced there through the action of transients.

Overall, this simplest form of a quasi-geostrophic theory of wind-driven gyres suggests that while the stratification largely confines the circulation to the upper layer, the

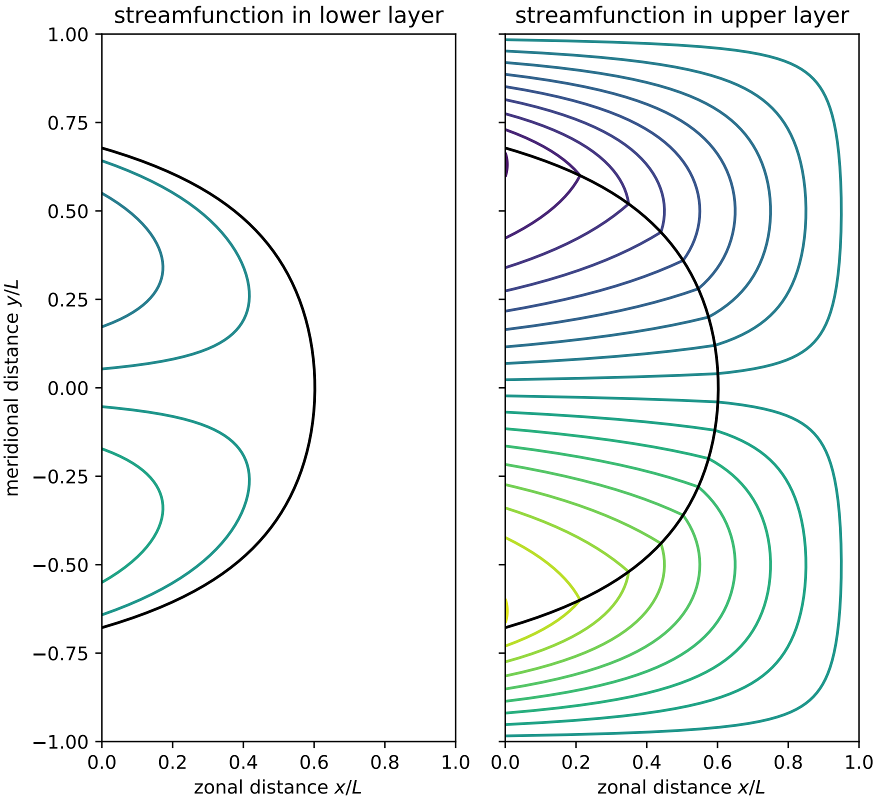

Figure 2.6: Streamfunctions of the flow in the two layers. In both layers, the flow is anticyclonic in the subtropics and cyclonic in the subpolar region. Note the alignment of the lower-layer flow with the geostrophic contours defined by $\hat{q}_1$ (Fig. 2.4). The solution is plotted for $f_0 w_0/(\lambda^2\beta^2 H) = 0.2$.

flow extends ever deeper the farther west one moves and the stronger the forcing is (which would enlarge the pool region). One can generalize this theory to more layers (see homework) and even to the continuous limit. This generalization confirms the tendency we observed in the two-layer version of the theory: that the subtropical circulation is confined to a bowl that deepens westward and toward the zero curl line. In the subpolar region, the thermocline bulges up.

2.4 The ventilated thermocline

Having elucidated how the stratification affects the gyre circulation, we now ask the more fundamental question: how does that stratification arise in the first place? Instead of making the quasi-geostrophic approximation, in which mean layer thicknesses must be prescribed *a priori*, we now consider planetary-geostrophic dynamics. The flow is now is strict geostrophic balance, and layer thicknesses can vary without bound. In

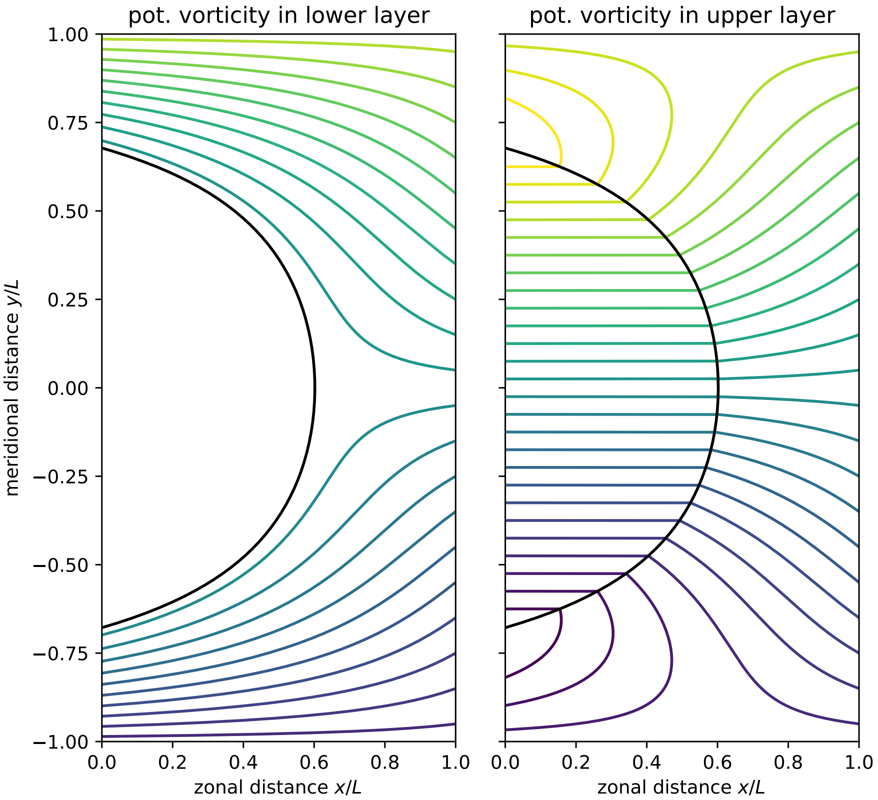

Figure 2.7: Potential vorticity in the two layers. In the unforced lower layer, potential vorticity is homogenized in the pool region (by assumption). The solution is plotted for $f_0 w_0/(\lambda^2\beta^2 H) = 0.2$.

fact, we will consider the case in which layer interfaces outcrop, i.e., they come all the way up to the sea surface. The theory described in the following was developed by Luyten et al. (1983).

We consider an ocean consisting of three layers: a deep layer 1 that we assume at rest, and intermediate layer 2, and a top layer 3. The interface between the intermediate layer and the top layer outcrops at $y = y_2$. We assume that the outcrop position is independent of longitude, and that the outcrop latitude is set by the atmospheric forcing. We can think of this as an imposed meridional surface temperature gradient, corresponding to the step from a higher buoyancy in the top layer to a lower buoyancy in the intermediate layer that occurs at the outcrop latitude. The deep layer does not outcrop and can be thought of as the result of deep water formation in remote high latitudes. The circulation of the deep ocean is sluggish compared to that of the thermocline, so assuming the deep layer to be at rest is not a bad assumption. To simplify the algebra, we assume that the differences between the layer buoyancies are the same: $b_3 - b_2 = b_2 - b_1 = g'$.

The system is forced by Ekman pumping entering whichever layer touches the surface. We impose the Ekman pumping velocity

$$w_{\mathrm{Ek}} = -w_0 \sin \frac{\pi y}{L}, \tag{2.60}$$

which corresponds to the wind stress

$$\tau^x = -\frac{\rho_0 f w_0 L}{\pi} \cos \frac{\pi y}{L}. \tag{2.61}$$

We consider the subtropics only, so our ocean extends from $x = 0$ to $x = L$ and $y = 0$ to $y = L$.

We first consider the dynamics north of the outcrop latitude y_1. There are only two layers present: the resting deep layer 1 and the moving intermediate layer 2. We determine the circulation and the thickness h_2 of layer 2 based on two principles: Sverdrup balance and thermal wind.

In layer 2, the planetary-geostrophic momentum equations are

$$-f v_2 = -\frac{1}{\rho_0} \frac{\partial p_2}{\partial x}, \qquad f u_2 = -\frac{1}{\rho_0} \frac{\partial p_2}{\partial y}. \tag{2.62}$$

Cross-differentiating these gives us the linear vorticity equation

$$\beta v_2 = f \frac{\partial w}{\partial z}, \tag{2.63}$$

which upon integration over the layer yields

$$\beta h_2 v_2 = f w_{\mathrm{Ek}}. \tag{2.64}$$

We used here that the horizontal flow within the layer is independent of depth and that the deep layer is at rest, which implies that the vertical velocity just below the interface between the intermediate and deep layer vanishes.

To derive the thermal-wind balance for a layered system, consider a general interface between layers i and $i+1$, located at $z = z_i$. The pressure field must be continuous across this interface, so we require

$$p_i + \rho_0 b_i z_i = p_{i+1} + \rho_0 b_{i+1} z_i. \tag{2.65}$$

Differentiating this equation with respect to x and applying geostrophic balance in both layers yields

$$f(v_{i+1} - v_i) = -(b_{i+1} - b_i) \frac{\partial z_i}{\partial x}. \tag{2.66}$$

This tells us that the jump in the meridional velocity across the interface is proportional to the zonal slope of the interface. Differentiating with respect to y tells us similarly that

$$f(u_{i+1} - u_i) = (b_{i+1} - b_i) \frac{\partial z_i}{\partial y}. \tag{2.67}$$

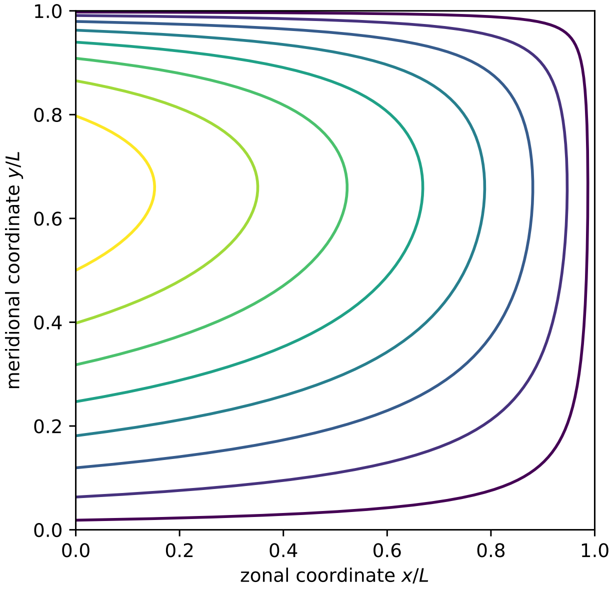

Figure 2.8: The function $D(x, y)$ defined in (2.71). The function is normalized by h_{E} and plotted for $f = f_0 + \beta(y - L/2)$, $f_0^2 w_0 L/\beta g' h_{\mathrm{E}}^2 = 2$, and $\beta L/f_0 = 1$.

These are the layer versions of thermal-wind balance, also known as “Margules’s equations.”

Applying the thermal-wind relation (2.66) to the interface between the moving layer 2 and the resting deep layer 1 yields

$$f v_2 = -(b_2 - b_1)\frac{\partial z_1}{\partial x} = g'\frac{\partial h_2}{\partial x}, \tag{2.68}$$

where we used the $z_1 = -h_2$. Combining this equation with the Sverdrup balance (2.64), we obtain

$$f^2 w_{\mathrm{Ek}} = \beta g' \frac{\partial}{\partial x}\left(\frac{h_2^2}{2}\right). \tag{2.69}$$

We can integrate this starting from the eastern boundary:

$$h_2^2 - h_{\mathrm{E}}^2 = \frac{2f^2}{\beta g'}\int_L^x w_{\mathrm{Ek}}\,\mathrm{d}x' = D^2 \tag{2.70}$$

where h_{E} is the thickness of layer 2 on the eastern boundary, and

$$D^2 = \frac{2f^2}{\beta g'}\int_L^x w_{\mathrm{Ek}}\,\mathrm{d}x' = \frac{2f^2}{\beta g'}(L - x)w_0 \sin\frac{\pi y}{L} \tag{2.71}$$

is a known function of the forcing (Fig. 2.8). As long as we have Ekman pumping, i.e., $w_{\mathrm{Ek}} < 0$, it is ensured that $D^2 > 0$ everywhere. The thickness of layer 2 is thus

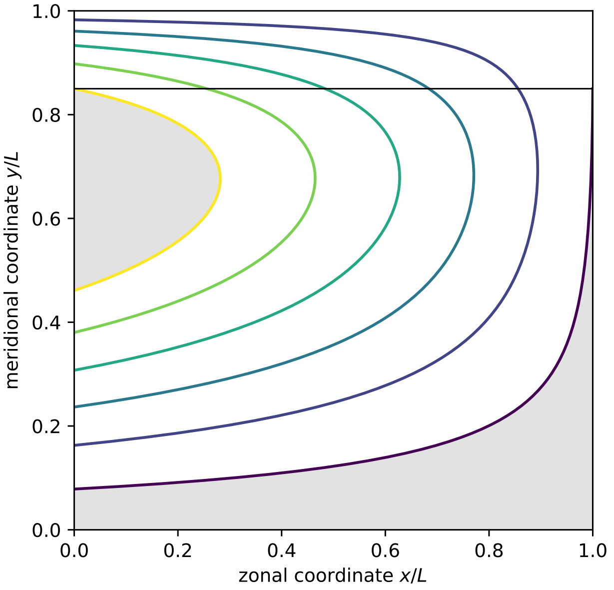

Figure 2.9: Combined thickness of the active layers as determined by the theory of the ventilated thermocline. North of the outcrop line at $y = y_2$, only layer 2 exists, so h_2 is plotted there. South of the outcrop line, both layers 2 and 3 exist, so $h = h_2 + h_3$ is plotted there. The solution is plotted for $f = f_0 + \beta(y - L/2)$, $f_0^2 w_0 L/\beta g' h_{\mathrm{E}}^2 = 2$, $\beta L/f_0 = 1$, and $y_2/L = 0.85$.

determined to be

$$h_2 = \sqrt{h_{\mathrm{E}}^2 + D^2}. \tag{2.72}$$

We have used the positive root because a negative layer thickness is unphysical. Since D^2 increases westward, layer 2 thickens as we move westward (Fig. 2.9). This westward thickening of the thermocline is in qualitative agreement with the quasi-geostrophic theory discussed above and with observations.

The solution (2.72) determines the thickness of layer 2 throughout the region north of the outcrop latitude, although we do need to prescribe its thickness on the eastern boundary. If the eastern boundary is considered to be a vertical sidewall, h_{E} must be a constant because otherwise thermal wind would require a flow across that sidewall. But this constant is arbitrary and cannot be determined as part of the solution. This constitutes a bit of an Achilles heel of the theory.

We now turn to the dynamics south of the outcrop line. Our solution in this region still employs Sverdrup balance and thermal wind, but we need an additional dynamical principle because we have to determine the flow and thickness in two active layers: layer 3, which is in contact with the atmosphere, and layer 2, which is now shielded from the atmosphere by layer 3. Fluid columns in layer 2 that move across the outcrop line—note that the zonal slope of the layer interface north of the outcrop implies a southward flow—are said to be "subducted," in analogy to tectonic plates. Once moved across the outcrop line, fluid columns in layer 2 do not experience any atmospheric forcing anymore, and therefore conserve their potential vorticity. This is the third dynamical principle that we take advantage of to derive a solution.

We begin with the thermal-wind balance between the deep layer 1, which is at rest, and the intermediate layer 2:

$$f v_2 = -g' \frac{\partial z_1}{\partial x} = g' \frac{\partial h}{\partial x}, \qquad f u_2 = g' \frac{\partial z_1}{\partial y} = -g' \frac{\partial h}{\partial y}, \tag{2.73}$$

where $h = h_2 + h_3 = -z_1$ is the combined thickness of the two active layers. This tells us that the flow in layer 2 is always directed along contours of constant h, so h defines streamlines for the flow of layer 2. Because the potential vorticity in layer 2 is conserved, this further tells us that this layer's potential vorticity $q_2 = f/h_2$ along h contours. The potential-vorticity conservation holds south of the outcrop line, such that the potential vorticity is set at the outcrop line and carried into the subducted layer:

$$q_2 = \frac{f}{h_2} = \frac{f_2}{h}, \tag{2.74}$$

where $f_2 = f(y_2)$ is the Coriolis parameter at the outcrop latitude $y = y_2$. This relation allows us to express the thicknesses of the two active layers relative to h:

$$h_2 = \frac{f}{f_2} h, \quad \text{and} \quad h_3 = h - h_2 = \left(1 - \frac{f}{f_2}\right) h. \tag{2.75}$$

All that is left to do is to determine h from Sverdrup balance and thermal wind, similar to what we did for the region north of the outcrop.

South of the outcrop, where the meridional transport is split between the two active layers, Sverdrup balance reads

$$\beta \left(h_2 v_2 + h_3 v_3\right) = f w_{\mathrm{Ek}}. \tag{2.76}$$

The thermal-wind balance between the active layers is

$$f\left(v_3 - v_2\right) = -g' \frac{\partial z_2}{\partial x} = g' \frac{\partial h_3}{\partial x}. \tag{2.77}$$

We combine this relation with (2.73), the thermal-wind balance between layer 1 and 2, to obtain

$$f v_3 = g' \frac{\partial}{\partial x}\left(h + h_3\right). \tag{2.78}$$

Substituted back into Sverdrup balance (2.76), we obtain

$$\beta g' \left[(h - h_3) \frac{\partial h}{\partial x} + h_3 \frac{\partial}{\partial x}\left(h + h_3\right) \right] = f^2 w_{\mathrm{Ek}}. \tag{2.79}$$

The two terms involving $h_3 \partial h / \partial x$ cancel, such that

$$\frac{\beta g'}{2} \frac{\partial}{\partial x}\left(h^2 + h_3^2\right) = f^2 w_{\mathrm{Ek}}. \tag{2.80}$$

which we can integrate zonally starting on the eastern boundary to obtain

$$h^2 + h_3^2 - h_{\mathrm{E}}^2 = D^2. \tag{2.81}$$

We used that $h = h_{\mathrm{E}}$ on the eastern boundary, because we are still required to prevent flow across the boundary, and we assumed that the thickness of layer 3 vanishes on the eastern boundary: $h_3 = 0$ at $x = L$. This is the only sensible choice because $h_3 = 0$ at the outcrop latitude, and thermal wind requires a constant layer thickness along the eastern sidewall. Combined with the potential-vorticity conservation along the paths of fluid columns in layer 2, i.e., with the expression for h_3 in (2.75), we obtain

$$h = \sqrt{\frac{h_{\mathrm{E}}^2 + D^2}{1 + \left(1 - \frac{f}{f_2}\right)^2}}. \tag{2.82}$$

From this equation, the thicknesses of the two layers follows through (2.75), and the flow follows from thermal wind.

This solution, however, does not apply everywhere south of the outcrop line. We employed the conservation of potential vorticity in layer 2 and traced fluid columns back to the outcrop line to determine their potential vorticity at the point of subduction. This only works in locations that receive such subducted fluid columns, i.e., in locations struck by h contours emanating from the outcrop line. A look at the solution (2.82) reveals two regions that are not struck by such contours: a pool region in the west and a shadow region in the east (Fig. 2.9).

The h contour emanating from $(x, y) = (L, y_2)$ turns west, opening up a region between this contour and the eastern and southern boundaries that is not struck by fluid columns subducted at the outcrop line. This region is not ventilated and in the "shadow" of the eastern boundary. There is no flow in layer 2, and the Sverdrup transport is carried entirely by layer 3. The lack of flow in layer 2 requires a constant thickness $h = h_{\mathrm{E}}$, such that (2.81) yields

$$h_3 = D. \tag{2.83}$$

In the real ocean, these shadow regions are characterized by extremely low oxygen concentrations, the result of microbial drawdown and a lack of resupply by ventilation.

We leave the pool region to the homework, where we will determine a solution based on the assumption that potential vorticity is homogenized in layer 2. We also note that our solution has ignored western boundary currents, which must be present to close the circulation on the western margin of the basin. But with these elements added, we arrive at a fairly comprehensive theory of the structure of thermocline. The main feature distinguishing it from the quasi-geostrophic theory considered above is the ventilation of the region south of the outcrop line. The surface outcrop of the intermediate water allows for motion once the layer is subducted and shielded from the atmospheric forcing, without the action of transients. The dynamics of this region are thus fundamentally distinct from that of the pool region.

The theory of the ventilated thermocline offers a relatively simple model of the bowl-shaped stratification structure of subtropical gyres, the ventilation of the thermocline through subduction, and the stagnant shadow regions near eastern boundaries. This theory can be generalized to more layers or more complicated geometries, which facilitates the comparison to observations but reveals no new physics.

Chapter 3

The Southern Ocean

Thus far, we have been concerned exclusively with the circulation in ocean basins. The continental margins at the eastern and western edges of these basins have played a key role in the theories we have developed for the wind-driven gyre circulation. In particular, the presence of a western boundary allows for a swift boundary current that returns the meridional transport required by Sverdrup balance in the basin interior.

The Southern Ocean has drastically different dynamics than these ocean basins, largely because it is (at least partially) zonally unblocked. This allows for a circumpolar current, the Antarctic Circumpolar Current (ACC). The transport of the ACC at Drake Passage is about 130 Sv, which makes it the strongest current on Earth. The ACC consists of two major temperature fronts: the Subantarctic Front and the Subpolar Front, across both of which the temperature drops sharply by a few Kelvin. By thermal-wind balance, these fronts are associated with swift currents.

The ACC is bounded to the north by a subtropical gyre circulation, which merges into a "supergyre" south of the southern tip of Africa. To the south, the ACC is bounded by the Weddell and Ross Gyres, where the Antarctic Peninsula and the Victoria Land provide western boundaries, as well as by the Antarctic Margin where no such gyres exist.

The ACC has to navigate some prominent topography. Most importantly, it flows through the narrow meridional constriction at Drake Passage. In Drake Passage, the ACC is forced across the Scotia Arc, with bathymetry rising to about 2000 m depth. Other major topographic features that at least partially steer the ACC are the Kerguelen Plateau, Macquarie Ridge, and the East Pacific Rise.

3.1 The need for eddies

The Southern Ocean is forced by the strongest winds on Earth: the "roaring fourties" apply a strong westerly stress at the ocean surface. This drives northward Ekman transport

$$V^{\mathrm{E}} = -\frac{\tau^x}{\rho_0 f}. \tag{3.1}$$

In gyres, this transport would be attended by an interior geostrophic transport

$$V^{\mathrm{I}} = \frac{1}{\rho_0 \beta} \boldsymbol{z} \cdot (\nabla \times \boldsymbol{\tau}) + \frac{\tau^x}{\rho_0 f}, \tag{3.2}$$

carried by the thermocline, such that the vertically integrated transport is in Sverdrup balance

$$\beta V = \frac{1}{\rho_0} \boldsymbol{z} \cdot (\nabla \times \boldsymbol{\tau}). \tag{3.3}$$

The resulting net meridional transport is returned by a western boundary current that is typically topographically steered. Put another way: in ocean basins, the wind-driven Ekman transport is returned by a geostrophic transport that consist of a component in the interior of the basin and a western boundary current. This net meridional geostrophic transport is possible because a pressure gradient can be sustained between the two boundaries. Zonally integrating the zonal geostrophic momentum balance gives

$$f \int_{x_{\mathrm{W}}}^{x_{\mathrm{E}}} v^{\mathrm{I}} \, \mathrm{d}x = \frac{1}{\rho_0} (p_{\mathrm{E}} - p_{\mathrm{W}}). \tag{3.4}$$

This is impossible in the Southern Ocean because the start and end points of the zonal integration are identical. We are thus forced to conclude that the zonally integrated geostrophic transport vanishes:

$$\int v^{\mathrm{I}} \, \mathrm{d}x = 0. \tag{3.5}$$

This applies at all latitudes and depths at which the flow is zonally unblocked. The ocean must find a different way to return the Ekman transport.

Two possibilities suggest themselves: either there is an ageostrophic return flow, or the Ekman transport is returned below the depth of the Scotia Arc sill, where zonal boundaries can again support a pressure gradient. The first possibility can be realized in a bottom Ekman layer, where geostrophic balance can be broken. This does occur in numerical simulations of an idealized circumpolar channel with a flat bottom. But in the real ocean, this plays a minor role: the return flow is thought to occur largely along topographic features such as the sill in Drake Passage.

This return of the Ekman transport at depth—the Scotia Arc only reaches about 2000 m—has major consequences for the circulation of the Southern Ocean. It implies that the Ekman pumping on the northern flank of the ACC and the Ekman suction on the southern flank of the ACC reach to much greater depths than the Ekman pumping in the thermocline of gyres. The Ekman pumping and suction in the Southern Ocean thus pushes down isopycnals to the north and pulls up isopycnals to the south, tending to steepen the isopycnals across a layer 2000 m thick.

This steepening of isopycnals by the Ekman circulation indeed leads to isopycnals that slope much more strongly in the Southern Ocean than they do elsewhere, especially below the thermocline. But if the Ekman circulation were unopposed, it would eventually render isopycnals vertical in the Southern Ocean. This is unrealistic and was in fact a severe problem of climate models up until the 1990s. So what is missing from this picture?

What is missing is that the circumpolar current associated with the sloping isopycnals, is baroclinically unstable. Mesoscale eddies release some of the potential energy associated with the sloping isopycnals and thus tend to flatten these isopycnals. The observed isopycnal slopes are then the result of a balance between the Ekman circulation that tends to steepen isopycnals and mesoscale eddies that tend to flatten isopycnals. Mesoscale eddies therefore play a leading-order role in the Southern Ocean. Without them, the hydrography would be qualitatively different, like in coarse-resolution climate models that do not take the flattening by the eddies into account. Once eddies are resolve or parameterized in these models, the simulated isopycnal slopes become realistic.

To understand how eddies can flatten isopycnals, consider the quasi-geostrophic buoyancy budget:

$$\frac{\partial b_0}{\partial t} + u_0 \frac{\partial b_0}{\partial x} + v_0 \frac{\partial b_0}{\partial y} + w_1 N^2 = 0. \tag{3.6}$$

We can use the horizontal nondivergence of the leading order flow,

$$\frac{\partial u_0}{\partial x} + \frac{\partial v_0}{\partial y} = 0 \tag{3.7}$$

to rewrite the buoyancy budget as

$$\frac{\partial b_0}{\partial t} + \frac{\partial}{\partial x}(u_0 b_0) + \frac{\partial}{\partial y}(v_0 b_0) + w_1 N^2 = 0. \tag{3.8}$$

We now average this buoyancy budget zonally over the circumpolar channel, denoting the zonal average with angle brackets:

$$\frac{\partial \langle b_0 \rangle}{\partial t} + \frac{\partial}{\partial y}\langle v_0 b_0 \rangle + \langle w_1 \rangle N^2 = 0. \tag{3.9}$$

The zonal transport term vanishes because the domain is zonally periodic. We further decompose the flow into a zonal mean and a perturbation from that zonal mean:

$$b_0 = \langle b_0 \rangle + b_0', \qquad v_0 = \langle v_0 \rangle + v_0'. \tag{3.10}$$

The meridional buoyancy flux can then be written as a sum between a mean flux and an eddy flux:

$$\langle v_0 b_0 \rangle = \left\langle \left(\langle v_0 \rangle + v_0' \right) \left(\langle b_0 \rangle + b_0' \right) \right\rangle = \langle v_0 \rangle \langle b_0 \rangle + \left\langle v_0' b_0' \right\rangle. \tag{3.11}$$

Given that the leading-order flow is in geostrophic balance and that the Southern Ocean is zonally unblocked, however, $\langle v_0 \rangle = 0$, and the mean buoyancy flux vanishes. We are left with the buoyancy budget

$$\frac{\partial \langle b_0 \rangle}{\partial t} + \frac{\partial}{\partial y}\left\langle v_0' b_0' \right\rangle + \langle w_1 \rangle N^2 = 0. \tag{3.12}$$

In order for the system to reach a steady state, the buoyancy tendencies due to the Ekman circulation $\langle w_1 \rangle N^2$ must be balanced by the divergence of meridional eddy fluxes. The eddies must transport buoyancy southward to balance the downwelling of buoyant water in the north and the upwelling of dense water in the south.

3.2 Eddy effects

The above discussion suggests that in the absence of zonal-mean meridional geostrophic flow in the part of the Southern Ocean that is zonally unblocked, the steepening of isopycnals by the wind-driven Ekman circulation must be opposed by eddies. These eddies, arising primarily from baroclinic instability of the ACC, tend to flatten isopycnals and must be taken into account to explain and model the observed hydrography. Without eddies, the Southern Ocean would look qualitatively different. We now take a closer look at how these eddies affect the mean flow and buoyancy distribution in a zonally reentrant channel like the Southern Ocean to begin to construct a quantitative description of eddy effects.

The machinery we are about to discuss was originally developed to understand the midlatitude atmospheric circulation. Like the Southern Ocean, the atmosphere is zonally reentrant and harbors baroclinic eddies that have a profound impact on the mean state.

Our goal is to understand the mean state of the Southern Ocean: how strongly do isopycnals slope and how strong is the zonal current? It is therefore sensible to decompose the flow into such zonal mean variables and perturbations from the zonal mean, which we will simply refer to as “eddies,” having in mind mesoscale eddies in particular. We therefore begin our discussion by taking the zonal average of the quasi-geostrophic equations of motion.

We begin with the zonal momentum equation

$$\frac{\partial u_0}{\partial t} + u_0 \frac{\partial u_0}{\partial x} + v_0 \frac{\partial u_0}{\partial y} - f_0 v_1 - \beta y v_0 = -\frac{1}{\rho_0} \frac{\partial p_1}{\partial x}, \tag{3.13}$$

which is the momentum equation at order ε, the Rossby number of the flow, which describes the deviations from the leading-order geostrophic balance. Since the leading-order flow is horizontally nondivergent, we can rewrite the advective terms as

$$\frac{\partial u_0}{\partial t} + \frac{\partial}{\partial x}(u_0 u_0) + \frac{\partial}{\partial y}(u_0 v_0) - f_0 v_1 - \beta y v_0 = -\frac{1}{\rho_0} \frac{\partial p_1}{\partial x}. \tag{3.14}$$

A zonal average then eliminates the zonal momentum flux term, and we are left with

$$\frac{\partial \langle u_0 \rangle}{\partial t} + \frac{\partial}{\partial y} \left\langle u_0' v_0' \right\rangle - f_0 \langle v_1 \rangle = 0. \tag{3.15}$$

The meridional momentum flux is equal to the eddy flux because there is no leading-order zonal-mean meridional flow: $\langle v_0 \rangle = 0$. (This also eliminates the β-term.) This equation for the zonal-mean zonal flow tells us that this flow can change in response to the divergence of a meridional eddy momentum flux and in response to an ageostrophic meridional circulation. The zonal-mean buoyancy budget is, as before,

$$\frac{\partial \langle b_0 \rangle}{\partial t} + \frac{\partial}{\partial y} \left\langle v_0' b_0' \right\rangle + \langle w_1 \rangle N^2 = 0. \tag{3.16}$$

The zonal-mean buoyancy field can therefore change in response to the divergence of a meridional eddy buoyancy flux and in response to an ageostrophic vertical circulation. The ageostrophic circulation $\langle v_1 \rangle$ and $\langle w_1 \rangle$ has to satisfy the continuity equation

$$\frac{\partial \langle v_1 \rangle}{\partial y} + \frac{\partial \langle w_1 \rangle}{\partial z} = 0, \tag{3.17}$$

and zonally averaging the combination of hydrostatic and geostrophic balance yield the thermal-wind balance of the zonal-mean zonal flow:

$$f_0 \frac{\partial \langle u_0 \rangle}{\partial z} = -\frac{\partial \langle b_0 \rangle}{\partial y}. \tag{3.18}$$

These zonally averaged "Eulerian-mean" equations appear to reveal the effects of eddies in a straightforward way: momentum fluxes enter the zonal-mean momentum budget and buoyancy fluxes enter the zonal-mean buoyancy budget. It turns out, however, that the response of the mean circulation to eddies is far from straightforward. Consider, for example, eddies that generate a buoyancy flux $\left\langle v_0' b_0' \right\rangle < 0$ and no momentum flux $\left\langle u_0' v_0' \right\rangle = 0$, similar to what might be considered the leading-order effect of eddies in the Southern Ocean. The buoyancy budget would lead us to conclude that the mean buoyancy field responds to the eddies: where the buoyancy flux is divergent, there is a negative buoyancy tendency, and where the buoyancy flux is convergent, there is a positive buoyancy tendency. The buoyancy field cannot change in isolation, however, because thermal-wind balance must be maintained. The reduction in a meridional buoyancy gradient must be attended by a reduction in the vertical shear of the zonal flow, which is accomplished through the establishment of an ageostrophic circulation in the meridional–vertical plane. We are forced to admit that the zonal-mean buoyancy and momentum budgets are tightly coupled and that the effects of eddies remain opaque in these Eulerian-mean equations.

The effects of eddies becomes much more apparent when we transform the equations with what at first might seem like a mathematical trick but in fact has deep physical meaning. We subsume the eddy buoyancy flux into a redefined mean circulation to remove the effect of the eddies from the buoyancy budget:

$$\langle w_1 \rangle^* = \langle w_1 \rangle + \frac{\partial}{\partial y} \left(\frac{\left\langle v_0' b_0' \right\rangle}{N^2} \right), \tag{3.19}$$

such that

$$\frac{\partial \langle b_0 \rangle}{\partial t} + \langle w_1 \rangle^* N^2 = 0. \tag{3.20}$$

To impose that the redefined circulation is nondivergent in the meridional–vertical plane, i.e., that

$$\frac{\partial \langle v_1\rangle^*}{\partial y} + \frac{\partial \langle w_1\rangle^*}{\partial z} = 0, \tag{3.21}$$

we also define

$$\langle v_1\rangle^* = \langle v_1\rangle - \frac{\partial}{\partial z}\left(\frac{\left\langle v_0' b_0'\right\rangle}{N^2}\right). \tag{3.22}$$

This redefined meridional circulation is called the "residual circulation" because it is the residual between the Eulerian mean circulation and an eddy component. Defining streamfunctions for these circulations,

$$\langle v_1\rangle = -\frac{\partial \chi}{\partial z} \quad \text{and} \quad \langle w_1\rangle = \frac{\partial \chi}{\partial y} \tag{3.23}$$

for the Eulerian-mean circulation and

$$\langle v_1\rangle^* = -\frac{\partial \chi^*}{\partial z} \quad \text{and} \quad \langle w_1\rangle^* = \frac{\partial \chi^*}{\partial y} \tag{3.24}$$

for the residual circulation, we find

$$\chi^* = \chi + \frac{\left\langle v_0' b_0'\right\rangle}{N^2}. \tag{3.25}$$

We can think of the eddy term here as inducing a meridional overturning circulation, which when added to the Eulerian-mean circulation χ gives us the residual-mean circulation χ^*.

Our redefinition of the mean circulation did not remove the eddy terms, of course, but rather shifted them over to the momentum budget. Writing that budget in terms of the residual-mean circulation, we find

$$\frac{\partial \langle u_0\rangle}{\partial t} - f_0\langle v_1\rangle^* = -\frac{\partial}{\partial y}\left\langle u_0' v_0'\right\rangle + f_0\frac{\partial}{\partial z}\left(\frac{\left\langle v_0' b_0'\right\rangle}{N^2}\right) = -\nabla\cdot\boldsymbol{F}, \tag{3.26}$$

where $\boldsymbol{F}$, the "Eliassen–Palm flux," is defined as

$$\boldsymbol{F} = \left\langle u_0' v_0'\right\rangle \boldsymbol{y} - f_0\frac{\left\langle v_0' b_0'\right\rangle}{N^2}\boldsymbol{z}. \tag{3.27}$$

The eddy effects are now compactly represented as the divergence of the Eliassen–Palm flux, which acts like a flux of zonal-mean momentum. But why should the meridional eddy buoyancy flux appear as a vertical flux of momentum? It turns out that this buoyancy flux is closely related to the vertical momentum flux between density layers through what is called "form stress." A meridional buoyancy flux $\left\langle v_0' b_0'\right\rangle < 0$ generates pressure perturbations that transfer momentum from upper to lower layers, consistent with a downward Eliassen–Palm flux (note that $f_0 < 0$) in the Southern Ocean. There is thus an equivalence, at least for geostrophic flow, between meridional momentum fluxes and form stress, reassuring us that the appearance of the buoyancy flux in the Eliassen–Palm vector is less strange than it might seem at first sight. This equivalence also hints at the connection to averages in isopycnal layers or more generally in isopycnal coordinates ("thickness-weighted averages"). In fact, the residual circulation is closely related to the thickness-weighted mean circulation—a full discussion of which, however, would take us way beyond what we can do in this course (Young, 2012). It suffices to say that the buoyancy budget (3.20) hints at the fact that it is the residual circulation that advects conserved tracers, not the Eulerian mean circulation.

A further conceptual advantage of the TEM framework is that the convergence of the Eliassen–Palm flux can be expressed as a potential-vorticity flux. To see this, we first express the convergence of the meridional component of the Eliassen–Palm flux as the meridional flux of relative vorticity:

$$\begin{aligned}-\frac{\partial}{\partial y}\left\langle u_0'v_0'\right\rangle &= -\left\langle \frac{\partial u_0'}{\partial y}v_0'\right\rangle - \left\langle u_0'\frac{\partial v_0'}{\partial y}\right\rangle \\ &= -\left\langle v_0'\frac{\partial u_0'}{\partial y}\right\rangle + \left\langle u_0'\frac{\partial u_0'}{\partial x}\right\rangle = \left\langle v_0'\left(\frac{\partial v_0'}{\partial x} - \frac{\partial u_0'}{\partial y}\right)\right\rangle, \end{aligned} \tag{3.28}$$

where we used that

$$\left\langle u_0'\frac{\partial u_0'}{\partial x}\right\rangle = \left\langle \frac{\partial}{\partial x}\left(\frac{u_0'^2}{2}\right)\right\rangle = 0 \tag{3.29}$$

and likewise for v_0'. We then express the convergence of the vertical component of the Eliassen–Palm flux as the meridional flux of the stretching contribution to potential vorticity:

$$\begin{aligned} f_0\frac{\partial}{\partial z}\left(\frac{\left\langle v_0'b_0'\right\rangle}{N^2}\right) &= f_0\left\langle \frac{\partial v_0'}{\partial z}\frac{b_0'}{N^2}\right\rangle + f_0\left\langle v_0'\frac{\partial}{\partial z}\left(\frac{b_0'}{N^2}\right)\right\rangle \\ &= \left\langle \frac{\partial b_0'}{\partial x}\frac{b_0'}{N^2}\right\rangle + f_0\left\langle v_0'\frac{\partial}{\partial z}\left(\frac{b_0'}{N^2}\right)\right\rangle = f_0\left\langle v_0'\frac{\partial}{\partial z}\left(\frac{b_0'}{N^2}\right)\right\rangle, \end{aligned} \tag{3.30}$$

where we used thermal-wind balance and the analogue to (3.29) for b_0'. We therefore have

$$-\nabla\cdot\boldsymbol{F} = \left\langle v_0'q'\right\rangle \quad \text{with} \quad q' = \frac{\partial v_0'}{\partial x} - \frac{\partial u_0'}{\partial y} + f_0\frac{\partial}{\partial z}\left(\frac{b_0'}{N^2}\right). \tag{3.31}$$

Collecting our TEM equations, we have arrived at

$$\frac{\partial \langle u_0 \rangle}{\partial t} - f_0 \langle v_1 \rangle^* = \left\langle v_0' q' \right\rangle, \tag{3.32}$$

$$f_0 \frac{\partial \langle u_0 \rangle}{\partial z} = -\frac{\partial \langle b_0 \rangle}{\partial y}, \tag{3.33}$$

$$\frac{\partial \langle v_1 \rangle^*}{\partial y} + \frac{\partial \langle w_1 \rangle^*}{\partial z} = 0, \tag{3.34}$$

$$\frac{\partial \langle b_0 \rangle}{\partial t} + \langle w_1 \rangle^* N^2 = 0. \tag{3.35}$$

These equations form a closed set of equations for the variables $\langle u_0 \rangle$, $\langle b_0 \rangle$, $\langle v_1 \rangle^*$, and $\langle w_1 \rangle^*$ if the eddy effects, compactly represented by their meridional potential-vorticity flux, are known. In reality, the eddies depend on the mean state, potentially in a complicated way—this is the parameterization problem we discuss below.

The TEM equations (3.32) to (3.35) can be combined to form the diagnostic equation

$$N^2 \frac{\partial^2 \chi^*}{\partial y^2} + f_0^2 \frac{\partial^2 \chi^*}{\partial z^2} = f_0 \frac{\partial}{\partial z} \left\langle v_0' q' \right\rangle. \tag{3.36}$$

This allows us to determine the residual circulation described by χ^* from the vertical change in the potential-vorticity flux. This equation applies instantaneously, even if the mean fields are evolving in time. It should be noted, however, that the required boundary conditions are not always simple. For example, at the surface (corresponding to the base of the Ekman layer) we need to impose

$$\frac{\partial \chi^*}{\partial y} = \langle w_1 \rangle^* = \langle w_1 \rangle + \frac{\partial}{\partial y} \left(\frac{\left\langle v_0' b_0' \right\rangle}{N^2} \right) \quad \text{at} \quad z = 0. \tag{3.37}$$

Given that the Ekman pumping is

$$\langle w_1 \rangle = -\frac{\partial}{\partial y} \left(\frac{\langle \tau^x \rangle}{\rho_0 f_0} \right) \quad \text{at} \quad z = 0, \tag{3.38}$$

the boundary condition can be integrated to

$$\chi^* = -\frac{\langle \tau^x \rangle}{\rho_0 f_0} + \frac{\left\langle v_0' b_0' \right\rangle}{N^2} \quad \text{at} \quad z = 0. \tag{3.39}$$

So eddy effects can also enter through the boundary conditions, not only through the potential-vorticity flux.

3.3 Eddy parameterization

In order to obtain the mean state of the Southern Ocean from the TEM equations (3.32) to (3.35), we need to specify the eddy fluxes as a function of the mean state. A simple and elegant eddy closure would be to postulate that potential-vorticity is fluxed down-gradient, with some eddy diffusivity K:

$$\left\langle v_0' q' \right\rangle = -K \frac{\partial \langle q \rangle}{\partial y} \tag{3.40}$$

with the mean potential-vorticity gradient

$$\frac{\partial \langle q \rangle}{\partial y} = \beta - \frac{\partial^2 \langle u_0 \rangle}{\partial y^2} + f_0 \frac{\partial}{\partial z}\left(\frac{\partial \langle b_0 \rangle / \partial y}{N^2}\right). \tag{3.41}$$

Despite its elegance, this approach is rarely used in practice. Instead, an even simpler eddy closure is used, which is based on an energy argument.

The dominant source of eddy energy in the Southern Ocean is thought to be the conversion from mean potential energy to eddy potential energy, which in turn is converted into eddy kinetic energy. This is the energetic pathway favored by baroclinic instability, likely the dominant instability in the Southern Ocean. We therefore consider the potential-energy budget of the mean flow by multiplying the mean buoyancy equation (3.16) by $\rho_0 \langle b_0 \rangle / N^2$. After using

$$\frac{\langle b_0 \rangle}{N^2} \frac{\partial}{\partial y} \left\langle v_0' b_0' \right\rangle = \frac{\partial}{\partial y}\left(\frac{\langle b_0 \rangle}{N^2} \left\langle v_0' b_0' \right\rangle\right) - \frac{\left\langle v_0' b_0' \right\rangle}{N^2} \frac{\partial \langle b_0 \rangle}{\partial y}, \tag{3.42}$$

we obtain the evolution equation for the mean potential energy density:

$$\frac{\partial}{\partial t}\left(\frac{\rho_0}{2} \frac{\langle b_0 \rangle^2}{N^2}\right) + \frac{\partial}{\partial y}\left(\frac{\rho_0 \langle b_0 \rangle}{N^2} \left\langle v_0' b_0' \right\rangle\right) = \frac{\rho_0 \left\langle v_0' b_0' \right\rangle}{N^2} \frac{\partial \langle b_0 \rangle}{\partial y} - \rho_0 \langle w_1 \rangle \langle b_0 \rangle. \tag{3.43}$$

The second term on the left is a transport term and therefore can only redistribute mean potential energy. Mean potential energy can be generated or destroyed by two processes, as expressed by the two terms on the right. The first term is the conversion between mean potential energy and eddy potential energy, and the second term is the conversion between mean potential energy and mean kinetic energy.

Mean potential energy is associated with the mean meridional slope of isopycnals. The conversion term with mean kinetic energy allows the Ekman circulation to generate potential energy by steepening up isopycnals. The conversion term with eddy potential energy allows the eddies to flatten isopycnals. The dominant energy pathways from mean to eddy potential energy then motivates one to insist that an eddy closure should always release mean potential energy. The simplest such closure is a down-gradient buoyancy flux closure:

$$\left\langle v_0' b_0' \right\rangle = -K \frac{\partial \langle b_0 \rangle}{\partial y} \quad \text{such that} \quad \frac{\rho_0 \left\langle v_0' b_0' \right\rangle}{N^2} \frac{\partial \langle b_0 \rangle}{\partial y} = -\frac{\rho_0 K}{N^2} \left(\frac{\partial \langle b_0 \rangle}{\partial y}\right)^2 < 0, \tag{3.44}$$

where K again is an eddy diffusivity. This is the central argument of the Gent–McWilliams parameterization, which is nowadays used in practically all climate models that do not explicitly resolve mesoscale eddies.

The down-gradient buoyancy flux closure is accompanied by neglecting the momentum fluxes in the Eliassen–Palm flux. This is generally a reasonable approximation, although it can break down in strong jets, such as those associated with the fronts in the ACC and the extensions of western boundary currents.

Making these assumptions, we can now use the TEM framework to obtain an expression for the residual circulation. In steady state, the TEM momentum balance is now

$$-f_0\langle v_1\rangle^* = f_0\frac{\partial}{\partial z}\left(\frac{\left\langle v_0' b_0'\right\rangle}{N^2}\right). \tag{3.45}$$

Integrating this balance in the vertical to $z = 0$, where (3.39) applies, we find that

$$\chi^* = -\frac{\langle \tau^x\rangle}{\rho_0 f_0} + \frac{\left\langle v_0' b_0'\right\rangle}{N^2}. \tag{3.46}$$

This applies at any depth and allows us to think of the residual circulation as a sum of the wind-driven circulation (first term) and the eddy-driven circulation (second term).

If the flow is adiabatic, as we have assumed throughout, the residual circulation must vanish for the buoyancy field to be steady. Together with the diffusive buoyancy flux closure, this allows us to obtain an expression for the slopes of isopycnals in the Southern Ocean:

$$-\frac{\partial\langle b_0\rangle/\partial y}{N^2} = \frac{\langle \tau^x\rangle}{K\rho_0 f_0}. \tag{3.47}$$

For typical values $\langle \tau^x\rangle = 0.1$ N m^{-2}, $K = 1000$ m^2 s^{-1}, $\rho_0 = 1000$ kg m^{-3}, and $f_0 = -10^{-4}$ s^{-1}, we obtain a slope of -10^{-3} or a descent by 1000 m over a distance of 1000 km. This is roughly consistent with the observed hydrography.

The remaining difficulty is now to find appropriate values for the eddy diffusivity K. The $K = 1000$ m^2 s^{-1} used above is a good order-of-magnitude estimate, but there are significant variations in the real ocean, both in the horizontal and in the vertical. Estimating diffusivities from observations and eddy-resolving numerical simulations is an active area of research. Enabled by increasing computing power, however, many ocean models are moving to resolutions that permit the development of eddies, which overcomes the mesoscale parameterization problem altogether.

Chapter 4

Geostrophic instability and turbulence

We saw that mesoscale eddies play a fundamental role in the Southern Ocean, but these eddies also generate the strongest flows almost everywhere in the world ocean. While we can understand the thermocline circulation without explicitly taking eddies into account, they do modify the thermocline structure (not just by homogenizing potential vorticity in the pool regions). Mesoscale eddies also tend to dominate the horizontal (or isopycnal) transport of tracers such as carbon, oxygen, or nutrients. Motivated by this importance, we now take a closer look at how these eddies are generated through instabilities, and we will discuss some properties of the geostrophic turbulence that ensues.

4.1 Baroclinic instability

Last term, we discussed the Eady model as an archetype for baroclinic instability. We saw that the configuration consisting of a uniform buoyancy gradient between two solid boundaries is unstable at sufficiently large wavelengths. The instability can be understood to arise from the interaction of two counter-propagating edge waves: an edge wave at the lower boundary that propagates eastward and an edge wave at the upper boundary whose intrinsic propagation is westward but which is also Doppler shifted by the eastward mean flow. These two edge waves can propagate in lockstep and mutually amplify.

While the Eady model is a reasonable model for the troposphere, it does not very closely resemble the configuration of the ocean. Except in the Southern Ocean, buoyancy gradients are largely confined to the thermocline. But a variant of the mechanism revealed by the Eady model is at work in much of the ocean as well.

The key to the Eady instability is the availability of counter-propagating edge waves. In the ocean, the role of these edge waves is more typically played by Rossby waves that propagate on potential-vorticity gradients in the interior of the fluid. Since the direction of Rossby wave propagation is set by the potential-vorticity gradient, we anticipate that an instability requires a reversal in the sign of the potential-vorticity gradient. We will see this formally below. But first, we discuss the general structure of potential-vorticity gradients in the ocean.

Given that in the ocean's interior, strong flows are typically zonal, we concentrate on the meridional potential-vorticity gradient associated with zonal flows. In the quasi-geostrophic framework, that potential-vorticity gradient is

$$\frac{\partial Q}{\partial y} = \beta - \frac{\partial^2 U}{\partial y^2} + f_0 \frac{\partial}{\partial z}\left(\frac{\partial B/\partial y}{N^2}\right), \tag{4.1}$$

where we are using capital letters to denote mean-flow quantities. The gradient consists of a planetary-vorticity gradient, a relative-vorticity gradient, and a gradient due to the stretching term. In much of the ocean, the stretching term dominates over the other two terms. If that is the case, we can read off the potential-vorticity gradient directly from the hydrography: the potential-vorticity gradient is proportional to the change of the isopycnal slope

$$s = -\frac{\partial B/\partial y}{N^2} \tag{4.2}$$

with depth,

$$\frac{\partial Q}{\partial y} = -f_0 \frac{\partial s}{\partial z}. \tag{4.3}$$

Tulloch et al. (2011) provided a schematic discussion of these potential-vorticity gradients in the ocean. At the poleward edge of subtropical gyres, the isopycnals generally slope upward toward the pole, so $f_0 s > 0$. The isopycnals first steepen with depth, then flatten again. This implies that $\partial Q/\partial y > 0$ in the upper ocean and $\partial Q/\partial y < 0$ below. There is a reversal of the potential-vorticity gradient that gives rise to instability there. On the equatorial edge of subtropical gyres, isopycnals slope downward toward the pole, so $f_0 s < 0$ there. Again isopycnals first steepen, then flatten with depth, implying a potential-vorticity gradient reversal now from $\partial Q/\partial y < 0$ near the surface to $\partial Q/\partial y > 0$ at depth. This reversal also tends to occur at smaller depths, inducing an instability that does not reach as far into the interior ocean as in at the poleward edge of the gyre. The Southern Ocean behaves much like the poleward edge of gyres, although sloping isopycnals reach much deeper into the ocean.

To understand these instabilities more quantitatively, one can generalize the instability calculation we performed for the Eady model. We consider small perturbations of the mean flow U, which we assume is in thermal-wind balance

$$f_0 \frac{\partial U}{\partial z} = -\frac{\partial B}{\partial y}. \tag{4.4}$$

From the linearized conservation and inversion statements for perturbation potential vorticity, we obtain

$$\frac{\partial q'}{\partial t} + U \frac{\partial q'}{\partial x} + \frac{\partial \psi'}{\partial x}\frac{\partial Q}{\partial y} = 0 \quad \text{and} \quad q' = \frac{\partial^2 \psi'}{\partial x^2} + \frac{\partial^2 \psi'}{\partial y^2} + \frac{\partial}{\partial z}\left(\frac{f_0^2}{N^2}\frac{\partial \psi'}{\partial z}\right). \tag{4.5}$$

The dynamics are completed by the boundary conditions

$$\frac{\partial b_0'}{\partial t} + U\frac{\partial b_0'}{\partial x} + \frac{\partial \psi'}{\partial x}\frac{\partial B}{\partial y} = 0 \quad \text{at} \quad z = -H \quad \text{and} \quad z = 0 \tag{4.6}$$

if we assume the bottom at $z = -H$ to be flat. If we can neglect the relative vorticity contribution to the potential-vorticity gradient and consider the mean flow a function of z only, we can make the plane wave ansatz

$$\psi' = \hat{\psi}(z)e^{i(kx+ly-\omega t)}. \tag{4.7}$$

We then obtain the eigenvalue problem

$$(U-c)\hat{q} + \frac{\partial Q}{\partial y}\hat{\psi} = 0 \quad \text{with} \quad \hat{q} = -\left(k^2+l^2\right)\hat{\psi} + \frac{\partial}{\partial z}\left(\frac{f_0^2}{N^2}\frac{\partial \hat{\psi}}{\partial z}\right). \tag{4.8}$$

We used $c = \omega/k$ to denote the zonal phase speed. The boundary conditions yield

$$(U-c)f_0\frac{\partial \hat{\psi}}{\partial z} + \frac{\partial B}{\partial y}\hat{\psi} = 0 \quad \text{at} \quad z = -H \quad \text{and} \quad z = 0. \tag{4.9}$$

For arbitrary mean flow profiles $U(z)$ and associated $\partial Q/\partial y$ and $\partial B/\partial y$, and for every wavenumber combination k and l, this system can be solved for the eigenvalues c and the eigenfunctions $\hat{\psi}$. Examples of such calculations can be found in Gill et al. (1974), Smith (2007), and Tulloch et al. (2011). One generally finds that the most unstable mode lies close to the local deformation radius and that the growth rate is reasonably predicted by the Eady growth rate.

Our physical discussion above has suggested that we require a change in the sign of the potential-vorticity gradient for an instability to occur, which we can now formalize and make more precise. We will derive a necessary condition for instability that is typically attributed to Charney, Stern, and Pedlosky. We begin by dividing (4.8) by $U-c$, multiplying it with the complex conjugate $\hat{\psi}^*$, and integrating vertically over the domain:

$$\int_{-H}^{0}\left[-\left(k^2+l^2\right)|\hat{\psi}|^2 + \hat{\psi}^*\frac{\partial}{\partial z}\left(\frac{f_0^2}{N^2}\frac{\partial \hat{\psi}}{\partial z}\right)\right]\mathrm{d}z + \int_{-H}^{0}\frac{\partial Q/\partial y}{U-c}|\hat{\psi}|^2\,\mathrm{d}z = 0. \tag{4.10}$$

Using integration by parts and plugging in the boundary conditions (4.9), we can rewrite the second term of the first integral as

$$\left[\frac{f_0^2}{N^2}\hat{\psi}^*\frac{\partial \hat{\psi}}{\partial z}\right]_{-H}^{0} - \int_{-H}^{0}\frac{f_0^2}{N^2}\left|\frac{\partial \hat{\psi}}{\partial z}\right|^2\mathrm{d}z = -\left[\frac{f_0}{N^2}\frac{\partial B/\partial y}{U-c}|\hat{\psi}|^2\right]_{-H}^{0} - \int_{-H}^{0}\frac{f_0^2}{N^2}\left|\frac{\partial \hat{\psi}}{\partial z}\right|^2\mathrm{d}z. \tag{4.11}$$

Substituting this back into (4.10) then yields

$$-\int_{-H}^{0}\left[\left(k^2+l^2\right)|\hat{\psi}|^2 + \frac{f_0^2}{N^2}\left|\frac{\partial \hat{\psi}}{\partial z}\right|^2\right]\mathrm{d}z - \left[\frac{f_0}{N^2}\frac{\partial B/\partial y}{U-c}|\hat{\psi}|^2\right]_{-H}^{0} + \int_{-H}^{0}\frac{\partial Q/\partial y}{U-c}|\hat{\psi}|^2\,\mathrm{d}z = 0. \tag{4.12}$$

The first term here is evidently always real. Since

$$\frac{1}{U-c}=\frac{U-c^*}{|U-c|^2}, \tag{4.13}$$

we can isolate the imaginary part of this equation as follows:

$$(\operatorname{Im} c)\left(-\left[\frac{f_0}{N^2}\frac{\partial B/\partial y}{|U-c|^2}|\hat{\psi}|^2\right]_{-H}^{0}+\int_{-H}^{0}\frac{\partial Q/\partial y}{|U-c|^2}|\hat{\psi}|^2\,\mathrm{d}z\right)=0. \tag{4.14}$$

This equation, although seemingly complicated, provides us with a relatively simple necessary criterion for instability. Instability requires that $\operatorname{Im} c > 0$, so this constraint can only be satisfied if the bracketed term vanishes. Given that all other factors are positive, this can occur only if there are contributions of different signs arising from $\partial Q/\partial y$ at different depths and $f_0 \partial B/\partial y$ at the boundaries. For instability, we thus require at least one of the following:

1. $\partial Q/\partial y$ changes sign somewhere in the domain,
2. $f_0 \partial B/\partial y$ has the same sign on both boundaries,
3. $\partial Q/\partial y$ has the opposite sign of $f_0 \partial B/\partial y$ at $z=-H$,
4. $\partial Q/\partial y$ has the same sign as $f_0 \partial B/\partial y$ at $z=0$.

The Eady model satisfies the second condition. Another archetypal model for the atmosphere is $\partial Q/\partial y=\beta$ and $f_0 \partial B/\partial y<0$ at the surface, which satisfies the third condition. The arising instability is called a “Charney instability.” None of these conditions is satisfied if $\partial Q/\partial y=\beta$ and $f_0 \partial B/\partial y=0$—this configuration yields propagating Rossby waves, as we have seen previously. These necessary conditions for instability are exactly those expected from our physical argument about counter-propagating interior Rossby waves and Eady edge waves.

4.2 Barotropic instability

Baroclinic instability, arguably the most important instability in the ocean, relies on a change in sign of the quasi-geostrophic potential-vorticity gradient in the vertical that arise largely from the stretching contribution to potential vorticity. But in regions of strong currents, instability can also occur because of relative-vorticity gradients. These are called “barotropic instabilities.”

We consider a simple example of barotropic instability, the following parallel shear flow:

$$U=\begin{cases}\frac{\Delta}{2} & y>\frac{L}{2},\\ \frac{\Delta y}{L} & -\frac{L}{2}<y<\frac{L}{2},\\ -\frac{\Delta}{2} & y<-\frac{L}{2}.\end{cases} \tag{4.15}$$

We assume $\beta = 0$ and no z-dependence, i.e., we can consider this flow to be two-dimensional. This flow has kinks at $y = \pm L/2$ and has constant vorticity

$$Q = -\frac{\partial U}{\partial y} \tag{4.16}$$

within each of the three subregions. The vorticity gradient is thus concentrated into sheets at $y = \pm L/2$. As we will formalize in the following, this gives rise to counter-propagating Rossby waves that at large-enough scales interact and give rise to instability. The dynamics are completely analogous to the Eady model.

The linearized equations of motion are

$$\frac{\partial q'}{\partial t} + U\frac{\partial q'}{\partial x} + \frac{\partial \psi'}{\partial x}\frac{\partial Q}{\partial y} = 0, \qquad q' = \frac{\partial^2 \psi'}{\partial x^2} + \frac{\partial^2 \psi'}{\partial y^2}. \tag{4.17}$$

We make a wave ansatz in the homogeneous x-dimension and in time:

$$q' = \hat{q}(y)e^{i(kx-\omega t)}, \qquad \psi' = \hat{\psi}(y)e^{i(kx-\omega t)}. \tag{4.18}$$

Away from $y = \pm L/2$, there are no potential-vorticity gradients, so if there are no potential-vorticity anomalies initially, we have $q' = 0$ for all time. We therefore have

$$-k^2\hat{\psi} + \frac{\partial^2 \hat{\psi}}{\partial y^2} = 0. \tag{4.19}$$

Applying decay conditions for $y \to \pm\infty$, we can therefore write down the general solution as

$$\hat{\psi} = \begin{cases} Ae^{-k\left(y-\frac{L}{2}\right)} & y > \frac{L}{2}, \\ Be^{k\left(y-\frac{L}{2}\right)} + Ce^{-k\left(y+\frac{L}{2}\right)} & -\frac{L}{2} < y < \frac{L}{2}, \\ De^{k\left(y+\frac{L}{2}\right)} & y < -\frac{L}{2}. \end{cases} \tag{4.20}$$

The streamfunction decays exponentially away from the interfaces at $y = \pm L/2$, with a decay scale given by k^{-1}. The meridional decay scale is proportional to the zonal wavelength of the perturbation. One can already anticipate at this point that an instability is possible only at scales with $kL \sim 1$. Otherwise, the dynamics of the two interfaces are decoupled.

The general solutions in the three subregions must be matched at the interfaces. Given that there are four unknowns, we need two matching conditions per interface. The first of these is that the interfaces are material surfaces. We express this in terms of the meridional interface displacement η':

$$\frac{\partial \eta'}{\partial t} + U\frac{\partial \eta'}{\partial x} = \frac{\partial \psi'}{\partial x}. \tag{4.21}$$

This equation must hold on both sides of the interface for the same displacement η'. This requires that $\hat{\psi}$ is continuous at $y = \pm L/2$, so

$$A = B + Ce^{-kL} \quad \text{and} \quad D = Be^{-kL} + C. \tag{4.22}$$

The second condition is that the pressure field must be continuous across the interfaces. To derive the resulting condition, we begin with the zonal momentum equation

$$\frac{\partial u_0'}{\partial t} + U\frac{\partial u_0'}{\partial x} + \frac{\partial \psi'}{\partial x}\frac{\partial U}{\partial y} - f_0 v_1' = -\frac{1}{\rho_0}\frac{\partial p_1'}{\partial x}. \tag{4.23}$$

Since for this two-dimensional flow

$$\frac{\partial u_1'}{\partial x} + \frac{\partial v_1'}{\partial y} = 0, \tag{4.24}$$

we can introduce a streamfunction ψ_1' for this first-order flow. Then redefining the pressure as $p_1' \mapsto p_1' + f_0\rho_0\psi_1'$ eliminates rotation from the problem. This is a general result: uniform rotation has no effect on nondivergent two-dimensional flow. With this redefinition, we are left with the momentum equation

$$\frac{\partial u_0'}{\partial t} + U\frac{\partial u_0'}{\partial x} + \frac{\partial \psi'}{\partial x}\frac{\partial U}{\partial y} = -\frac{1}{\rho_0}\frac{\partial p_1'}{\partial x} \tag{4.25}$$

which with a wave ansatz becomes

$$(U-c)\frac{\partial \hat{\psi}}{\partial y} - \hat{\psi}\frac{\partial U}{\partial y} = \frac{\hat{p}_1}{\rho_0}. \tag{4.26}$$

Pressure continuity then implies that the left side of this equation must be the same on either side of the interface. This yields the conditions

$$-\left(\frac{\Delta}{2}-c\right)kA = \left(\frac{\Delta}{2}-c\right)k\left(B - Ce^{-kL}\right) - \frac{\Delta}{L}\left(B + Ce^{-kL}\right), \tag{4.27}$$

$$\left(-\frac{\Delta}{2}-c\right)kD = \left(-\frac{\Delta}{2}-c\right)k\left(Be^{-kL} - C\right) - \frac{\Delta}{L}\left(Be^{-kL} + C\right). \tag{4.28}$$

We now have four equations for four unknowns that can be summarized with the coefficient matrix

$$M = \begin{pmatrix} 1 & -1 & -e^{-kL} & 0 \\ 0 & -e^{-kL} & -1 & 1 \\ \left(\frac{1}{2}-\frac{c}{\Delta}\right)kL - 1 & \left(\frac{1}{2}-\frac{c}{\Delta}\right)kL & -\left(\frac{1}{2}-\frac{c}{\Delta}\right)kLe^{-kL} & 0 \\ 0 & -\left(\frac{1}{2}+\frac{c}{\Delta}\right)kLe^{-kL} & \left(\frac{1}{2}+\frac{c}{\Delta}\right)kL & \left(\frac{1}{2}+\frac{c}{\Delta}\right)kL - 1 \end{pmatrix} \tag{4.29}$$

For our problem to have nontrivial solutions, we require that the determinant of M vanishes, which yields the dispersion relation

$$c = \pm\frac{\Delta}{2kL}\sqrt{(1-kL)^2 - e^{-2kL}}. \tag{4.30}$$

This dispersion relation indicates instability for $kL < 1.3$ (Fig. 4.1). The most unstable mode occurs at $kL = 0.8$ with a growth rate $\sigma = k\,\mathrm{Im}\,c = 0.2\Delta/L$. All unstable

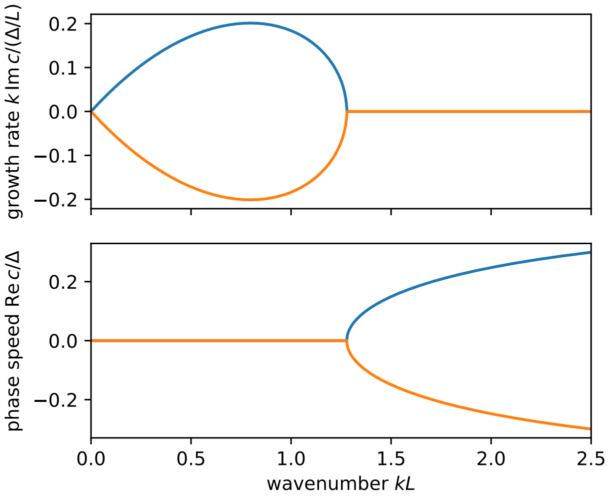

Figure 4.1: Barotropic instability of a parallel shear flow. Shown are the nondimensional growth rate and phase speed as obtained from the dispersion relation. The two branches are shown in blue and orange.

modes are phase-locked with $\mathrm{Re}\,c = 0$. The stable modes are decoupled edge waves propagating on the interfaces.

The instability thus grows at scales at which edge waves propagating on the two vorticity sheets at $y = \pm L/2$ can interact. The instability is again produced by counter-propagating Rossby waves that phase-lock and mutually amplify. The dynamics are the same as for baroclinic instability, except that now the phase-locking occurs in the horizontal. Barotopic instabilities grow at the expense of the kinetic energy of the mean flow, rather than its potential energy. Once the instability reaches finite amplitude, it produces geostrophic turbulence. In the ocean, especially at strong currents, this contributes to the energization of mesoscale eddies.

4.3 Triad interactions

Much of our discussion of time-dependent flow so far has relied on linear dynamics. We have regularly assumed flow perturbations to be sufficiently small to linearize the equations of motion. For example, our linear stability calculations for baroclinic and barotropic currents allowed us to understand the mechanisms behind these instabilities. But the conditions for linearization are not typically satisfied in the real ocean: the perturbations produced by the instabilities—mesoscale eddies—have large-enough amplitudes for nonlinear terms to become of leading-order importance. The mesoscale eddy field is more aptly described as geostrophic turbulence than linear perturbations to a mean flow. Nonlinearity leads to spatial and temporal disorder, both hallmarks of turbulence. Any serious description of the ocean circulation must take this nonlinearity into account.

Nonlinearity makes describing and understanding turbulent flows a much more challenging problem, one that has vexed researchers for centuries. Heisenberg and Lamb have famously been quoted to have more hope for enlightenment about relativity and quantum electrodynamics than about turbulence. At the core of the difficulty is that nonlinearity couples together different spatial modes, so we cannot treat them separately as we have been doing to great effect in our linear calculations. This allows energy transfer between modes and hence between scales.

To understand how nonlinearity couples modes and thus allows energy transfer, we consider as a model system two-dimensional incompressible flow in a periodic box. We use this example for illustrative purposes—the general result that nonlinearity allows energy transfer between modes equally applies to three-dimensional flow. There are important differences between two- and three-dimensional turbulence, with important implications for the ocean, which is something we will return to.

The equations of motion for incompressible two-dimensional flow can be cast in terms of a vorticity equation. The equations of motion are

$$\frac{\partial u}{\partial t}+u\frac{\partial u}{\partial x}+v\frac{\partial u}{\partial y}=-\frac{1}{\rho_0}\frac{\partial p}{\partial x}, \tag{4.31}$$

$$\frac{\partial v}{\partial t}+u\frac{\partial v}{\partial x}+v\frac{\partial v}{\partial y}=-\frac{1}{\rho_0}\frac{\partial p}{\partial y}, \tag{4.32}$$

$$\frac{\partial u}{\partial x}+\frac{\partial v}{\partial y}=0. \tag{4.33}$$

Cross-differentiating the momentum equations and making use of the continuity equation yields the vorticity equation

$$\frac{\partial \zeta}{\partial t}+\mathrm{J}(\psi,\zeta)=0 \quad \text{with} \quad \zeta=\frac{\partial v}{\partial x}-\frac{\partial u}{\partial y}=\nabla^2\psi \tag{4.34}$$

and the usual definition of the streamfunction:

$$u=-\frac{\partial \psi}{\partial y} \quad \text{and} \quad v=\frac{\partial \psi}{\partial x}. \tag{4.35}$$

We suppose that the flow is contained in a box with side length L and that the flow is doubly periodic. The latter condition states that $\psi(0,y)=\psi(L,y)$ for all y and $\psi(x,0)=\psi(x,L)$ for all x. Any flow leaving the box on one side is returned on the other side of the box.

Turbulence theory is often formulated in spectral space, with the interaction between different Fourier modes taking center stage. A meaningful description of turbulence in spectral space requires spatial homogeneity of the turbulence, which is understood as a requirement that the statistics of the turbulence are homogeneous. We typically also assume isotropy. Both conditions are never exactly satisfied for the ocean, but they are useful idealizations. Isotropy is broken at sufficiently large scales, for example, by the planetary vorticity gradient. With the aim to understand turbulence in its simplest form, we ignore such complications in what follows.

We decompose the flow into spatial Fourier modes:

$$\psi(x,y,t)=\sum_{\boldsymbol{k}}\hat{\psi}(\boldsymbol{k},t)e^{i\boldsymbol{k}\cdot\boldsymbol{x}} \quad \text{and} \quad \zeta(x,y,t)=\sum_{\boldsymbol{k}}\hat{\zeta}(\boldsymbol{k},t)e^{i\boldsymbol{k}\cdot\boldsymbol{x}}, \tag{4.36}$$

where $\boldsymbol{k}=k^x\boldsymbol{x}+k^y\boldsymbol{y}$ is the two-dimensional wavenumber vector, and the summation is understood to be over all wavenumbers $k^x=2\pi n/L$ and $k^y=2\pi m/L$ with integers n and m. Substituting these Fourier series into the vorticity equation (4.34) yields

$$\frac{\partial}{\partial t}\sum_{\boldsymbol{k}}\hat{\zeta}(\boldsymbol{k},t)e^{i\boldsymbol{k}\cdot\boldsymbol{x}}+\left(\sum_{\boldsymbol{p}}ip^x\hat{\psi}(\boldsymbol{p},t)e^{i\boldsymbol{p}\cdot\boldsymbol{x}}\right)\left(\sum_{\boldsymbol{q}}iq^y\hat{\zeta}(\boldsymbol{q},t)e^{i\boldsymbol{q}\cdot\boldsymbol{x}}\right)$$
$$-\left(ip^y\sum_{\boldsymbol{p}}\hat{\psi}(\boldsymbol{p},t)e^{i\boldsymbol{p}\cdot\boldsymbol{x}}\right)\left(iq^x\sum_{\boldsymbol{q}}\hat{\zeta}(\boldsymbol{q},t)e^{i\boldsymbol{q}\cdot\boldsymbol{x}}\right)=0 \tag{4.37}$$

and

$$\hat{\zeta}(\boldsymbol{k},t)=-|\boldsymbol{k}|^2\hat{\psi}(\boldsymbol{k},t). \tag{4.38}$$

To get an evolution equation for $\hat{\zeta}(\boldsymbol{k},t)$, we now project the above equation onto a single Fourier mode. We multiply the equation by $e^{-i\boldsymbol{k}'\cdot\boldsymbol{x}}$, integrate over the domain, and take advantage of the fact that Fourier modes are orthogonal:

$$\iint e^{i\boldsymbol{p}\cdot\boldsymbol{x}}e^{i\boldsymbol{q}\cdot\boldsymbol{x}}\,\mathrm{d}^2\boldsymbol{x}=L^2\delta_{\boldsymbol{p}+\boldsymbol{q}}, \tag{4.39}$$

where $\delta_{\boldsymbol{k}}=1$ for $\boldsymbol{k}=0$ and $\delta_{\boldsymbol{k}}=0$ otherwise. We thus arrive at the evolution equation

$$\frac{\partial}{\partial t}\hat{\psi}(\boldsymbol{k},t)=\sum_{\boldsymbol{p},\boldsymbol{q}}\frac{|\boldsymbol{q}|^2}{|\boldsymbol{k}|^2}(p^xq^y-p^yq^x)\,\hat{\psi}(\boldsymbol{p})\,\hat{\psi}(\boldsymbol{q})\,\delta_{\boldsymbol{p}+\boldsymbol{q}-\boldsymbol{k}}. \tag{4.40}$$

The summation here is over all wavenumber $\boldsymbol{p}$ and $\boldsymbol{q}$, but only those with $\boldsymbol{p}+\boldsymbol{q}=\boldsymbol{k}$ make a contribution. The wavenumbers satisfying this condition are called a “triad.” This shows that the streamfunction (and thus the flow) at wavenumber $\boldsymbol{k}$ evolves due to flow at wavenumbers $\boldsymbol{p}$ and $\boldsymbol{q}$. Triads couple together different Fourier modes—and thus different scales of motion. This role of triads is a consequence of the quadratic nonlinearity of the equations of motion.

Triads can be categorized into “local” and “nonlocal” triads. The wavenumbers forming local triads have similar lengths, $|\boldsymbol{k}|\sim|\boldsymbol{p}|\sim|\boldsymbol{q}|$. Nonlocal triads, instead, are made up of two wavenumbers of similar length and one wavenumber that is much smaller, e.g., $|\boldsymbol{k}|\sim|\boldsymbol{p}|\gg|\boldsymbol{q}|$. Local triads correspond to the interaction between scales that are not too different from one another, whereas nonlocal triads correspond to the interaction between one large-scale mode with two small-scale modes. The condition $\boldsymbol{p}+\boldsymbol{q}=\boldsymbol{k}$ prevents triads from involving two small and one large wavenumber.

Triad interactions are at the core of turbulence. They allow the interaction and energy exchange between scales. We will argue that local triad interactions are dominant in the transfer of energy, but there is no rigorous justification for this. Intuitively, eddies of similar scale can more easily deform one another than a very large and a very small eddy.

The energy transfer across scales by triad interactions allows turbulence to connect scales at which energy is put into the system (the forcing scale) with the scale at which energy is dissipated (the dissipation scale). We will discuss next how this happens in three-dimensional turbulence, and we will develop a theory for how energy is distributed across scales. This is Kolmogorov's celebrated theory of three-dimensional homogeneous turbulence, which applies approximately to mixed-layer other small-scale turbulence in the ocean.

4.4 Three-dimensional turbulence

We now discuss a cornerstone of turbulence theory: Kolmogorov's (1941) theory that predicts the energy spectrum for three-dimensional homogeneous and isotropic turbulence. This is arguably the simplest form of turbulence and therefore a good place to start our quantitative description of turbulence. While the ocean is seldom homogeneous and isotropic, these conditions apply approximately at small-enough scales. For example, the atmospherically forced turbulence in the surface boundary layer is three-dimensional, as is the turbulence induced by the breaking of internal waves in the ocean interior. Principles from this theory are indeed used in practice to measure the levels of turbulence using microstructure probes (discussed later in the course).

We consider a triply periodic box of side length L that is filled with a constant-density fluid. The system is not rotating and therefore has the equations of motion

$$\frac{\partial \boldsymbol{u}}{\partial t} + (\boldsymbol{u} \cdot \nabla)\boldsymbol{u} = -\frac{\nabla p}{\rho} + \boldsymbol{F} + \nu \nabla^2 \boldsymbol{u}, \tag{4.41}$$

$$\nabla \cdot \boldsymbol{u} = 0. \tag{4.42}$$

The fluid is experiencing a body force $\boldsymbol{F}$ that acts at a relatively large scale given by $k_0^{-1} = L_0$. The last term in the momentum equation is due to viscous stresses: the fluid is experiencing momentum diffusion proportional to the molecular viscosity ν.

The energy budget, obtained by dotting the momentum equation with $\boldsymbol{u}$ (we divide the energy by the constant ρ) and integrating over the domain, is

$$\frac{\mathrm{d}}{\mathrm{d}t} \iiint \frac{|\boldsymbol{u}|^2}{2}\, \mathrm{d}^3\boldsymbol{x} = \iiint \left(\boldsymbol{F} \cdot \boldsymbol{u} - \nu |\nabla \boldsymbol{u}|^2 \right) \mathrm{d}^3\boldsymbol{x}. \tag{4.43}$$

To reach a (statistically) steady state, the energy input by the forcing must be balanced by viscous dissipation. If we do a scale analysis for the size of the viscous term compared to the inertial terms in the momentum equation, we find

$$(\boldsymbol{u} \cdot \nabla)\boldsymbol{u} \sim \frac{U^2}{L_0} \quad \text{and} \quad \nu \nabla^2 \boldsymbol{u} \sim \frac{\nu U}{L_0^2}, \tag{4.44}$$

so their ratio scales like

$$\mathrm{Re} = \frac{UL_0}{\nu}. \tag{4.45}$$

This ratio is called the "Reynolds number" of the flow and is often very large for realistic flows. For mixed-layer turbulence, typical scales might be

$$U \sim 0.01 \text{ m s}^{-1} \quad \text{and} \qquad L_0 \sim 10 \text{ m}, \tag{4.46}$$

and the viscosity for seawater is about $\nu = 10^{-6}$ m^2 s^{-1}, such that Re $\sim 10^5$. This would suggest that the viscous term is extremely small and inconsequential for the evolution of the flow. So how can it then close the energy budget? The answer is that turbulent scale interactions transfer the energy from the forcing scale down to small scales, where the viscous term becomes large:

$$\frac{U_\nu L_\nu}{\nu} \sim 1 \tag{4.47}$$

at the viscous scale

$$L_\nu \sim \frac{\nu}{U_\nu}, \tag{4.48}$$

where U_ν is an as yet undetermined velocity scale at this viscous scale. The forcing scale $L_0 = k_0^{-1}$ is thus connected to the dissipation scale $L_\nu = k_\nu^{-1}$ by turbulent scale interactions that transfer energy from the forcing to the dissipation scale across a range of scales in which neither forcing nor dissipation are important. Because of the dominance of inertial terms, this range of scales is called the "inertial range."

Given this phenomenology, what can we say quantitatively about the turbulence? It turns out that this phenomenology leads to a relatively straightforward prediction of the energy spectrum. Writing the flow in terms of a Fourier series,

$$\boldsymbol{u}(\boldsymbol{x}, t) = \sum_{\boldsymbol{k}} \hat{\boldsymbol{u}}(\boldsymbol{k}, t) e^{i\boldsymbol{k}\cdot\boldsymbol{x}}, \tag{4.49}$$

we can express the energy density in terms of the Fourier components:

$$\frac{1}{L^3} \iiint \frac{\left\langle |\boldsymbol{u}|^2 \right\rangle}{2} \, \mathrm{d}^3\boldsymbol{x} = \sum_{\boldsymbol{k}} \frac{\left\langle |\hat{\boldsymbol{u}}|^2 \right\rangle}{2} = \sum_{\boldsymbol{k}} E(\boldsymbol{k}), \tag{4.50}$$

where $E(\boldsymbol{k})$ is the energy spectrum. The angle brackets here denote an average over the fluctuations of the turbulence. The turbulent flow is disordered in space and time, and different initial conditions give rise to different evolutions. We can take the average to be an average over an ensemble of such statistically identical realizations of the flow. The identity above is the result of Parseval's theorem. The spectrum $E(\boldsymbol{k})$ is defined at discrete wavenumbers, but it turns into a continuous spectrum as we make our box infinitely large. Also assuming isotropy, we can write

$$\lim_{L\to\infty} \frac{1}{L^3} \iiint \frac{\left\langle |\boldsymbol{u}|^2 \right\rangle}{2} \, \mathrm{d}^3\boldsymbol{x} = \int \mathcal{E}(k) \, \mathrm{d}k, \quad \text{where} \quad k = |\boldsymbol{k}|. \tag{4.51}$$

The energy spectrum $\mathscr{E}(k)$ measures the distribution of energy across spatial scales. Our goal is a prediction for $\mathscr{E}(k)$, which is arguably the most important descriptor of the statistics of the turbulence.

Let us now assume that the rate of energy input by the forcing is ε. In steady state, the energy input must be balanced by dissipation, so the dissipation rate must also be ε. Consequently, turbulent scale interactions must transfer energy at this rate from the forcing to the dissipation scales. We posit that this scale transfer is dominated by local triad interactions. This is a reasonable assumption but cannot be justified rigorously. This assumption means that the energy transfer occurs in small steps in wavenumber space and is therefore referred to as an "energy cascade."

With this assumption in hand, we can now infer the shape of $\mathscr{E}(k)$ in the inertial range. Within this range, the flow is independent of the forcing and dissipation, so $\mathscr{E}(k)$ should be a function of the transfer rate ε and the local wavenumber k only. Other wavenumbers do not enter because of the locality assumption. We can then infer $\mathscr{E}(k)$ based on dimensional analysis. The energy spectrum gives the energy per unit wavenumber, so $\mathscr{E}(k)$ has units length^3 time^{-2}. The energy transfer rate ε has dimensions length^2 time^{-3}, and the units of k are length^{-1}. To match the time units, we require $\mathscr{E}(k) \sim e^{2/3}$. To match the length units, we thus require

$$\mathscr{E}(k) \sim e^{\frac{2}{3}} k^{-\frac{5}{3}}. \tag{4.52}$$

This is Kolmogorov's famous prediction for a spectral slope of $-5/3$. Despite the heuristic nature of the argument—note that we did not derive the prediction directly from the equations of motion—this prediction has proven very accurate. It is consistent with experiments and with numerical simulations. It is a remarkably simple prediction for a complicated disordered flow.

4.5 Two-dimensional turbulence

An important property of three-dimensional turbulence is that dissipation is finite in the limit $\nu \to 0$. The energy cascade produces vortex stretching and folding that leads to ever stronger velocity gradients until, at small-enough scales, the energy gets dissipated. This is how a balance between energy input and dissipation can be achieved:

$$\varepsilon = \frac{1}{L^3} \iiint \boldsymbol{F} \cdot \boldsymbol{u} \, \mathrm{d}^3\boldsymbol{x} = \frac{1}{L^3} \iiint \nu |\nabla \boldsymbol{u}|^2 \, \mathrm{d}^3\boldsymbol{x}. \tag{4.53}$$

This is not true for two-dimensional turbulence, fundamentally because vorticity is now conserved. Vortex stretching is absent and velocity gradients cannot grow without bounds.

Let us consider two-dimensional dynamics with forcing and dissipation:

$$\frac{\partial \zeta}{\partial t} + \mathrm{J}(\psi, \zeta) = \boldsymbol{z} \cdot (\nabla \times \boldsymbol{F}) + \nu \nabla^2 \zeta \quad \text{with} \quad \zeta = \nabla^2 \psi. \tag{4.54}$$

We can form the energy budget by multiplying the vorticity equation by $-\psi$ and integrating over the domain. The tendency term yields

$$-\iint \psi \frac{\partial \zeta}{\partial t}\, \mathrm{d}^2\boldsymbol{x} = -\iint \psi \frac{\partial}{\partial t}\left(\nabla^2\psi\right) \mathrm{d}^2\boldsymbol{x} = \iint \nabla\psi\cdot\frac{\partial}{\partial t}(\nabla\psi)\, \mathrm{d}^2\boldsymbol{x} = \frac{\mathrm{d}}{\mathrm{d}t}\iint \frac{|\nabla\psi|^2}{2}\, \mathrm{d}^2\boldsymbol{x}. \tag{4.55}$$

The integrand in the final expression can be identified as the kinetic-energy density (divided by density). The nonlinear term in the vorticity only redistributes energy:

$$-\iint \psi\, \mathrm{J}(\psi,\zeta)\, \mathrm{d}^2\boldsymbol{x} = 0. \tag{4.56}$$

The forcing term yields, as expected, the work done by the forcing:

$$-\iint \psi \boldsymbol{z}\cdot(\nabla\times\boldsymbol{F})\, \mathrm{d}^2\boldsymbol{x} = -\iint \boldsymbol{F}\cdot(\nabla\times\psi\boldsymbol{z})\, \mathrm{d}^2\boldsymbol{x} = \iint \boldsymbol{F}\cdot\boldsymbol{u}\, \mathrm{d}^2\boldsymbol{x}. \tag{4.57}$$

The dissipation term is most usefully written as:

$$-\nu\iint \psi\nabla^2\zeta\, \mathrm{d}^2\boldsymbol{x} = \nu\iint \nabla\psi\cdot\nabla\zeta\, \mathrm{d}^2\boldsymbol{x} = -\nu\iint \zeta^2\, \mathrm{d}^2\boldsymbol{x}. \tag{4.58}$$

The full energy budget thus reads

$$\frac{\mathrm{d}}{\mathrm{d}t}\iint \frac{|\nabla\psi|^2}{2}\, \mathrm{d}^2\boldsymbol{x} = \iint \boldsymbol{F}\cdot\boldsymbol{u}\, \mathrm{d}^2\boldsymbol{x} - \nu\iint \zeta^2\, \mathrm{d}^2\boldsymbol{x}. \tag{4.59}$$

As before, a statistically steady state requires a balance between forcing and dissipation.

The dissipation is proportional to the enstrophy

$$\iint \frac{\zeta^2}{2}\, \mathrm{d}^2\boldsymbol{x}. \tag{4.60}$$

Unlike in three-dimensional turbulence, the dissipation cannot remain finite as $\nu \to 0$ because the enstrophy itself is a conserved quantity of unforced and frictionless two-dimensional flow. The full enstrophy budget is obtained by multiplying the vorticity equation by ζ and integrating over the domain:

$$\frac{\mathrm{d}}{\mathrm{d}t}\iint \frac{\zeta^2}{2}\, \mathrm{d}^2\boldsymbol{x} = \iint \zeta\boldsymbol{z}\cdot(\nabla\times\boldsymbol{F})\, \mathrm{d}^2\boldsymbol{x} - \nu\iint |\nabla\zeta|^2\, \mathrm{d}^2\boldsymbol{x}. \tag{4.61}$$

In two-dimensional turbulence, scale interactions cannot create large velocity gradients that allow energy dissipation even if $\nu \to 0$, the high-Reynolds-number limit, because of the enstrophy constraint. The enstrophy constraint makes two-dimensional turbulence behave fundamentally differently from three-dimensional turbulence. Energy, in fact, is transferred to large rather than small scales.

This can be illustrated by a decay experiment. If two-dimensional turbulence is generated by an initially random vorticity field, larger and larger vortices for over time through progressive mergers. Energy is transferred to progressively larger scales—away from the small scales where it could be dissipated.

Let us consider a heuristic argument for why this should be expected. Imagine an initially strongly peaked energy spectrum $\mathscr{E}(k)$, corresponding to energy concentrated close to a particular length scale. Scale interactions will redistribute this energy across wavenumbers, so they will entail a broadening of the energy spectrum. We assume forcing and dissipation are not important in this evolution, and then ask: how does the dominant scale of the motion respond to the broadening of the energy spectrum? We define the dominant scale as the centroid of the energy spectrum $\mathscr{E}(k)$:

$$k_\mathrm{e} = \frac{\int k\mathscr{E}(k)\,\mathrm{d}k}{\int \mathscr{E}(k)\,\mathrm{d}k}. \tag{4.62}$$

The broadening of the energy spectrum implies that the second moment of the energy spectrum increases:

$$\frac{\mathrm{d}}{\mathrm{d}t}\left(\frac{\int (k-k_\mathrm{e})^2\mathscr{E}(k)\,\mathrm{d}k}{\int \mathscr{E}(k)\,\mathrm{d}k}\right) > 0. \tag{4.63}$$

We can write this second moment as

$$\frac{\int (k-k_\mathrm{e})^2\,\mathscr{E}(k)\,\mathrm{d}k}{\int \mathscr{E}(k)\,\mathrm{d}k} = \frac{\int k^2\mathscr{E}(k)\,\mathrm{d}k}{\int \mathscr{E}(k)\,\mathrm{d}k} - \frac{2k_\mathrm{e}\int k\mathscr{E}(k)\,\mathrm{d}k}{\int \mathscr{E}(k)\,\mathrm{d}k} + \frac{k_\mathrm{e}^2\int \mathscr{E}(k)\,\mathrm{d}k}{\int \mathscr{E}(k)\,\mathrm{d}k} = \frac{\int \mathscr{Z}(k)\,\mathrm{d}k}{\int \mathscr{E}(k)\,\mathrm{d}k} - k_\mathrm{e}^2, \tag{4.64}$$

where $\mathscr{Z}(k)$ is the enstrophy spectrum, defined analogously to $\mathscr{E}(k)$. Energy and enstrophy conservation imply that

$$\frac{\mathrm{d}}{\mathrm{d}t}\left(\int \mathscr{E}(k)\,\mathrm{d}k\right) = 0 \quad \text{and} \quad \frac{\mathrm{d}}{\mathrm{d}t}\left(\int \mathscr{Z}(k)\,\mathrm{d}k\right) = 0, \tag{4.65}$$

which in turn imply that

$$\frac{\mathrm{d}}{\mathrm{d}t}\left(k_\mathrm{e}^2\right) = 2k_\mathrm{e}\frac{\mathrm{d}k_\mathrm{e}}{\mathrm{d}t} = -\frac{\mathrm{d}}{\mathrm{d}t}\left(\frac{\int (k-k_\mathrm{e})^2\mathscr{E}(k)\,\mathrm{d}k}{\int \mathscr{E}(k)\,\mathrm{d}k}\right) < 0. \tag{4.66}$$

The centroid of the energy spectrum thus moves to smaller wavenumber, i.e., larger scales. Scale interactions in two-dimensional flow tend to transfer energy to large scales.

In contrast to energy, enstrophy can move to small scales and be dissipated as $\nu \to 0$. Enstrophy dissipation depends on the vorticity gradients, which unlike vorticity can grow without bounds. This suggests that there are two cascades in two-dimensional turbulence: an energy cascade to large scales and an enstrophy cascade to small scales. Imagining forcing at some intermediate scale to generate energy at a rate ε and enstrophy at a rate η, we conclude there energy is cascaded to ever larger scales until it is remove by some process that acts at large scales, for example bottom drag. In an inertial range in which neither forcing nor drag acts, we can apply the same dimensional argument as in three-dimensional turbulence and obtain the prediction

$$\mathscr{E}(k) \sim \varepsilon^{\frac{2}{3}} k^{-\frac{5}{3}}. \tag{4.67}$$

While the energy spectrum is predicted to have the same shape, the physics are fundamentally different, and the direction of energy transfer is reversed. In the enstrophy range, we can apply a similar argument, but now the energy spectrum depends on the enstrophy rather than the energy flux. The enstrophy flux η has units time^{-3}, such that we arrive at the prediction

$$\mathscr{E}(k) \sim \eta^{\frac{2}{3}} k^{-3}. \tag{4.68}$$

The energy spectrum in the enstrophy range is significantly steeper than in the energy cascade range.

The prediction for a steep spectrum in the enstrophy range is somewhat problematic because it is on the edge of where scale interactions become predominantly nonlocal. Nevertheless, this prediction is largely consistent with experiment and simulation.

4.6 Geostrophic turbulence

Mesoscale eddies are not two-dimensional. They occur in a stratified ocean, generated by baroclinic instability that crucially involves vertically sheared currents. Nevertheless, the geostrophic constraint makes mesoscale eddies behave much more like two-dimensional turbulence than three-dimensional turbulence, albeit with a richer phenomenology.

The fundamental reason geostrophic turbulence in the ocean behaves much like two-dimensional turbulence is that it also has two conservation laws. The conservation of kinetic energy in two-dimensional flow is replaced by the conservations of kinetic plus potential energy in quasi-geostrophic flow, and the enstrophy conservation of two-dimensional flow is replaced by potential-enstrophy conservation in quasi-geostrophic flow.

Let us consider f-plane quasi-geostrophic flow in a domain that is periodic in the horizontal and unbounded in the vertical. We assume that the stratification N^2 is constant. The unboundedness in the vertical and constancy of N^2 are severe assumptions that are problematic for the ocean. Both the sea surface and the bottom boundary can have a profound impact on the flow, as does the enhancement of stratification in the thermocline. The following should thus be taken as nothing more than a first attempt to understand the properties of geostrophic turbulence in the ocean.

Under these assumptions, the dynamics can be described by

$$\frac{\partial q}{\partial t} + \mathrm{J}(\psi, q) = 0 \quad \text{with} \quad q = \frac{\partial^2 \psi}{\partial x^2} + \frac{\partial^2 \psi}{\partial y^2} + \frac{f_0^2}{N^2} \frac{\partial^2 \psi}{\partial z^2}. \tag{4.69}$$

We neglect forcing and dissipation, having in mind the dynamics in an inertial range. Energy conservation follows from multiplying this equation by $-\psi$ and integrating over the domain:

$$-\iiint \psi \frac{\partial q}{\partial t}\,\mathrm{d}^3\boldsymbol{x} = \frac{\mathrm{d}}{\mathrm{d}t}\iiint \frac{1}{2}\left[\left(\frac{\partial \psi}{\partial x}\right)^2 + \left(\frac{\partial \psi}{\partial y}\right)^2 + \frac{f_0^2}{N^2}\left(\frac{\partial \psi}{\partial z}\right)^2\right]\mathrm{d}^3\boldsymbol{x} = 0 \quad (4.70)$$

since the advective term gives no contribution. We used integration by parts, and the integrand can be identified as the sum of the kinetic and potential energies. Similarly, the conservation of potential enstrophy follows by multiplying the conservation law by q and integrating over the domain, which yields

$$\frac{\mathrm{d}}{\mathrm{d}t}\iiint \frac{q^2}{2}\,\mathrm{d}^3\boldsymbol{x} = 0. \quad (4.71)$$

This conservation of potential enstrophy plays the same role in geostrophic turbulence as the enstrophy constraint played in two-dimensional turbulence. It prevents the flow from generating stronger and stronger velocity gradients through unbounded vortex stretching. While some vortex stretching can occur in geostrophic turbulence, the restoring buoyancy forces that arise in this stratified fluid prevent stretching without bound.

The analogy to two-dimensional turbulence becomes most apparent if we define a stretched vertical coordinate:

$$z' = \frac{N}{f_0} z, \quad (4.72)$$

such that the energy density is

$$\frac{1}{2}\left[\left(\frac{\partial \psi}{\partial x}\right)^2 + \left(\frac{\partial \psi}{\partial y}\right)^2 + \left(\frac{\partial \psi}{\partial z'}\right)^2\right], \quad (4.73)$$

and the potential vorticity is

$$q = \frac{\partial^2 \psi}{\partial x^2} + \frac{\partial^2 \psi}{\partial y^2} + \frac{\partial^2 \psi}{\partial z'^2}. \quad (4.74)$$

The dynamics can now be seen to be equivalent to two-dimensional dynamics, except that the two-dimensional Laplacian in two-dimensional dynamics is replaced by a three-dimensional Laplacian (with the stretched vertical coordinate) in these quasi-geostrophic dynamics.

It is thus natural to translate our results from two-dimensional turbulence to the quasi-geostrophic case. To do so, we need to assume isotropy to extend to the vertical dimension: we assume that flow anomalies have three-dimensionally isotropic statistics in x, y, and z'. We then expect two inertial ranges, corresponding to cascades of energy and potential enstrophy. In the energy range, we expect scale interactions to transfer energy to progressively larger scales and produce an energy spectrum proportional to $k^{-5/3}$; in the enstrophy range, we expect scale interactions to transfer potential enstrophy to progressively smaller scales and an energy spectrum proportional to k^{-3}. Larger and smaller scales, per the isotropy assumption, apply to all three dimensions. For example, the inverse energy cascade implies a transfer of energy to progressively larger horizontal scales but also progressively larger vertical scales. Quasi-geostrophic flow thus has a tendency to "barotropize." The flow has a typical aspect ratio f_0/N, the "Prandtl ratio." (Note that this is the same as H/λ, with $\lambda \sim NH/f_0$ the deformation radius.)

While this picture of geostrophic turbulence can be refined substantially by taking boundaries and vertical variations in stratification into account, the general expectations set forth here can be observed in the real ocean. Satellite altimetry provides just enough spatial resolution to allow the diagnosis of an inverse cascade of kinetic energy at the sea surface (e.g. Scott and Wang, 2005; Tulloch et al., 2011). This inverse cascade is thought to be responsible for the energization of scales somewhat larger than the scale of baroclinic instability—eddies are observed to be two to three times larger than the scale of maximum growth. A $k^{-5/3}$ scaling cannot typically be discerned in the energy spectrum, however, presumably because the inertial range is too narrow.

The k^{-3} prediction for the energy spectrum in the enstrophy range, on the other hand, can be observed in the ocean thermocline. Spectra estimated from shipboard ADCP observations of thermocline velocities tend to show this scaling below the scales of the dominant eddies, typically at wavelengths between 10 and 100 km (e.g. Wang et al., 2010; Callies and Ferrari, 2013; Rocha et al., 2016). Importantly, this prediction is violated at times near the surface, where submesoscale processes can generate more energetic small scales.

Chapter 5

Submesoscale dynamics

The expectation from geostrophic turbulence that small scales do not carry much energy is partially violated near the ocean surface. Both numerical simulations and observations show substantially more energy at scales below the mesoscale deformation radius than predicted by interior geostrophic turbulence. At times, a rich field with strong submesoscale eddies and energetic frontal features can be observed. These dynamics have recently received a lot of attention, largely because they are thought to generate large vertical velocities and thus regulate the exchange of tracers, such as heat, carbon, oxygen, and nutrients, between the surface and interior ocean. In this chapter, we discuss some elements of these submesoscale dynamics in the upper ocean.

5.1 Quasi-geostrophic frontogenesis

The surface ocean often exhibits fronts, elongated zones of sharp surface buoyancy gradients. Such fronts can often be observed in satellite images of sea surface temperature, especially around the edges of mesoscale eddies and most prominently in winter. Associated with these fronts are strong geostrophic currents along the axes of the fronts and, as we will see, ageostrophic flow in the cross-frontal plane.

The theory for the generation of fronts was largely developed in the atmospheric literature, where surface fronts have a profound impact on the weather at midlatitudes. Some basic features of frontogenesis can be understood with quasi-geostrophic dynamics, as discussed by Stone (1966a). This theory successfully explains why fronts form at the surface and not in the interior of the ocean, and it explains the generation of a secondary circulation. The predicted frontogenesis is much slower than observed, however, which led Hoskins and Bretherton (1972) to develop a semi-geostrophic theory for frontogenesis. We will discuss these two theories in turn.

Fronts form if a pre-existing buoyancy gradient is sharpened by the flow field. A simple example is a straining flow acting on a buoyancy gradient in the x-direction. We can imagine this configuration to occur between mesoscale eddies arranged in a quadrupole pattern. We consider the strain rate α to be fixed and externally prescribed.

The strain field is

$$U = -\alpha x \quad \text{and} \quad V = \alpha y, \tag{5.1}$$

which is horizontally nondivergent and carries no vorticity. We let this strain field act on the zonal buoyancy field

$$b_0 = B(x) = \frac{\Delta}{2} \tanh \frac{x}{L} \quad \text{at} \quad z = 0 \quad \text{and} \quad t = 0 \tag{5.2}$$

This defines an initial buoyancy gradient around $x = 0$ that has a width L and a buoyancy difference Δ. Our goal is to derive the evolution of the buoyancy field and the flow, which can depart from the prescribed strain field. We assume that the interior of the ocean has constant stratification and no potential vorticity. For definiteness, we assume that the ocean has a depth H. The inversion relation

$$\frac{\partial^2 \psi}{\partial x^2} + \frac{f_0^2}{N^2} \frac{\partial^2 \psi}{\partial z^2} = 0 \tag{5.3}$$

then defines the interior flow and buoyancy field. The streamfunction ψ defines the departures from the imposed strain field. Here and throughout we take advantage of the invariance of the buoyancy field in y, which also implies that the flow's departure from the imposed strain field is invariant in y.

The assumption of vanishing interior potential vorticity drastically simplified the dynamics. The evolution can be fully determined from the advection of buoyancy at the surface and bottom:

$$\frac{\partial b_0}{\partial t} - \alpha x \frac{\partial b_0}{\partial x} = 0 \quad \text{for} \quad z = 0 \quad \text{and} \quad z = -H. \tag{5.4}$$

There is no departure of the flow in the cross-front direction from the imposed flow because otherwise ψ would have to be dependent on y. There is no advection in the along-front direction because there are no buoyancy gradients in that direction. What is left is the advection of the surface buoyancy field by the cross-front component of the strain field.

The surface buoyancy equation can be solved exactly. It states that the buoyancy is fixed on fluid parcels moving with the cross-front velocity $-\alpha x$. Such fluid parcels have the trajectories $x = \xi e^{-\alpha t}$ if ξ is the position at $t = 0$. Fluid parcels converge on $x = 0$ and thus sharpen the buoyancy gradient there. These trajectories motivate the coordinate transformation

$$\xi = x e^{\alpha t} \quad \text{and} \quad \tau = t. \tag{5.5}$$

At time t, ξ is the original position of a fluid parcel located at x. This definition implies that

$$\frac{\partial}{\partial x} = e^{\alpha t} \frac{\partial}{\partial \xi} \quad \text{and} \quad \frac{\partial}{\partial t} = \frac{\partial}{\partial \tau} + \alpha x e^{\alpha t} \frac{\partial}{\partial \xi}. \tag{5.6}$$

Applying these transformation rules to the buoyancy equation, we find that

$$\frac{\partial b_0}{\partial \tau} = 0 \quad \text{at} \quad z = 0. \tag{5.7}$$

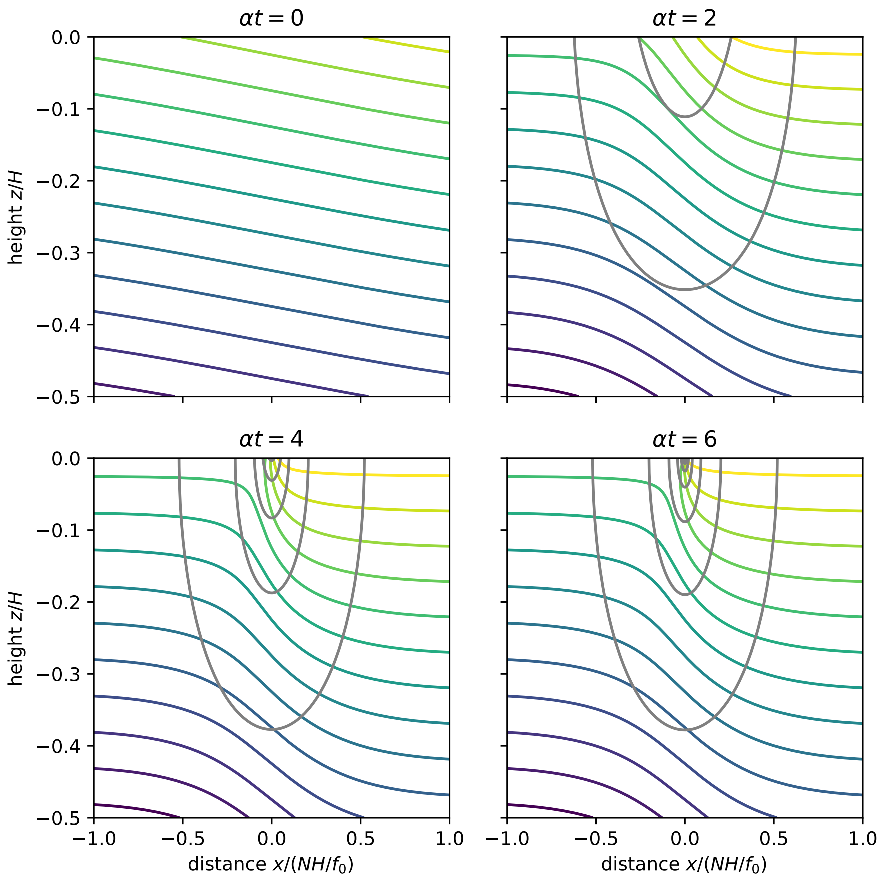

Figure 5.1: Quasi-geostrophic frontogenesis: buoyancy field (colored contours) and the along-front flow v_0 (gray contours) in the upper half of the domain.

This simply states that the buoyancy of fluid parcels traced back to their original position remains constant. We thus find the solution

$$b_0(\xi, \tau) = B(\xi) \quad \text{or} \quad b_0(x, t) = B(xe^{\alpha t}) \quad \text{at} \quad z = 0 \quad \text{and} \quad z = -H. \tag{5.8}$$

This knowledge of the surface buoyancy field can be extended into the interior using the inversion relation, which can be applied at any time t to find the interior streamfunction. The streamfunction determines the interior buoyancy field b_0 and the along-front flow v_0 (Fig. 5.1).

It can be see that while the surface buoyancy field progressively sharpens, the interior buoyancy gradients remain relatively small. The front forms at the surface. Likewise, the along-front flow is strongly enhanced at the surface: there is a sharp jet associated with the surface front, and it decays rapidly into the interior.

To understand why the buoyancy gradients sharpens exponentially at the surface but remains smaller in the interior, we consider the interior buoyancy equation:

$$\frac{\partial b_0}{\partial t} - \alpha x \frac{\partial b_0}{\partial x} + w_1 N^2 = 0. \tag{5.9}$$

The key difference is that vertical advection of the background buoyancy gradient is present here, whereas the surface boundary condition eliminates this term at $z = 0$. In the interior, the sharpening of the buoyancy gradient by the strain field can thus be opposed by the vertical advection by an ageostrophic circulation.

This ageostrophic circulation occurs in the cross-frontal plane and is called the "secondary circulation" of the front. We can diagnose it using the omega equation. It is slightly more straightforward, however, to calculate the streamfunction of the secondary circulation, defined by

$$u_1 = \frac{\partial \chi}{\partial z} \quad \text{and} \quad w_1 = -\frac{\partial \chi}{\partial x}. \tag{5.10}$$

This is possible because the y-invariance of the deviations from the strain field implies that the ageostrophic flow is nondivergent in the x–z plane. An equation for χ arises from the combination of the along-front momentum and buoyancy budgets:

$$\frac{\partial v_0}{\partial t} - \alpha x \frac{\partial v_0}{\partial x} + v_0 \alpha + f_0 \frac{\partial \chi}{\partial z} = 0, \tag{5.11}$$

$$\frac{\partial b_0}{\partial t} - \alpha x \frac{\partial b_0}{\partial x} - N^2 \frac{\partial \chi}{\partial x} = 0. \tag{5.12}$$

Applying $f_0 \partial/\partial z$ to the along-front momentum equation and $\partial/\partial x$ to the buoyancy equation and then subtracting the two equations yields

$$N^2 \frac{\partial^2 \chi}{\partial x^2} + f_0^2 \frac{\partial^2 \chi}{\partial z^2} = -2\alpha \frac{\partial b_0}{\partial x}, \tag{5.13}$$

where we made use of the thermal-wind balance

$$f_0 \frac{\partial v_0}{\partial z} = \frac{\partial b_0}{\partial x}. \tag{5.14}$$

This equation tells us that the strain α acting on a buoyancy gradient induces a secondary circulation.

If the buoyancy gradient is positive, the forcing term for χ is negative, implying a maximum in χ (Fig. 5.2). The sharpening of a positive buoyancy gradient thus induces a secondary circulation that produces downwelling on the dense side of the front and upwelling on the light side of the front. This produces a positive buoyancy tendency on the dense side and a negative buoyancy tendency on the light side, consequently acting to reduce the cross-frontal buoyancy gradient. The secondary circulation, which is an inevitable consequence of the sharpening front, thus counteracts the sharpening of buoyancy gradients in the interior. It is only at the surface, where no advection across the background stratification is possible because $w_1 = 0$, that the buoyancy gradient can sharpen into a front.

5.2 Semi-geostrophic dynamics

The failure of quasi-geostrophic dynamics to capture the rapid frontal collapse observed in midlatitude weather systems led to the search for more accurate approximations to the primitive equations that were still tractable enough for analysis. The

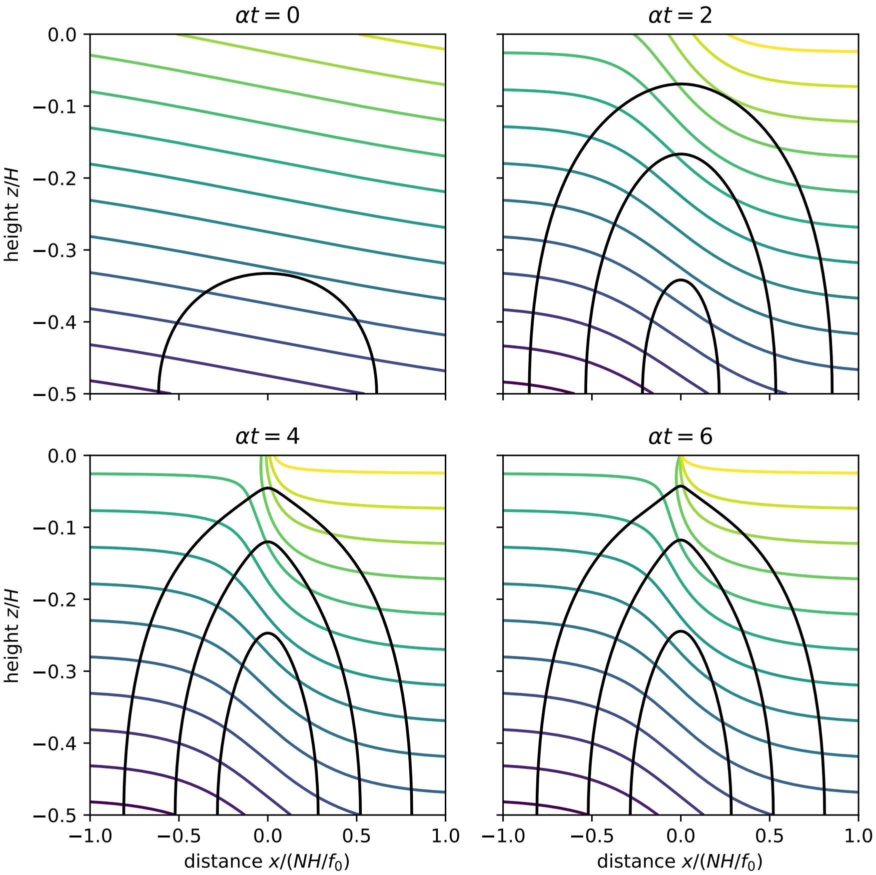

Figure 5.2: Quasi-geostrophic frontogenesis: buoyancy field (colored contours) and the secondary circulation χ (black contours) in the upper half of the domain.

semi-geostrophic equations are the result of such an approximation, and they offer an elegant generalization of the quasi-geostrophic equations that helps understand frontal dynamics.

Accelerated frontal collapse can be anticipated from the quasi-geostrophic solution discussed above. In the quasi-geostrophic approximation, we approximate the advection of momentum and buoyancy to be by the geostrophic flow only. While during frontal sharpening the momentum remains dominated by the geostrophic component, cross-frontal gradients become sharp and the products between these gradients and the cross-frontal ageostrophic flow become important. It can be anticipated that the ageostrophic secondary circulation tilts over the system, moving the surface front towards the dense side. This leaves the surface front in a region where the ageostrophic cross-frontal flow is convergent. The advection of surface buoyancy by this convergent ageostrophic flow thus adds to the external strain field, and the frontal sharpening is accelerated.

To capture this effect, we must incorporate the advection of momentum and buoyancy by the ageostrophic flow. The semi-geostrophic equations do just that, while still approximating the momentum by the geostrophic component. This approximation is useful because it leaves the system balanced: the dynamics can be described in terms of conservation of potential vorticity and an inversion statement that allows determination of the flow from the distribution of potential vorticity. We will see that his has conceptual advantages that help us understand frontal dynamics. It also simplifies the dynamics by filtering out inertia–gravity waves.

We begin with the primitive equations, i.e., the Boussinesq equations with the hydrostatic approximation:

$$\frac{\mathrm{D}u}{\mathrm{D}t} - f v = -\frac{\partial \phi}{\partial x}, \tag{5.15}$$

$$\frac{\mathrm{D}v}{\mathrm{D}t} + f u = -\frac{\partial \phi}{\partial y}, \tag{5.16}$$

$$b = \frac{\partial \phi}{\partial z}, \tag{5.17}$$

$$\frac{\partial u}{\partial x} + \frac{\partial v}{\partial y} + \frac{\partial w}{\partial z} = 0, \tag{5.18}$$

$$\frac{\mathrm{D}b}{\mathrm{D}t} = 0, \tag{5.19}$$

where $\phi = p/\rho_0$. Defining the geostrophic velocities as

$$u_{\mathrm{g}} = -\frac{1}{f}\frac{\partial \phi}{\partial y} \quad \text{and} \quad v_{\mathrm{g}} = \frac{1}{f}\frac{\partial \phi}{\partial x}, \tag{5.20}$$

We can write the horizontal momentum equations as

$$\frac{\mathrm{D}u}{\mathrm{D}t} - f(v - v_{\mathrm{g}}) = 0 \quad \text{and} \quad \frac{\mathrm{D}v}{\mathrm{D}t} + f(u - u_{\mathrm{g}}) = 0. \tag{5.21}$$

Defining the operator

$$\mathscr{D} = \frac{1}{f}\frac{\mathrm{D}}{\mathrm{D}t}, \tag{5.22}$$

we can write these equations as

$$u = u_{\mathrm{g}} - \mathscr{D}v = u_{\mathrm{g}} - \mathscr{D}v_{\mathrm{g}} - \mathscr{D}^2 u \quad \text{and} \quad v = v_{\mathrm{g}} + \mathscr{D}u = v_{\mathrm{g}} + \mathscr{D}u_{\mathrm{g}} - \mathscr{D}^2 v. \tag{5.23}$$

The approximation leading to the semi-geostrophic equations consists of neglecting the last terms in these equations. This is justified if

$$\mathscr{D}^2 u \ll u \quad \text{and} \quad \mathscr{D}^2 v \ll v. \tag{5.24}$$

This is a statement that the momentum is to leading order geostrophic, while it makes no assumption about the relative contributions geostrophic and ageostrophic flows make to advection. Crucially, the approximation neglects the second derivative compared with the same component of velocity. It is thus possible that $\mathscr{D}^2 v \gg u$, as will indeed be the case in the example of frontogenesis we discuss below. The notion that the along-front velocity is in geostrophic balance while the cross-front ageostrophic flow is fully taken into account has led to the name "semi-geostrophic" equations, although the approximation is more appropriately called the "geostrophic-momentum approximation."

The resulting equations of motion are then

$$\frac{\mathrm{D}u_\mathrm{g}}{\mathrm{D}t} - fv = -\frac{\partial \phi}{\partial x}, \tag{5.25}$$

$$\frac{\mathrm{D}v_\mathrm{g}}{\mathrm{D}t} + fu = -\frac{\partial \phi}{\partial y}, \tag{5.26}$$

$$b = \frac{\partial \phi}{\partial z}, \tag{5.27}$$

$$\frac{\partial u}{\partial x} + \frac{\partial v}{\partial y} + \frac{\partial w}{\partial z} = 0, \tag{5.28}$$

$$\frac{\mathrm{D}b}{\mathrm{D}t} = 0, \tag{5.29}$$

where the advection is by the full three-dimensional flow. While the approximation might appear mild, the simplification it affords is spectacular. The full power of the approximation becomes apparent when making the following coordinate transformation:

$$X = x + \frac{v_\mathrm{g}}{f}, \qquad Y = y - \frac{u_\mathrm{g}}{f}, \qquad Z = z, \qquad T = t. \tag{5.30}$$

Since

$$\frac{\mathrm{D}X}{\mathrm{D}t} = u + \frac{1}{f}\frac{\mathrm{D}v_\mathrm{g}}{\mathrm{D}t} = u_\mathrm{g} \quad \text{and} \quad \frac{\mathrm{D}Y}{\mathrm{D}t} = v - \frac{1}{f}\frac{\mathrm{D}u_\mathrm{g}}{\mathrm{D}t} = v_\mathrm{g}, \tag{5.31}$$

these new coordinates are referred to as "geostrophic coordinates." In these coordinates, the horizontal motion of fluid parcels is determined by the geostrophic rather than the full velocities. This means that the advection operator can be written as

$$\frac{\mathrm{D}}{\mathrm{D}t} = \frac{\partial}{\partial T} + u_\mathrm{g}\frac{\partial}{\partial X} + v_\mathrm{g}\frac{\partial}{\partial Y} + w\frac{\partial}{\partial Z}, \tag{5.32}$$

where the geostrophic velocities velocities appear in the horizontal advection terms. On horizontal boundaries, where $w = 0$, the buoyancy conservation thus reduces to

$$\frac{\partial b}{\partial T} + u_\mathrm{g}\frac{\partial b}{\partial X} + v_\mathrm{g}\frac{\partial b}{\partial Y} = 0. \tag{5.33}$$

In the transformed coordinates, buoyancy at the boundary is conserved under geostrophic advection, just like in the quasi-geostrophic system, where the same applies in the untransformed coordinates.

We specialize our further discussion to a system that is invariant in the y-direction. This simplifies the algebra, but it should be noted that a generalization to three dimensions is available (Hoskins, 1975). The conceptual power of the semi-geostrophic system is based on the conservation of potential vorticity. It can be verified with straightforward algebra that in the two-dimensional system

$$\frac{\mathrm{D}q_g}{\mathrm{D}t} = 0 \quad \text{with} \quad q_g = \left(f + \frac{\partial v_g}{\partial x}\right)\frac{\partial b}{\partial z} - \frac{\partial v_g}{\partial z}\frac{\partial b}{\partial x}. \tag{5.34}$$

Since the geostrophic velocity appears in this expression, q_g is called the "geostrophic potential vorticity." Applying the transformation rules

$$\frac{\partial}{\partial x} = \frac{1}{f}\left(f + \frac{\partial v_g}{\partial x}\right)\frac{\partial}{\partial X}, \qquad \frac{\partial}{\partial z} = \frac{\partial}{\partial Z} + \frac{1}{f}\frac{\partial v_g}{\partial z}\frac{\partial}{\partial X}, \tag{5.35}$$

we can reduce the geostrophic potential vorticity to

$$q_g = \left(f + \frac{\partial v_g}{\partial x}\right)\left(\frac{\partial b}{\partial Z} + \frac{1}{f}\frac{\partial v_g}{\partial z}\frac{\partial b}{\partial X}\right) - \frac{1}{f}\frac{\partial v_g}{\partial z}\left(f + \frac{\partial v_g}{\partial x}\right)\frac{\partial b}{\partial X} = \left(f + \frac{\partial v_g}{\partial x}\right)\frac{\partial b}{\partial Z}. \tag{5.36}$$

Further noting that

$$\frac{\partial v_g}{\partial x} = \frac{1}{f}\left(f + \frac{\partial v_g}{\partial x}\right)\frac{\partial v_g}{\partial X}, \quad \text{so} \quad \left(f + \frac{\partial v_g}{\partial x}\right)\left(1 - \frac{1}{f}\frac{\partial v_g}{\partial X}\right) = f, \tag{5.37}$$

we find that

$$q_g\left(1 - \frac{1}{f}\frac{\partial v_g}{\partial X}\right) = f\frac{\partial b}{\partial Z}. \tag{5.38}$$

If we now define

$$\Phi = \phi + \frac{v_g^2}{2}, \tag{5.39}$$

we have

$$f v_g = \frac{\partial \phi}{\partial x} = \frac{\partial \Phi}{\partial X} \quad \text{and} \quad b = \frac{\partial \phi}{\partial z} = \frac{\partial \Phi}{\partial Z}, \tag{5.40}$$

which can be verified using the transformation rules. Using these in (5.38), we find that

$$\frac{1}{f^2}\frac{\partial^2 \Phi}{\partial X^2} + \frac{f}{q_g}\frac{\partial^2 \Phi}{\partial Z^2} = 1. \tag{5.41}$$

This is the balance statement of semi-geostrophic dynamics. It allows for the inversion for Φ from a given field of geostrophic potential vorticity as long as $q_g/f > 0$ everywhere. Under this condition, the equation is elliptic and can be solved given appropriate boundary conditions. Like in quasi-geostrophic dynamics, the existence of the balance statement allows us to think of the dynamics as consisting of potential-vorticity conservation and an inversion for the flow based on this balance statement.

The balance statement (5.41) of the semi-geostrophic system in geostrophic coordinates has a remarkable similarity to that of the quasi-geostrophic system. This correspondence becomes exact if we assume the flow to have uniform geostrophic potential vorticity:

$$q_g = f N^2. \tag{5.42}$$

The conservation of geostrophic potential vorticity implies that if q_{g} assumes this uniform value initially, it must remain at this value for all times. Splitting the buoyancy field into a background and a perturbation, i.e.,

$$\Phi = \frac{1}{2}N^2 z^2 + \Phi', \tag{5.43}$$

then turns the balance statement into

$$\frac{\partial^2 \Phi'}{\partial X^2} + \frac{f^2}{N^2}\frac{\partial^2 \Phi'}{\partial Z^2} = 0. \tag{5.44}$$

This is exactly the same equation for $\Phi'(X, Z)$ as we had in the quasi-geostrophic system for $\psi(x, z)$, see (5.3). In combination with the buoyancy boundary condition (5.33), this tells us that the evolution of the semi-geostrophic system in geostrophic coordinates is exactly equivalent to the evolution of the quasi-geostrophic system in physical space. The fields predicted by the semi-geostrophic system can thus be obtained simply by applying a coordinate transformation to the quasi-geostrophic solution.

5.3 Semi-geostrophic frontogenesis

Applied to the concrete example of strain-induced frontogenesis, the above procedure produces a semi-geostrophic solution that is a mere distortion of the quasi-geostrophic one. The perturbation buoyancy field at boundaries is, in geostrophic coordinates,

$$b'(X, T) = B(X e^{\alpha T}) \quad \text{at} \quad z = 0 \quad \text{and} \quad z = -H. \tag{5.45}$$

This provides the boundary conditions for the inversion (5.44), which yields Φ', from which the flow can be determined. In particular, we can determine the geostrophic along-front flow

$$v_{\mathrm{g}} = \frac{1}{f}\frac{\partial \Phi'}{\partial x}, \tag{5.46}$$

which is a strengthening jet concentrated at the sharpening buoyancy gradient. Using this geostrophic velocity, we can then transform the solution to physical space:

$$x = X - \frac{v_{\mathrm{g}}}{f}. \tag{5.47}$$

Since $v_{\mathrm{g}} > 0$ at the surface, this transformation implies a shift of the surface front towards the dense side of the front relative to the quasi-geostrophic solution (Fig. 5.3, 5.4). And because v_{g} is largest at the core of the front, the transformation compresses the dense side of the front and stretches the light side of the front. This accelerates the sharpening of the buoyancy gradient and leads to the formation of a buoyancy discontinuity in finite time. In the example shown in the figures, this occurs at about $\alpha t = 0.35$. (The solution procedure can be applied after the formation of a discontinuity, but the transformation leaves the solution multivalued.)

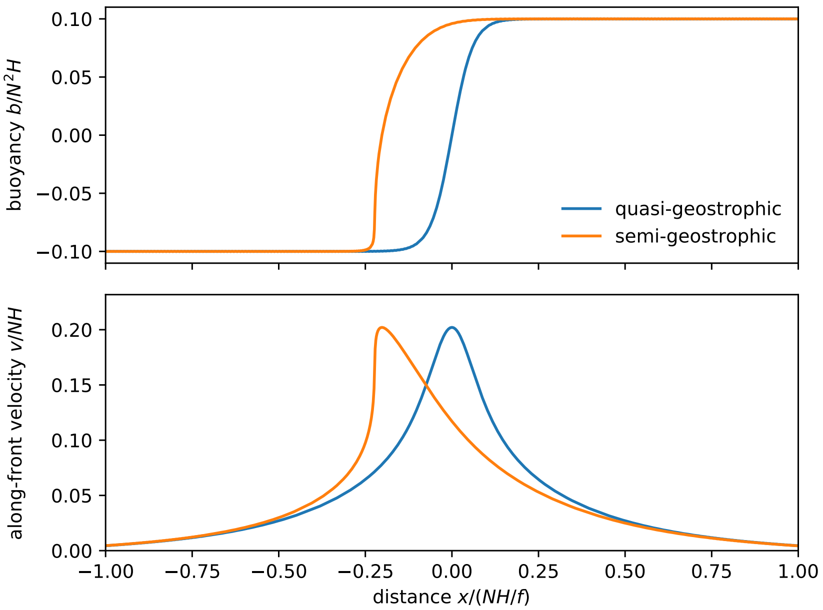

Figure 5.3: Comparison between quasi-geostrophic and semi-geostrophic frontogenesis. Shown are the surface buoyancy and along-front geostrophic velocity at time $\alpha t = 3.5$, which is just before frontal collapse in the semi-geostrophic system. The semi-geostrophic fields are a distorted versions of the quasi-geostrophic fields.

Semi-geostrophic dynamics produce a markedly asymmetric surface front, which is sharper on the dense side. Associated with this asymmetry is a skewness in the relative vorticity: the cyclonic vorticity on the dense side is much larger than the anticyclonic vorticity on the light side of the front. Such skewness in relative vorticity has been observed in the upper ocean in a number of regions, and it contrasts with more symmetric vorticity statistics in the ocean interior (Rudnick, 2001; Shcherbina et al., 2013; Buckingham et al., 2016). It is expected more generally than in this frontogenesis example because

$$\frac{\partial v_g}{\partial x} = \frac{f \frac{\partial v_g}{\partial X}}{f - \frac{\partial v_g}{\partial X}}. \tag{5.48}$$

Positive vorticity anomalies in geostrophic coordinates are enhanced by the transformation to physical space, while negative anomalies are suppressed. It generates the following mapping of vorticity anomalies from geostrophic to physical coordinates: $-\infty \mapsto -f$, $-f \mapsto -f/2$, $f/2 \mapsto f$, and $f \mapsto \infty$.

Through the transformation of coordinates, semi-geostrophic theory captures the acceleration of frontogenesis by the secondary circulation. The advection by the ageostrophic flow, which slumps the surface front over to the dense side and adds to the cross-frontal convergence of the strain field, is elegantly wrapped into a simple remapping of the quasi-geostrophic solution. This remapping provides important insight into the formation of fronts, but it also generates some confidence that quasi-geostrophic

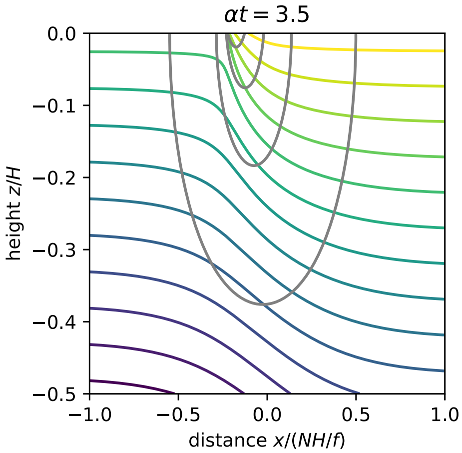

Figure 5.4: Buoyancy field and along-front geostrophic flow just before frontal collapse, as predicted by the semi-geostrophic system. Note the distortion towards the dense side of the front compared to the quasi-geostrophic prediction.

solutions are not far off the truth, even when quasi-geostrophic scaling is formally violated.

5.4 Mixed-layer instabilities

The tendency for frontogenesis to occur at the sea surface is one difference between the upper ocean and the interior. But there is another feature of the upper ocean that is key for submesoscale dynamics in the upper ocean: the mixed layer. This is the ocean's surface boundary layer that is mixed by directly forced small-scale turbulence. Both wind stress and surface cooling destabilize the upper ocean and generate a mixed layer. Since the atmospheric forcing is seasonal, with typically strong winds and cooling in winter and weaker winds and warming in summer, the mixed layer also displays marked seasonality. It is typically much deeper in winter than in summer. The deepest winter mixed layers in the midlatitude ocean can reach several hundred meters, whereas summer mixed layers are often less than ten meters thick.

These mixed layers have a profound impact on the balanced dynamics in the upper ocean. The sharp increase in stratification at the base of the mixed layer can act much like a rigid bottom to motion within the mixed layer. In the presence of a lateral buoyancy gradient, for example at the edges of mesoscale eddies, this allows for a baroclinic instability within the mixed layer that arises from Eady edge waves propagating at the sea surface and the interface between the mixed layer and the thermocline.

Let us construct a simple quasi-geostrophic model of this instability (Callies et al., 2016), treating the thermocline more realistically not as a rigid bottom but a layer with strong stratification. We model the mixed layer as having a constant stratification N_m and the thermocline as having a constant stratification N_t. The mixed-layer depth is h.

To focus on the mixed-layer dynamics, we assume the thermocline is infinitely deep, and we impose decay conditions at depth. We consider a buoyancy gradient in the y-direction that is in thermal-wind balance with a mean flow in the x-direction. In the mixed layer, we assume the mean flow to be $U = \Lambda_\mathrm{m}(z+h)$, and in the thermocline, we assume it to be $U = \Lambda_\mathrm{t}(z+h)$, allowing for different buoyancy gradients in the mixed layer and thermocline. The linear shear ensures that there are no potential-vorticity gradients within the mixed layer and thermocline, such that the quasi-geostrophic potential vorticity within the two layers can be set to zero at all times. We assume that f is constant, appropriate for submesoscale dynamics.

With these assumptions, the dynamics are controlled by the advection of conserved quantities at the surface and at the interface. At the surface, as usual, buoyancy is conserved under horizontal advection. It will turn out convenient to define $\theta_0 = -f\,b_0/N_\mathrm{m}^2$ at $z=0$ and $\Gamma_0 = f^2\Lambda_\mathrm{m}/N_\mathrm{m}^2$, such that the linearized conservation of surface buoyancy can be written as

$$\frac{\partial \theta_0}{\partial t} + \Lambda_\mathrm{m} h \frac{\partial \theta_0}{\partial x} + \Gamma_0 \frac{\partial \psi}{\partial x} = 0 \quad \text{at} \quad z = 0. \tag{5.49}$$

The second and third term represent advection of the θ_0 perturbation by the mean flow $\Lambda_\mathrm{m} h$ at $z=0$ and the advection of the background θ_0 gradient by the perturbation flow. The interface between the mixed layer and the thermocline can be treated similarly, but it is slightly more complicated because the interface can move, such that $w_1 \neq 0$ at $z=-h$. To arrive at a similar conservation law, we consider the buoyancy budgets just above and just below the interface:

$$\frac{\partial b_0^+}{\partial t} - f\Lambda_\mathrm{m}\frac{\partial \psi}{\partial x} + w_1 N_\mathrm{m}^2 = 0 \quad \text{and} \quad \frac{\partial b_0^-}{\partial t} - f\Lambda_\mathrm{t}\frac{\partial \psi}{\partial x} + w_1 N_\mathrm{t}^2 = 0, \tag{5.50}$$

where $b_0^\pm$ denotes the buoyancy anomaly just above or below the interface. There is no advection by the mean flow because it vanishes at $z=-h$. We now apply two matching conditions at the interface. First, we require that pressure is continuous at the interface, which implies that ψ must be continuous. Second, we require that the interface is a material surface. Since the continuity in pressure implies that the horizontal velocities above and below the interface match, this condition requires that w_1 is equal above and below the interface. We can thus rearrange (5.50) into

$$\frac{\partial \theta_1}{\partial t} + \Gamma_1 \frac{\partial \psi}{\partial x} = 0 \quad \text{at} \quad z = -h, \tag{5.51}$$

where

$$\theta_1 = f\left(\frac{b_0^+}{N_\mathrm{m}^2} - \frac{b_0^-}{N_\mathrm{t}^2}\right) \quad \text{and} \quad \Gamma_1 = -f^2\left(\frac{\Lambda_\mathrm{m}}{N_\mathrm{m}^2} - \frac{\Lambda_\mathrm{t}}{N_\mathrm{t}^2}\right). \tag{5.52}$$

Note that the conserved quantity θ_1 is nothing but the potential vorticity integrated just across the interface, such that the only contribution arises from the stretching term. Similarly, θ_0 can be thought of as the potential vorticity integrated across the sea surface, and Γ_0 and Γ_1 are the gradients of potential vorticity in infinitely thin sheets at the surface and the interface between the mixed layer and the thermocline.

The mixed-layer instability can now be anticipated to occur as long as Γ_0 and Γ_1 have opposite signs. This allows edge waves to counter-propagate on the surface and interface, phase lock, and mutually amplify. This is typically satisfied because $N_\mathrm{m} \ll N_\mathrm{t}$ and $\Lambda_\mathrm{m} \sim \Lambda_\mathrm{t}$. The mixed layer stratification is weak, and the buoyancy gradients are similar in the two layers. Using a wave ansatz together with the inversion statements

$$\frac{\partial^2\psi}{\partial x^2} + \frac{\partial^2\psi}{\partial y^2} + \frac{f^2}{N_\mathrm{m}^2}\frac{\partial^2\psi}{\partial z^2} = 0 \quad \text{and} \quad \frac{\partial^2\psi}{\partial x^2} + \frac{\partial^2\psi}{\partial y^2} + \frac{f^2}{N_\mathrm{t}^2}\frac{\partial^2\psi}{\partial z^2} = 0 \tag{5.53}$$

in the mixed layer and thermocline, respectively, we can solve the linear stability completely. In the case $\Lambda = \Lambda_\mathrm{m} = \Lambda_\mathrm{t}$, the zonal phase speed is

$$c = \frac{\Lambda h}{2}\left(1 - \frac{\alpha}{\mu}\right) \pm \frac{i\Lambda h}{\mu}\sqrt{\frac{(1-\alpha^2)(\mu - \tanh\mu)}{\tanh\mu + \alpha} - \frac{1}{4}(\mu-\alpha)^2}, \tag{5.54}$$

where

$$\mu = \frac{N\kappa h}{f} \quad \text{and} \quad \alpha = \frac{N_\mathrm{m}}{N_\mathrm{t}}, \tag{5.55}$$

with the horizontal wavenumber magnitude $\kappa = \sqrt{k^2 + l^2}$. This reverts to the solution to the Eady model as $\alpha \to 0$ for fixed μ, as expected because then the thermocline acts like a rigid bottom. In reality $\alpha > 0$, which modifies the instability because modes can now penetrate into the thermocline. Nevertheless, for realistically small α, the most unstable mode occurs around the deformation radius of the mixed layer $N_\mathrm{m} h/f$. This mixed-layer deformation is substantially smaller than the thermocline deformation radius, both because the stratification in the mixed layer is weaker, and the vertical scales h is smaller than the thickness of the thermocline. This makes this instability a submesoscale instability, occurring at scales between 100 m and 10 km. The growth rate of the instability similarly scales with the Eady growth rate $f\Lambda/N_\mathrm{m}$. Since the mixed-layer stratification is weaker than the thermocline stratification, mixed-layer instabilities grow much more rapidly, often with a time scale of about a day. Unlike the Eady model, mixed-layer instabilities have a long-wave cutoff. At large scales, the dynamics split into two neutral waves, one that is baroclinic in the mixed layer and one that is barotropic in the mixed layer, and both decay exponentially into the thermocline like edge waves.

These mixed-layer baroclinic instabilities appear to be the primary source of submesoscale turbulence (Callies et al., 2015). Both numerical simulations and observations show that submesoscale turbulence is much more energetic in winter than in summer, as is expected from the pronounced seasonal cycle of the mixed layer itself. In winter, when atmospheric forcing is strong, deep mixed layers harbor large amounts of potential energy that can be release by these instabilities. The vertical structure of submesoscale turbulence is also consistent with this mechanism: it is strongest within the mixed layer and rapidly decays below its base.

The quasi-geostrophic model described above misses some features of baroclinic mixed-layer instabilities. The quasi-geostrophic scaling requires that the Richardson number of the mixed layer, $\mathrm{Ri} = N_\mathrm{m}^2/\Lambda_\mathrm{m}^2$, is much larger than one. This is often violated, and non-quasi-geostrophic dynamics must be considered. A generalization of the

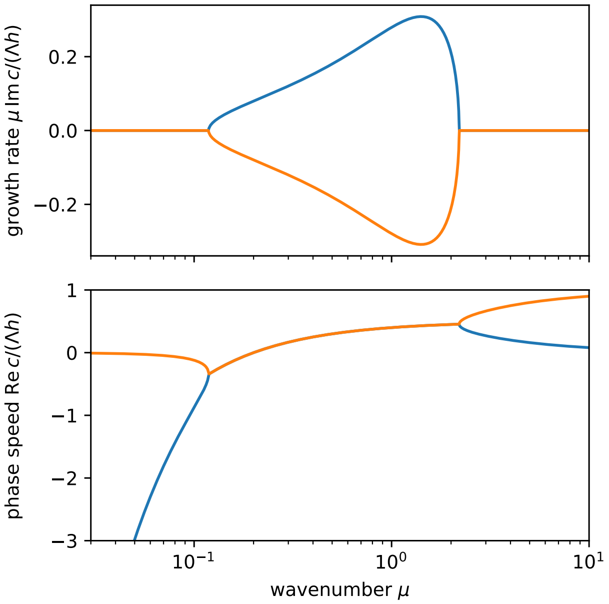

Figure 5.5: Growth rate and phase speed of a baroclinically unstable mixed layer model. The dispersion relation (5.54) is shown for $\alpha = 0.2$.

quasi-geostrophic Eady model (Stone, 1966b) predicts that the most unstable mode occurs at a wavenumber

$$k = 1.6\sqrt{\frac{\mathrm{Ri}}{\mathrm{Ri}+1}\frac{f}{N_\mathrm{m}h}}, \tag{5.56}$$

with a growth rate

$$\sigma = 0.3\sqrt{\frac{\mathrm{Ri}}{\mathrm{Ri}+1}\frac{f\Lambda_\mathrm{m}}{N_\mathrm{m}}}. \tag{5.57}$$

For $\mathrm{Ri} \sim 1$, this reduces the scale of the most unstable mode and its growth rate compared to the quasi-geostrophic prediction. Furthermore, the quasi-geostrophic dynamics will be modified by accelerated frontogenesis. As we have seen, these semi-geostrophic corrections are important to explain the observed fronts and the skewness of the vorticity statistics. The increased ubiquity of fronts in winter suggest that submesoscale frontogenesis is often initiated by mixed-layer instabilities.

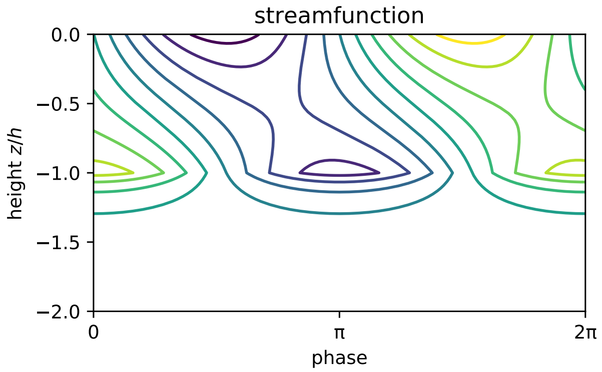

Figure 5.6: Structure of the most unstable mixed-layer instability mode, shown for $\alpha = 0.2$. Note the familiar tilt into the mean shear and the less familiar up–down asymmetry and penetration into the thermocline. The mixed-layer base is at $z/h = -1$.

Chapter 6

Deep-ocean circulation

6.1 Historical overview and concepts

So far, we have focused our attention on the upper ocean: the large- and mesoscale circulation of the thermocline and the submesoscale circulation of the surface ocean. The majority of the ocean's volume, however, is made up by the waters below the thermocline. This deep ocean is filled with cold polar waters, as first recorded in a letter the British slave trader Henry Ellis wrote to Stephen Hales in 1751:

> [. . .] I made several trials with the bucket sea-gage, in latitude 25'–13" north; longitude 25'–12" west. I charged it and let it down to different depths, from 360 feet to 5346 feet; when I discovered [. . .] that the cold increased regularly, in proportion to the depths, till it descended to 3900 feet: from whence the mercury in the thermometer came up at 53 degrees; and tho' I afterwards sunk it to the depth of 5346 feet, [. . .] it came up no lower.

Clearly, Ellis had discovered the base of the thermocline, below which the ocean is filled with the polar waters at high latitudes. This deep ocean is now understood to be a vast reservoir of heat and carbon that plays an important regulatory role in the earth's climate, especially on centennial to millennial time scales. For example, the deep ocean is thought o have stored the equivalent of 100 ppm of atmospheric CO_2 during the last glacial maximum. How exactly this was accomplished is a matter of an ongoing debate, but it seems clear that it was a combination of a colder ocean being able to hold more carbon and a change in circulation and stratification.

The presence of polar waters at 25°N and 25°W did not appear to strike Ellis as a fundamental discovery:

> This experiment, which seem'd at first but mere food for curiosity, became in the interim very useful to us. By its means we supplied our cold bath, and cooled our wines or water at pleasure; which is vastly agreeable to us in this burning climate.

His observations did not attract much attention at the time, but they were eventually interpreted correctly by Count Rumford and Alexander von Humboldt, who recognized the polar origin of the deep cold water. In 1845, these ideas lead Emil Lenz (of "Lenz's law" fame) to develop a more specific theory of the deep-ocean circulation. He envisioned hemispheric overturning cells that consisted of sinking at the poles and upwelling at the equator, citing the upward bulging of the equatorial thermocline as evidence. This conception of the deep-ocean circulation would dominate the thinking well into the twentieth century.

It was not until the 1925–1927 Meteor expedition, led by Merz and Wüst, amassed hydrographic samples from across the Atlantic that Lenz's theory was refuted. (Merz passed away during the expedition in Buenos Aires.) Using Meteor observations of temperature, salinity, and oxygen concentration, Wüst showed that waters originating in the northern North Atlantic spread south across the Equator and into the Southern Ocean at mid-depth, while southern-source waters spread northward along the ocean bottom. It is now known that these deep and bottom waters are formed in the Nordic and Labrador Seas in the north and in the Weddell and Ross Seas in the south. In these regions, strong buoyancy forcing—heat loss to the atmosphere and the rejection of brine when sea ice forms—and a pre-existing weak stratification allows surface waters to become dense enough to sink all the way to the deep ocean. There is no such deep convection in the North Pacific, proximately because the Pacific is less salty than the Atlantic, but ultimately for reasons that are not fully understood (e.g., Ferreira et al., 2018).

Wüst carefully wrote about "spreading," not "flow," of water, when rationalizing the property distribution of the deep ocean because he knew there were dynamical constraints on the deep-ocean circulation that meant that widespread southward flow was unlikely. How strong these dynamical constraints were, however, did not become fully apparent until Stommel et al. (1958) and Stommel and Arons (1959a,b) pointed them out in a set of papers that have become a touchstone of our understanding of the deep-ocean circulation. They considered a simple homogeneous deep ocean that has a flat bottom. To this deep ocean, water is added by a point source at high latitudes, and water leaves the deep ocean through prescribed uniform upwelling w_0, which they imagined pulls water into the thermocline. On a β-plane and under planetary-geostrophic scaling, certainly appropriate for the sluggish large-scale circulation of the deep ocean, the flow must satisfy the linear vorticity balance

$$\beta v = f \frac{\partial w}{\partial z}. \tag{6.1}$$

Integrated over the depth of the deep ocean, this yields

$$\beta V = f w_0, \tag{6.2}$$

where V is the vertically integrated meridional flow. This tells us that the upwelling out of the deep ocean drives poleward flow, similar to how Ekman suction drives poleward flow in the thermocline. In the context of this idealized deep ocean, however, this seems somewhat surprising: the flow is directed towards the source! The conundrum is resolved by appealing the western boundary currents, which must carry the source water plus the interior transport southward. The circulation is closed by zonal currents that can be obtained from the continuity equation:

$$\frac{\partial U}{\partial x}+\frac{\partial V}{\partial y}+w_0=0, \quad \text{so} \quad U=2w_0(L-x) \tag{6.3}$$

if we assume a β-plane and the ocean basin to extend from $x = 0$ to $x = L$. (More complicated geometries are easily dealt with.)

While the interior flows in the deep ocean are more complicated than in the Stommel–Arons theory, largely because upwelling out of the deep ocean is far from uniform and topography plays an important role, deep western boundary currents are a ubiquitous and important feature of the deep-ocean circulation. These deep boundary currents were first observed with floats in the 1950s and are often cited as a glorious experimental confirmation of Stommel and Aron's prediction. (Usually ocean theories are constructed only after observations demand an explanation.) Most of the meridional property spreading that Wüst described thus occurs in deep western boundary currents, from the properties enter the interior ocean through zonal flow and the stirring by mesoscale eddies.

The next major contribution to the understanding of the deep-ocean circulation was provided by Walter Munk. Munk (1966), in a classic paper titled "Abyssal recipes" said: if the cold water formed at the poles is to upwell into the thermocline, it has to cross buoyancy surfaces. And in order to cross density surfaces, the water must gain buoyancy through a non-conservative mixing process. In steady state, the buoyancy budget is

$$\boldsymbol{u}\cdot\nabla b=\nabla\cdot(\kappa\nabla b), \tag{6.4}$$

which expresses this balance between the advection of flow across buoyancy surfaces and mixing represented by a diffusivity κ. Buoyancy surfaces are relatively flat in the deep ocean, so this balance is dominated by the vertical component:

$$w\frac{\partial b}{\partial z}=\frac{\partial}{\partial z}\left(\kappa\frac{\partial b}{\partial z}\right). \tag{6.5}$$

If now w and κ are constants and boundaries are ignored, a solution to this equation is

$$b=b_0e^{\frac{wz}{\kappa}}, \tag{6.6}$$

so the buoyancy profile has a decay scale $d=\kappa/w$. Having an estimate of bottom-water inflow into the Pacific and assuming upwelling is uniform gives about $w = 10^{-7}$ m s^{-1}. Together with the observed buoyancy profile having a decay scale of about $d = 1000$ m, this upwelling requires a diffusivity of about $\kappa = 10^{-4}$ m^2 s^{-1}. This value is two orders of magnitude larger than the molecular diffusivity of seawater, suggesting the upwelling of deep water across buoyancy surfaces requires turbulent mixing.

Munk's abyssal recipes stimulated a decades-long quest to observe the turbulence required to close the circulation of the deep ocean. Two methods were developed:

1. Microstructure profilers directly measure the shear of the centimeter-scale turbulence, and one can infer the turbulent dissipation rate ε using Kolmogorov's turbulence theory. This dissipation rate is then empirically related to the turbulent diffusivity κ.

2. In tracer release experiments, tracer is injected into the deep ocean at a particular depth, and it is subsequently sampled to track the rate at which it spreads across buoyancy surfaces. The rate of tracer spreading can be related directly to the turbulent diffusivity κ.

Both these estimates give a diffusivity of about $\kappa = 10^{-5}\ \mathrm{m}^2\ \mathrm{s}^{-1}$ in much of the interior ocean, an order of magnitude smaller than what Munk had inferred to be required for diffusive upwelling into the thermocline. The notion of "missing mixing" arose.

It turns out, however, that not all deep water must upwell across buoyancy surface into the thermocline. Advances in the understanding of the Southern Ocean led to the realization that North Atlantic Deep Water, the water formed in the northern North Atlantic and spreading southward at mid-depth, can come back up to the surface adiabatically along sloping isopycnals in the Southern Ocean. There, a slight imbalance between the Eulerian-mean circulation and the eddy-induced circulation results in a residual circulation that is directed largely along isopycnals. This allows the so-called "upper cell" of the deep-ocean circulation to close largely adiabatically.

There still is a need for mixing to allow for the upwelling of Antarctic Bottom Water, the southern-source water that spreads northward along the ocean bottom. It has become increasingly clear that this bottom water experiences plenty of mixing, because it is close to topography. Microstructure and tracer observations show that while interior mixing is weak, mixing is enhanced by orders of magnitude over rough bathymetry (Polzin et al., 1997; Ledwell et al., 2000). There appears to be "enough" mixing to close the circulation in a Munk sense, but the spatial heterogeneity of the mixing pose challenges to our understanding of the abyssal circulation. It certainly is not as simple as Stommel and Arons envisioned.

6.2 Tides

The topic of tides is somewhat misplaced in this section, given that tidal motion occurs throughout the water column. But a large fraction of the current interest in tides relates to the circulation of the deep ocean through their role in generating small-scale mixing. Tidal motion is thought to be a major contributor to generating the turbulence that lightens Antarctic Bottom Waters and allows it to upwell to mid-depth. When tidal flow encounters topography, it generates internal waves that in turn break and generate the small-scale turbulence that mixes heat down into the abyss.

The theory of tides had largely been worked out in the nineteenth century, and tidal predictions had become extremely accurate in the early twentieth century, to the point that the subject had become scientifically boring. In the 1990s, however, interest in tides was revived by the realization of their importance for the circulation of the deep ocean, and this renewed interest continues until today.

Our discussion of tides consists of two parts. We will discuss first the generation of tides by the perturbations to the earth's gravitational potential by the sun and the moon and second the hydrodynamic response of the ocean to that forcing.

Tides are generated by the spatial variations in the gravitational forces that the sun and the moon exert on the ocean. Other celestial bodies also perturb the earth's gravitational field, but these perturbations are tiny compared to those induced by the sun and the moon. Let us derive an expression for this perturbation using the sun as an example. Consider an observer somewhere on the surface of the earth. The gravitational potential this observer experiences depends on the distance r_S between the observer and the sun:

$$V_\mathrm{S} = -\frac{GM_\mathrm{S}}{r_\mathrm{S}}, \tag{6.7}$$

where G is the gravitational constant and M_S is the solar mass. If we now call a the radius of the earth, R_S the distance between the centers of the earth and the sun, and α the angle between the vectors pointing from the center of the earth to the observer and to the sun, the sun's gravitational potential can be written as

$$V_\mathrm{S} = -\frac{GM_\mathrm{S}}{R_\mathrm{S}}\left(1+\frac{a^2}{R_\mathrm{S}^2}-2\frac{a}{R_\mathrm{S}}\cos\alpha\right)^{-\frac{1}{2}} = -\frac{GM_\mathrm{S}}{R_\mathrm{S}}\sum_{n=0}^{\infty}\left(\frac{a}{R_\mathrm{S}}\right)^n P_n(\cos\alpha). \tag{6.8}$$

In the first step, we used the law of cosines, which implies $r_\mathrm{S}^2 = R_\mathrm{S}^2 + a^2 - 2R_\mathrm{S}a\cos\alpha$. In the second step, the inverse square root was expanded into a power series of Legendre polynomials, the first few of which are $P_0(x) = 1$, $P_1(x) = x$, $P_2(x) = \frac{3}{2}x^2 - \frac{1}{2}$. Explicitly, the first few terms in the power series are thus

$$V_\mathrm{S} = -\frac{GM_\mathrm{S}}{R_\mathrm{S}}\left[1+\frac{a}{R_\mathrm{S}}\cos\alpha+\frac{a^2}{R_\mathrm{S}^2}\left(\frac{3}{2}\cos^2\alpha-\frac{1}{2}\right)+\dots\right]. \tag{6.9}$$

The power series converges rapidly because a/R_S is extremely small. The earth's radius is 6.4×10^6 m, and the distance to the sun is $R_\mathrm{S} = 1.5 \times 10^{11}$ m. Even for the moon, the distance $R_\mathrm{L} = 3.8 \times 10^8$ m is much larger than the earth's radius. The first term in (6.9), which is of order zero in a/R_S, is a constant and thus does not give rise to any forces. The second term, of first order in a/R_S, corresponds to a force that is constant across the surface of the earth because $a\cos\alpha$ is the observer's distance from a plane through the earth's center that is perpendicular to the vector pointing from the earth's center to the sun. This is the gravitational force that keeps the earth on its orbit around the sun and in the earth's frame is balanced by the centrifugal force of the orbital motion.

The generation of a tidal potential occurs at second order in a/R_S. This is the first term that leads to variations of the gravitational force over the surface of the earth and is the leading-order tide-generating potential. It is a good approximation to the full tide-generating potential, given that the above power series converges rapidly. This potential distorts the earth's gravitational potential by

$$\frac{V_\mathrm{S}^{(2)}}{g} = -\frac{M_\mathrm{S}}{M_\mathrm{E}}\frac{a^4}{R_\mathrm{S}^3}\left(\frac{3}{2}\cos^2\alpha-\frac{1}{2}\right) = -H_\mathrm{S}\left(\frac{3}{2}\cos^2\alpha-\frac{1}{2}\right), \tag{6.10}$$

where $g = GM_\mathrm{E}/a^2$ with M_E being the earth's mass, and

$$H_\mathrm{S} = \frac{M_\mathrm{S}}{M_\mathrm{E}}\frac{a^4}{R_\mathrm{S}^3} = 0.16 \text{ m} \tag{6.11}$$

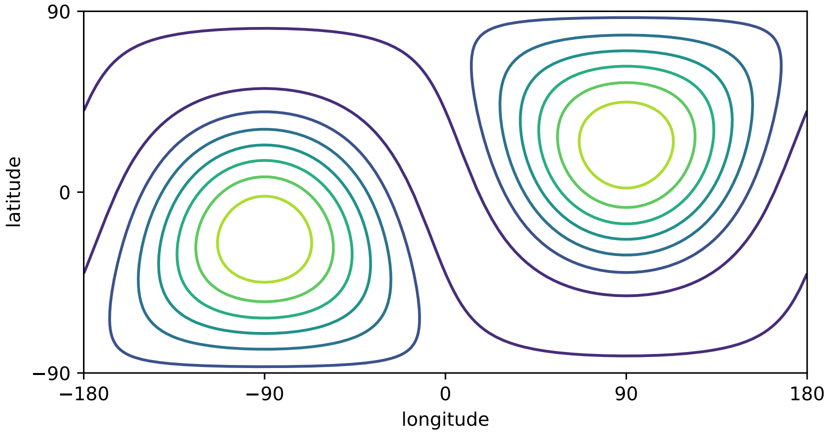

Figure 6.1: Solar tide-generating potential when the sub-solar point is at 23.44°N (solstice) and 90°E. The two maxima form bulges at opposite sides of the earth.

sets the scale by which the tide-generating potential distorts the earth's equipotential surfaces. The spatial structure of this distortion consists of two bulges: one facing the sun and one facing away from the sun. This arises because the sun-facing side experiences a slightly larger force than is required to balance the centrifugal force of the orbit, and the opposing side experiences a slightly smaller force than required to balance the centrifugal force, resulting in an outward force anomaly there.

As the earth rotates, a stationary observer on the surface of the earth moves in and out of such a bulge twice per day. Unless the sun is over the equator (equinox) or the observer is at the equator, one of the bulges is larger than the other. A simple representation of the forcing function in time is the superposition of two sine waves, one at a semi-diurnal frequency, one at a diurnal frequency. This is why the earth's tides are dominated by semi-diurnal and diurnal constituents.

What remains to be done is to specify the relative position of the sun to the earth. This can be determined from orbital dynamics, and in this case is largely described by Kepler's laws.

The tides due to the moon, the lunar tides, arise analogously. The distortion of the equipotential surfaces is

$$\frac{V_{\mathrm{L}}^{(2)}}{g} = -H_{\mathrm{L}}\left(\frac{3}{2}\cos^2\alpha - \frac{1}{2}\right), \tag{6.12}$$

where

$$H_{\mathrm{L}} = \frac{M_{\mathrm{L}}}{M_{\mathrm{E}}}\frac{a^4}{R_{\mathrm{L}}^3} = 0.36\ \mathrm{m}. \tag{6.13}$$

The lunar tidal forcing is about twice as strong as the solar tidal forcing. The much smaller mass of the moon is more than compensated by the dependence of the tidal potential on the inverse cube of the distance, which is of course much smaller as well.

The lunar tide is somewhat more complicated than the solar tide because the moon's orbit is complicated by the influence of both the earth and the sun. Still, diurnal and semi-diurnal constituents dominate, and the principal lunar semi-diurnal constituent M_2 is typically the strongest tidal constituent. It has a period slightly longer than 12 hours.

The time-dependent tidal potential acts as a body force on the fluid ocean. To represent this forcing, it is useful to define the equilibrium tide

$$\eta = -\frac{V_{\mathrm{S}}^{(2)} + V_{\mathrm{L}}^{(2)}}{g}, \tag{6.14}$$

which would be the sea surface elevation if the ocean adjusted instantaneously to the distorted equipotential surfaces. This would be the static response of the ocean if the sun and the moon did not move relative to the earth's surface. Since they do move, the response is dynamical and can be described to leading order by linear shallow-water dynamics:

$$\frac{\partial u}{\partial t} - f v = -g \frac{\partial}{\partial x}(h - \eta), \tag{6.15}$$

$$\frac{\partial v}{\partial t} + f u = -g \frac{\partial}{\partial y}(h - \eta), \tag{6.16}$$

$$\frac{\partial h}{\partial t} + H\left(\frac{\partial u}{\partial x} + \frac{\partial v}{\partial y}\right) = 0. \tag{6.17}$$

The resulting motion is variably called the barotropic tide, the external tide, or the surface tide. It is standard practice to decompose the astronomical forcing into harmonics, which are call tidal constituents. Since the dynamical response is largely linear, the tidal motion can be calculated frequency by frequency as well:

$$-i\omega\hat{u} - f\hat{v} + g\frac{\partial \hat{h}}{\partial x} = g\frac{\partial \hat{\eta}}{\partial x}, \tag{6.18}$$

$$-i\omega\hat{v} + f\hat{u} + g\frac{\partial \hat{h}}{\partial y} = g\frac{\partial \hat{\eta}}{\partial y}, \tag{6.19}$$

$$-i\omega\hat{h} + H\left(\frac{\partial \hat{u}}{\partial x} + \frac{\partial \hat{v}}{\partial y}\right) = 0. \tag{6.20}$$

Applying these equations, usually written in spherical coordinates, to the ocean's bathymetry, we can now in principle calculate the dynamical response to any periodic astronomical forcing encoded in $\hat{\eta}$.

Tides have long been observed with tide gauges, and satellite altimeters have provided global observations of the tidal perturbations to the sea surface elevation since the 1990s. Combining these observations with tidal models has led to accurate global tidal charts. This combination of data and models has also been used to constrain the loss of energy of the external tide, either through dissipation in a bottom boundary layer or through the conversion to internal tides by flow over topography. This conversion from external to internal tides, i.e., internal waves at tidal frequencies, is of particular interest because some fraction of that energy is thought to be dissipated by small-scale turbulence that occurs when these internal tides break. The total dissipation rate of tidal energy is well-constrained from the orbital evolution of the earth–moon system—because energy is dissipated in the earth's ocean, the earth's tides exert a torque on the moon that transfers angular momentum and energy to the moon's orbit. In response, the moon is slowly receding from the earth and the earth's rotation is slowed, both of which can be measure with exquisite precision. This has turned out to be a useful constraint on the amount of mixing in the deep ocean (Munk and Wunsch, 1998).

Bibliography

Buckingham, C. E. et al. (2016) Seasonality of Submesoscale Flows in the Ocean Surface Boundary Layer. *Geophysical Research Letters* 43 (5), 2118–2126.

Callies, J., R. Ferrari (2013) Interpreting Energy and Tracer Spectra of Upper-Ocean Turbulence in the Submesoscale Range (1–200 km). *Journal of Physical Oceanography* 43 (11), 2456–2474.

Callies, J., R. Ferrari, J. M. Klymak, J. Gula (2015) Seasonality in Submesoscale Turbulence. *Nature Communications* 6 (1), 6862.

Callies, J., G. Flierl, R. Ferrari, B. Fox-Kemper (2016) The Role of Mixed-Layer Instabilities in Submesoscale Turbulence. *Journal of Fluid Mechanics* 788, 5–41.

Ferreira, D. et al. (2018) Atlantic-Pacific Asymmetry in Deep Water Formation. *Annual Review of Earth and Planetary Sciences* 46, 327–352.

Gill, A. E., J. S. A. Green, A. J. Simmons (1974) Energy Partition in the Large-Scale Ocean Circulation and the Production of Mid-Ocean Eddies. *Deep Sea Research and Oceanographic Abstracts* 21 (7), 499–528.

Gray, A. R., K. S. Johnson, S. M. Bushinsky, S. C. Riser, J. L. Russell, L. D. Talley, R. Wanninkhof, N. L. Williams, J. L. Sarmiento (2018) Autonomous Biogeochemical Floats Detect Significant Carbon Dioxide Outgassing in the High-Latitude Southern Ocean. *Geophysical Research Letters* 45 (17), 9049–9057.

Hoskins, B. J., F. P. Bretherton (1972) Atmospheric Frontogenesis Models: Mathematical Formulation and Solution. *Journal of the Atmospheric Sciences* 29 (1), 11–37.

Hoskins, B. J. (1975) The Geostrophic Momentum Approximation and the Semi-Geostrophic Equations. *Journal of the Atmospheric Sciences* 32 (2), 233–242.

Johnson, G. C., C. Cadot, J. M. Lyman, K. E. McTaggart, E. L. Steffen (2020) Antarctic Bottom Water Warming in the Brazil Basin: 1990s through 2020, from WOCE to Deep Argo. *Geophysical Research Letters* 47 (18), e2020GL089191.

Ledwell, J. R., E. T. Montgomery, K. L. Polzin, L. C. St. Laurent, R. W. Schmitt, J. M. Toole (2000) Evidence for Enhanced Mixing over Rough Topography in the Abyssal Ocean. *Nature* 403 (6766), 179–182.

Luyten, J. R., J. Pedlosky, H. Stommel (1983) The Ventilated Thermocline. *Journal of Physical Oceanography* 13 (2), 292–309.

Marshall, J. C., A. J. G. Nurser, R. Brugge (1988) On the Time-Averaged Flow of Quasi-Geostrophic Wind-Driven Gyres. *Journal of Geophysical Research: Oceans* 93 (C12), 15427–15436.

Munk, W., C. Wunsch (1998) Abyssal Recipes II: Energetics of Tidal and Wind Mixing. *Deep Sea Research Part I: Oceanographic Research Papers* 45 (12), 1977–2010.

Munk, W. H. (1966) Abyssal Recipes. *Deep Sea Research and Oceanographic Abstracts* 13 (4), 707–730.

Polzin, K. L., J. M. Toole, J. R. Ledwell, R. W. Schmitt (1997) Spatial Variability of Turbulent Mixing in the Abyssal Ocean. *Science* 276 (5309), 93–96.

Rhines, P., W. Young (1982a) A Theory of Wind-Driven Circulation. I. Mid-ocean Gyres. *Journal of Marine Research* 40 (S).

Rhines, P. B., W. R. Young (1982b) Homogenization of Potential Vorticity in Planetary Gyres. *Journal of Fluid Mechanics* 122, 347–367.

Richardson, L. F., H. Stommel (1948) Note on Eddy Diffusion in the Sea. *Journal of the Atmospheric Sciences* 5 (5), 238–240.

Rocha, C. B., T. K. Chereskin, S. T. Gille, D. Menemenlis (2016) Mesoscale to Submesoscale Wavenumber Spectra in Drake Passage. *Journal of Physical Oceanography* 46 (2), 601–620.

Roemmich, D., J. Church, J. Gilson, D. Monselesan, P. Sutton, S. Wijffels (2015) Unabated Planetary Warming and Its Ocean Structure since 2006. *Nature Climate Change* 5 (3), 240–245.

Rudnick, D. L. (2001) On the Skewness of Vorticity in the Upper Ocean. *Geophysical Research Letters* 28 (10), 2045–2048.

Scott, R. B., F. Wang (2005) Direct Evidence of an Oceanic Inverse Kinetic Energy Cascade from Satellite Altimetry. *Journal of Physical Oceanography* 35 (9), 1650–1666.

Shcherbina, A. Y., E. A. D'Asaro, C. M. Lee, J. M. Klymak, M. J. Molemaker, J. C. McWilliams (2013) Statistics of Vertical Vorticity, Divergence, and Strain in a Developed Submesoscale Turbulence Field. *Geophysical Research Letters* 40 (17), 4706–4711.

Smith, K. (2007) The Geography of Linear Baroclinic Instability in Earth's Oceans. *Journal of Marine Research* 65 (5).

Stommel, H., A. B. Arons (1959a) On the Abyssal Circulation of the World Ocean—I. Stationary Planetary Flow Patterns on a Sphere. *Deep Sea Research (1953)* 6, 140–154.

Stommel, H., A. B. Arons (1959b) On the Abyssal Circulation of the World Ocean—II. An Idealized Model of the Circulation Pattern and Amplitude in Oceanic Basins. *Deep Sea Research (1953)* 6, 217–233.

Stommel, H., A. B. Arons, A. J. Faller (1958) Some Examples of Stationary Planetary Flow Patterns in Bounded Basins. *Tellus* 10 (2), 179–187.

Stone, P. H. (1966a) Frontogenesis by Horizontal Wind Deformation Fields. *Journal of the Atmospheric Sciences* 23 (5), 455–465.

Stone, P. H. (1966b) On Non-Geostrophic Baroclinic Stability. *Journal of the Atmospheric Sciences* 23 (4), 390–400.

Talley, L. D. (1988) Potential Vorticity Distribution in the North Pacific. *Journal of Physical Oceanography* 18 (1), 89–106.

Tulloch, R., J. Marshall, C. Hill, K. S. Smith (2011) Scales, Growth Rates, and Spectral Fluxes of Baroclinic Instability in the Ocean. *Journal of Physical Oceanography* 41 (6), 1057–1076.

Wang, D.-P., C. N. Flagg, K. Donohue, H. T. Rossby (2010) Wavenumber Spectrum in the Gulf Stream from Shipboard ADCP Observations and Comparison with Altimetry Measurements. *Journal of Physical Oceanography* 40 (4), 840–844.

Wunsch, C. (2006) *Discrete Inverse and State Estimation Problems: With Geophysical Fluid Applications*. Cambridge University Press.

Wunsch, C., P. Heimbach (2007) Practical Global Oceanic State Estimation. *Physica D: Nonlinear Phenomena*. Data Assimilation 230 (1), 197–208.

Young, W. R. (2012) An Exact Thickness-Weighted Average Formulation of the Boussinesq Equations. *Journal of Physical Oceanography* 42 (5), 692–707.